Nonlinear and Interference Techniques for Biomedical Imaging

Rumelo Amor

Submitted in fulfilment of the requirements for

the degree of Doctor of Philosophy

Department of Physics

Faculty of Science

University of Strathclyde

March 31, 2015

Abstract

Optical microscopy has long been an established tool in the biomedical sciences, being the preferred choice in the study of single cells and tissue sections. The realisation of the confocal laser scanning microscope in the 1980s led to major advances in the way optical microscopy is implemented, paving the way for the use of interference techniques such as 4Pi microscopy to increase the optical resolution, and for nonlinear microscopy techniques such as two-photon microscopy, which allows deeper penetration and the imaging of live specimens as a consequence of reduced photo-bleaching, and coherent anti-Stokes Raman scattering (CARS) microscopy, which produces high-contrast images without the need for fluorescent staining. In this work, I discuss advances in nonlinear and interference techniques available for biomedical imaging. I present a simultaneous near-field and far-field viewer for use in aligning the input beams in a CARS microscope and in a sum-frequency-generation-based two-photon microscope. I show 3D optical sectioning of whole mouse embryos using the Mesolens, a giant microscope objective capable of subcellular resolution in a 5 mm field of view, and present theoretical calculations on its use for two-photon microscopy. I present fast recording of synaptic events in neurones, with reduced photo-bleaching, using widefield

1

two-photon microscopy. Finally, I show multiple super-resolved sections are obtained using a laser scanning standing wave microscope, generating precise contour maps of the surface membrane of red blood cells and revealing 3D information from a single image.

Contents

List of Figures

9

10

15

16

17

Acknowledgements

The road I took towards a Ph.D. has been a long one. I was already studying for a Ph.D. when I left Manila in October 2008 to be with Jacq, who had started hers at the University of Glasgow the month before, two weeks after we got married. Now, seven years on, we have two degrees between us, and also two happy companions: Narra and Kahil.

I owe everything to Gail, who took me in as visiting researcher a few months after I arrived, and had me build a confocal microscope, and taught me lasers and optical parametric oscillators and temporal and spatial overlap and many other fancy things that were all new to me then (they still are now). The confocal microscope I eventually built and it is still being used today, and Gail eventually secured a studentship for me. I am where I am now because of her.

Brad taught me and all of us at the CfB not just optics and microscopy, but also biology and the magical (to me) arts of microtechnique and immuno-histochemistry. I have enjoyed learning from him, but equally valuable to me are his many stories and anecdotes, of scientists and of science, especially those set "In the early days of the confocal," and also stories of his time in the Philippines, particularly of the children who brought him all manner of

I thank John and Es, and Louise and Trevor and Gillian, and Sumeet, and Margaret, with whom I have worked, on projects and in the writing of manuscripts, and from whom I learned many things.

Ewan and Bob at the mechanical workshop and Ged at the electronics workshop and John at the SIPBS workshop made many beautiful things for me, bespoke and according to specifications, and oftentimes even more, and I thank them here now.

I thank Lynn and Catherine and Kayleigh and Audrey at Physics for taking care of the administrative side of things during the course of my Ph.D.

Greg and Alison were of my generation in joining the CfB, and they were always there to discuss ideas with and to make suggestions, but what I appreciate most was their joining us in the Philippines, to partake of our sweet mangoes and caramelised bananas, and take in the quiet grandeur of our Chocolate Hills, and ride horses up a volcano, and swim with the fishes in our reefs. Those were happy times and I will always remember them.

I thank Wei and Elric and John and Sara, and Michelle and Johanna and Jan and Calum, for their company in the old and the new CfB.

I thank Sharat and Russell and James and Panos, for their friendship in MATLAB and also outside of it.

I dedicate this work to Mamang, ~~who would have been happy to see~~ who will be happy to see that indeed I did a Ph.D. in another country, having asked me about it about many years ago, and to Papang and Mec and Fielmor, who have always been there to support me.

Finally, I thank Jacq for bringing me to Glasgow, having made it clear

26

before we married that she was studying in Europe, and that if we were to be husband and wife we should be together. She always believed that we could achieve what we set out to achieve when we came here, and she was right. I thank Narra and Kahil for the joy they give, doing what children do, decorating our days with pleasant surprises as they grow, and for the excitement I feel when I think of what they will choose to become someday, and I thank God for our happy little family.

Declaration of Authenticity and Author's Rights

This thesis is the result of the author's original research. It has been composed by the author and has not been previously submitted for examination which has led to the award of a degree.

Rumelo Amor

May 27, 2015

Publications

1. **A compact instrument for adjusting laser beams to be accurately coincident and coaxial and its use in biomedical imaging using wave-mixed laser sources,** R. Amor, G. Norris, J. Dempster, W. B. Amos and G. McConnell, *Review of Scientific Instruments* 83, 083705 (2012).

2. **A promising new wavelength region for three-photon fluorescence microscopy of live cells,** G. Norris, R. Amor, J. Dempster, W. B. Amos and G. McConnell, *Journal of Microscopy* 246, 266–273 (2012).

3. **Increased signals from short-wavelength-excited fluorescent molecules using sub-Ti:Sapphire wavelengths,** G. Norris, R. Amor, J. Dempster, W. B. Amos and G. McConnell, *Journal of Microscopy* 248, 200–207 (2012).

4. **Antitumor activity of the tea polyphenol epigallocatechin-3-gallate encapsulated in targeted vesicles after intravenous administration,** F. Lemarie, C. W. Chang, D.

R. Blatchford, R. Amor, G. Norris, L. Tetley, G. McConnell and C. Dufes, *Nanomedicine* 8, 181–192 (2013).

5. **Standing-wave-excited multiplanar fluorescence in a laser scanning microscope reveals 3D information on red blood cells,** R. Amor, S. Mahajan, W. B. Amos and G. McConnell, *Scientific Reports* 4: 7359 (2014).

6. **A simple but precise method for quantitative measurement of the quality of the laser focus in a scanning optical microscope,** J. Tragardh, K. MacRae, C. Travis, R. Amor, G. Norris, S. H. Wilson, G.-L. Oppo and G. McConnell, *Journal of Microscopy* (2015). doi: 10.1111/jmi.12249

7. **Exploration of the two-photon excitation spectrum of fluorescent dyes at wavelengths below the range of the Ti:Sapphire laser,** J. Tragardh, G. Robb, R. Amor, W. B. Amos, J. Dumpster and G. McConnell, *Journal of Microscopy* (2015). doi: 10.1111/jmi.12255

8. **Widefield two-photon excitation without scanning: live cell microscopy with high time resolution and low photo-bleaching,** R. Amor, J. Tragardh, G. Robb, L. Wilson, N. Z. Abdul Rahman, J. Dempster, W. B. Amos, T. J. Bushell and G. McConnell, *In peer review.* arXiv:1501.00044

It was literally darkness visible.

GEORGE STOKES

Chapter 1

Introduction

In this chapter, I will discuss the development of the optical microscope and its eventual use in biomedicine. I will begin with the invention of the microscope, then I will discuss the fluorescence microscope, followed by the development of the confocal microscope, beginning with Minsky's microscopy apparatus and culminating in the confocal laser scanning microscope developed by several groups. I will finish the chapter by discussing nonlinear and interference techniques in microscopy.

1.1   The light microscope

The invention of the microscope is placed in the period 1590–1610 and credited chiefly to the father-and-son pair of Hans and Zacharias Janssen and to Hans Lippershey, all famous spectacle makers in Middelburg, Holland [1, 2]. The Janssens placed, perhaps accidentally, two convex lenses in the proper relative positions in a tube so that they acted as a true compound

microscope, the image formed by the objective being magnified by the ocular before reaching the eye [3]. The Janssens' design is shown in Fig. 1.1 and consisted of three tubes, the middle tube acting as a sleeve into which the front tube containing the objective lens and rear tube containing the ocular lens could be pushed [1, 2, 4, 5]. It had a magnification of 3× when the inner tubes were pushed right in, and 9× when they were fully extended [1, 5].
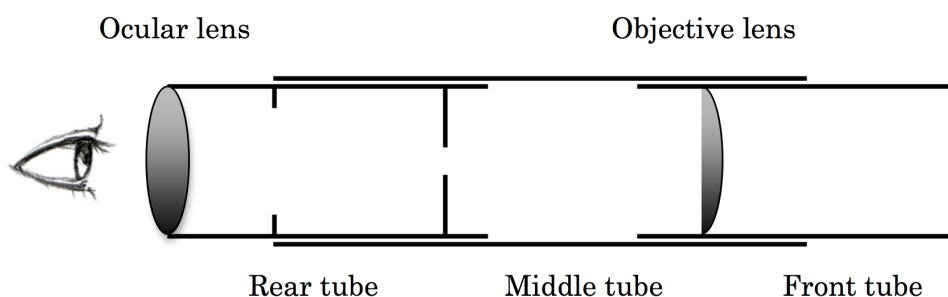
Figure 1.1: Diagram of the microscope of Hans and Zacharias Janssen. It had apertures at each end to admit light, and contained an objective lens and an ocular lens, making it a true compound microscope.

A schematic diagram of two convex lenses arranged to form a compound microscope is shown in Fig. 1.2. This microscope is of the "Keplerian" type, the use of a convex lens as the ocular lens having been first suggested by Johannes Kepler and published in his book *Dioptrice* in 1611 [5]. In the compound microscope, the object is placed near the focus of the first lens (the objective lens), producing a real, magnified intermediate image *(Image I)* between the objective lens and the second lens (the ocular lens) [6]. The

intermediate image is inverted with respect to the object, and the ocular lens produces a final virtual, inverted image *(Image II)*, magnified further still.
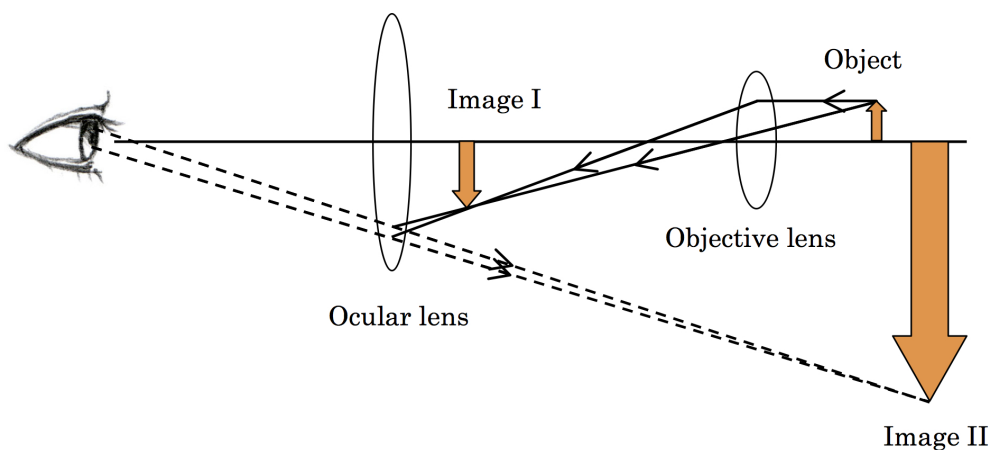
Figure 1.2: Schematic diagram of a compound microscope of the "Keplerian type", using a convex lens as the ocular lens. The objective lens forms a real, inverted, magnified image *(Image I)* of the object, further magnified by the ocular lens *(Image II)*. The final virtual image is inverted with respect to the object.

The microscope in its first incarnation was treated more as a toy [4] rather than the powerful scientific tool it is today. In 1625, Francesco Stelluti of the *Accademia dei Lincei* in Rome drew the head of a bee at a magnification of 5× and so was responsible for the first sketch made using a compound microscope [1, 4, 7, 8, 9, 10]. The discovery of capillaries by Marcello Malpighi in 1661 [11] is considered the first "truly scientific" use of the microscope,

being systematic and an attempt at finding the explanation of a scientific problem that existed since William Harvey's study of blood circulation in 1628 [4].

When Robert Hooke published *Micrographia* in 1665 [12], it created a sensation [13] and greatly increased the importance of the microscope [4]. *Micrographia* contained sixty "observations", including detailed accounts and illustrations of the anatomy of the flea and louse, the honeycomb structure of cork, which he described as being made of "cells", and a colony of "hairy mould" (the microfungus *Mucor*), the first published depiction of a microorganism [13].

At about the same time that Hooke improved the design and construction of the compound microscope, Antoni van Leeuwenhoek was making ever better lenses for his simple microscopes [14] which probably achieved magnifications of 266× and even 400× or 500×, with a resolution of 1.3 μm or better [15]. Leeuwenhoek and others like him persevered with (or perhaps preferred) the simple microscope because, as shown in Fig. 1.2, in the compound microscope, the intermediate image produced by the objective lens is further magnified by the ocular lens, and so any aberrations introduced by the objective are further compounded by the action of the ocular [5].

In 1674, Leeuwenhoek discovered at least three forms of life: the common green alga *Spirogyra* ("green streaks, spirally wound serpent-wise"), rotifers ("animalcules whereof ... I saw two little legs near the head, and two little fins at the hindmost end of the body) and *Euglena viridis* ("animalcules ... green in the middle, and before and behind white") [16], and in 1676 he discovered bacteria and other microorganisms ("ten hundred thousand of these living

creatures could scarce equal the bulk of a coarse sand-grain") [17]. Thus did Leeuwenhoek lay the foundations of microbiology [18].

1.2   The fluorescence microscope

The many improvements in lens design and in the construction of the microscope had one of its fruits in the fluorescence microscope. The earliest record of fluorescence was in 1569, when the Spanish physician Nicolas Monardes wrote of a certain wood that had the remarkable property of causing clear water when soaked in it to assume an azure blue colour in spite of the fact that the wood itself was whitish [19].

George Stokes made a systematic study of fluorescence in quinine. Stokes initially called the phenomenon "dispersive reflection", but wrote: "I confess I do not like this term. I am almost inclined to coin a word, and call the appearance fluorescence, from fluor-spar, as the analogous term opalescence is derived from the name of a mineral [20]." Stokes used a prism to disperse the spectrum of sunlight and illuminate a solution of quinine in a test tube, which he moved through the colours beginning with red, noting that for nearly the whole spectrum, the light passed through the fluid as through water, but on arriving nearly at the violet end, a ghost-like gleam of pale blue light shot right across the tube. Of his observations when the solution was placed beyond the violet, Stokes wrote:

"It was certainly a curious sight to see the tube instantaneously lighted up when plunged into the invisible rays: it was literally *darkness visible.*"

Fluorescence occurs when a fluorescent substance (a fluorophore) in the

ground state absorbs energy in the form of light, promoting an electron to an excited state. The return of the electron to the ground state occurs rapidly (about 10 ns) by emission of a photon [21]. A Jablonski diagram (Fig. 1.3) is used to illustrate the processes that occur between the absorption and emission of light, including that of fluorescence. In a Jablonski diagram, electronic energy states are represented by bold horizontal lines, above which are vibrational energy levels represented by thin horizontal lines. In Fig. 1.3, an electron at the ground state S_0 is promoted to the excited state S_1 through the absorption of a photon (blue arrow). Some of this energy is lost for example due to non-radiative decay between a vibrational energy level and the lowest level of the excited state (black arrow) [21]. The electron therefore emits light at a lower energy, and longer wavelength (green arrow), when it returns to the ground state. This shift in wavelength now bears Stokes' name.
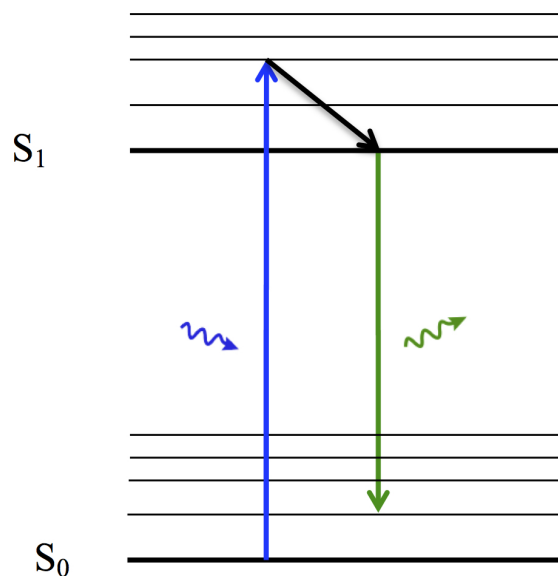
Figure 1.3: Jablonski diagram for fluorescence. The absorption of a photon (blue arrow) causes an electron in the ground state to be promoted to an excited state, after which it emits light at a longer wavelength (green arrow) when it returns to the ground state. Energy is lost between absorption and emission for example due to non-radiative decay between a vibrational energy level and the lowest level of the excited state (black arrow).

In 1914, Stanislaus von Prowazek was the first to study fluorescence staining in living cells [22]. The first demonstration of the vast potential of fluorescence microscopy in biology was made in 1941 and again in 1949 by Albert Hewett Coons and co-workers, who used anthracene-isocyanate and later fluorescein to directly label pneumococcal anti-serum [23, 24]. In 1954, another breakthrough was made when Thomas Weller and Coons developed and used an indirect method of staining, comprised of a non-labeled primary

and a fluorescein-labeled secondary antibody, to identify viral particles in culture. Fluorescence labelling has become an ideal technique for the study of specimens in cell biology and biomedicine because it allows the detection of specific molecules at small concentrations with good signal-to-background ratio [25]. The use of fluorescent labeled antibodies has, more than any other method, shaped cell biology, molecular biology and immunology [26].

1.3   The confocal microscope

The confocal microscope was invented by Marvin Minsky in 1955 [27], in his preoccupation to understand the brain, specifically, how brain cells are connected to each other [28]. Minsky was not satisfied with visualising one cell at a time; he knew that to obtain the brain's wiring diagram, all the cells needed to be visible in a three-dimensional region. But since brain tissue is packed with interconnected cells, staining them all would result in an image made blurry by rays of scattered light deflected by or from areas in the specimen outside of the area being viewed; Minsky knew that each plane in the three-dimensional image must be thin enough in order to remove the blur. His solution was to avoid all the scattered light by never allowing any of the unwanted light to enter his photo-sensitive detector; he eliminated all rays not initially aimed at the focal point by imaging a pinhole on a single point of the specimen, and rejected the light scattered by out-of-focus structures by placing a second pinhole in front of his detector at a point conjugate to the focal point. Figure 1.4 shows an illustration of Minsky's "microscopy apparatus".
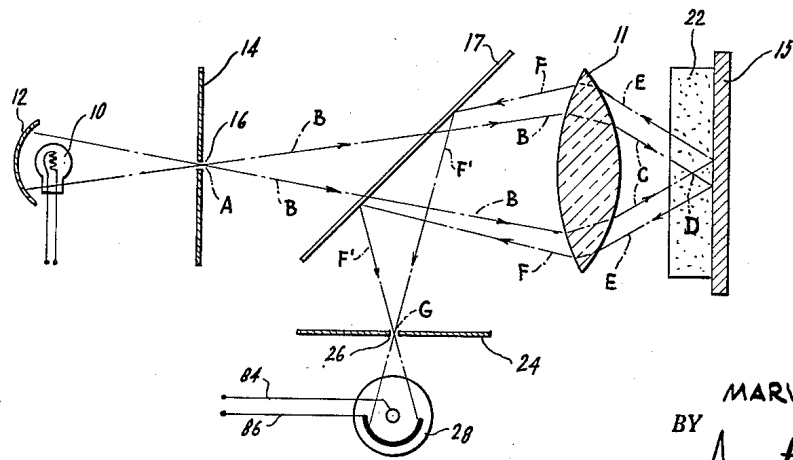
Figure 1.4: Marvin Minsky's illustration, now in the public domain, of his "microscopy apparatus" in a modified arrangement using a single objective *(11)* to focus the light from the pinhole aperture *(16)* at the illumination source and to focus the illuminated specimen point on the detection pinhole aperture *(26)*. The specimen *(22)* is mounted on a mirror *(15)* and a beam-splitter *(17)* is positioned above, and with the reflecting side facing, the objective. The convergent beam *(FF)* is reflected perpendicularly from the beam-splitter and converges to the focal point G at the detector pinhole aperture. The photoelectric cell *(28)* is aligned with the aperture to measure the intensity of the light that is allowed to pass.

As the detector in the confocal microscope sees only one point in the specimen at any given time, the image is built up by scanning the point across the specimen. In Minsky's prototype, he decided to move the stage, and caused the beam to be stationary [28]. The signal was measured using a

low noise photomultiplier that he designed and the image was reconstructed on a military surplus long persistence radar screen, with the image visible for about ten seconds, which was also the time it took for a scan [28].

Minsky's instrument was clearly ahead of its time, by decades. For one thing, as intimated by Minsky himself in his memoir on his invention, he could not reduce the imaging time by using brighter light – the laser had not yet been invented at the time. Also, the personal computer was still to come, as well as the high-resolution displays taken for granted nowadays.

In the late 1980s, the development of the confocal laser scanning microscope was pursued by Brakenhoff *et al.* [29], Carlsson *et al.* [30], Draaijer and Houpt [31], Goldstein *et al.* [32], and White, Amos, Durbin and Fordham [33, 34]. Of these designs, the one developed by White and Amos at the Medical Research Council in Cambridge is one of the more successful commercially. One of the more useful features of their design, made possible by placing the confocal aperture far from the scanning optics, is the enlarged aperture, as large as a millimetre in diameter, compared with the tens of micrometers found in other designs [35]. This was important because it meant an ordinary iris diaphragm could be used, with the beam path aligned without the need for micro-manipulation.

After the publication of White and Amos's striking results, and also those of others, notably Brakenhoff et al.'s, showing optical sectioning without actually cutting specimen sections, the confocal laser scanning microscope was taken up by the biological community. The microscope proved to be versatile, as, for example, by varying the diameter of the aperture, one changes the optical section thickness, or by changing the region scanned by the mir-

41

rors, one is able to zoom in or out of the image using the same objective, and without loss of resolution. Today, close to three decades after those developments, the confocal microscope has established itself as a requisite tool in every biological research facility. However, because microscope objectives are built small so that aberrations are minimised, the field of view of any microscope is small and so in order to image large specimens such as intact embryos or the brain, hundreds of images need to be stitched together, a process that requires considerable time and effort. I will show later on in this thesis that this issue is addressed by the Mesolens, a giant microscope objective that can image large specimens in a single snapshot, extending the range of the confocal microscope to cover large-volume specimens.

1.4 Nonlinear and interference techniques for microscopy

In this last section, I will discuss nonlinear and interference techniques employed in microscopy. Nonlinear techniques are so called because the signal being generated depends nonlinearly on the excitation intensity. For example, in two- or three-photon excitation of fluorescence, the fluorescence signal increases quadratically or cubicly with the excitation intensity [36]. Nonlinear techniques can either be incoherent or coherent, with two-photon and three-photon excitation of fluorescence being two examples of the incoherent kind [37]. On the other hand, coherent nonlinear techniques include second and third harmonic generation, four-wave mixing, stimulated Raman scattering, coherent anti-Stokes Raman scattering, coherent Stokes Raman scatter-

ing, and Raman-induced Kerr effect [38]. Of these mentioned, I will discuss two-photon excited fluorescence and coherent anti-Stokes Raman scattering, which I have worked on during the course of the research I describe in this thesis.

1.4.1 Two-photon-excited fluorescence

Two-photon excitation, a process in which an atom makes a transition from ground state to an excited state via the simultaneous (within $\sim$0.5 fs [39]) absorption of two photons, was first proposed by Göeppert-Mayer in 1931 [40]. In the two-photon absorption process, a molecule in its ground state absorbs two photons simultaneously, is promoted to an electronically excited state, and returns to the ground state by emission of a photon [21].

After the development of the confocal laser scanning microscope in the late 1980s by Brakenhoff *et al.* [29], Carlsson *et al.* [30], Draaijer and Houpt [31], Goldstein *et al.* [32], and White, Amos, Durbin and Fordham [33, 34], Denk, Strickler and Webb demonstrated two-photon laser scanning microscopy in 1990 using the microscope design of White and Amos [41].

In two-photon excitation, the photon density is highest at the focal plane, maximising the probability of two-photon absorption [42]. This means that only structures at the focal plane will emit fluorescence and as a consequence two-photon excitation has inherent three-dimensional optical sectioning, and along with it, reduced photobleaching and phototoxicity [39, 41, 43, 44]. It is for this reason that two-photon microscopy has opened a rapidly expanding field of imaging studies in intact tissues and living animals. However, two-photon microscopy is still a relatively specialist technique, with access being

limited to a few laboratories which either have the necessary in-house expertise to custom-build a two-photon microscope, or the resources to purchase a commercial system [45].

1.4.2 Coherent anti-Stokes Raman scattering microscopy

Coherent anti-Stokes Raman scattering (CARS) is a four-wave mixing process in which a pump beam at a frequency ω_p, a Stokes beam at a frequency ω_S, and a probe beam at a frequency ω_{pr} interact with the specimen and generate an anti-Stokes beam at a new frequency [46]. If the pump and Stokes beams are selected such that the difference frequency $\omega_p - \omega_S$ coincides with a molecular vibration within the specimen, the anti-Stokes signal is greatly enhanced, and real-time imaging possible [47, 48].

After the demonstration of CARS microscopy by Duncan *et al.* in the early 1980s [49, 50] and the improvement in the sensitivity introduced by Zumbusch, Holtom and Xie in 1999 making three-dimensional optical sectioning possible [47], CARS microscopy is now routinely being used for label-free imaging in biology and medicine (reviewed by Volkmer [51] and Evans and Xie [52]). Using the intrinsic molecular vibrations of a specimen, CARS microscopy has been used to visualise DNA [53], protein [54] and lipids [55] in living cells, and to study skin and brain tissue in vivo [56, 57]. However, as with two-photon microscopy, there are still relatively few laboratories that have CARS microscopy systems due to the fact that CARS microscopy, more so than two-photon microscopy, requires in-house expertise to custom-build and run, requiring two laser sources to be overlapped in time and space for the image contrast not to vanish.

1.4.3 Interference techniques

The first observation of interference phenomena was that of Newton's rings [58], so called because Newton was the first to study it, in 1717. Newton's rings is explained in elementary physics teaching by the interference between successive reflections of a beam of white light at normal incidence and is demonstrated by the use of a convex lens placed with one point in contact with a planar glass plate. The dark centre of the pattern is explained by a phase change of π, regardless of frequency, in the light reflected from the planar air–glass interface which places it in anti-phase to the light internally reflected within the lens in the same region.

A standing wave is another type of interference phenomenon, the result of interference between two waves traveling in opposite directions. Standing light waves were first detected by Otto Wiener in 1890 by using silver halide crystals in photographic film as microscopic detectors [59, 60, 61].

In 1964, interference was used in biological microscopy by Adam Curtis, who observed colours resembling Newton's rings in living cells attached to the underside of a glass coverslip when viewed with a reflection microscope [62]. Curtis interpreted these as due to interference between light reflected off the high-index lipoidal membrane of the cell and the light internally reflected within the coverslip. In 1979, David Gingell and Ian Todd observed similar intensity changes when water films between glass were observed, even when objectives of high numerical aperture were used [63]. Gingell and Todd measured the thickness of the water film and found that the normal incidence theory gave incorrect results at high numerical aperture.

In 1993, Frederick Lanni and co-workers performed standing-wave exci-

tation of fluorescence by placing a mirror beyond the specimen to reflect the laser beam coming out of the microscope objective [64]. In this way, Lanni et al. improved the axial resolution to the intensity peaks at the antinodes, with a full width at half maximum of $\lambda/4n$, where λ is the excitation wavelength and n is the medium refractive index.

In the following chapters, I will discuss the work that I did using non-linear and interference techniques to improve the performance of the light microscope.

Chapter 2 is about my work on coherent anti-Stokes Raman scattering microscopy and two-photon excitation of fluorescence using a sum-frequency generated source, and on an alignment device for looking at beam alignment simultaneously in the near-field and far-field that proves useful in both.

Chapter 3 is on implementing a laser-scanning setup for the Mesolens, a giant microscope objective that allows three-dimensional optical sectioning of specimens as large as whole mouse embryos, addressing the problem of the minute field of view available in the laser scanning confocal microscope.

Chapter 4 is about work on a widefield two-photon microscope, much easier to implement than its laser-scanning counterpart and capable of recording images at much higher frame rates, and also less phototoxic than single-photon widefield imaging, advantageous for live cell microscopy.

Chapter 5 is on the use of the interference phenomenon of standing waves in a laser-scanning microscope, improving the axial resolution to better than 100 nm, and generating simultaneous optical sections at different antinodal planes, useful for deducing the three-dimensional morphology of specimens from a single two-dimensional image.

Chapter 6 is a summary of the work presented, and some exciting possibilities for future work.

Chapter 2

A simultaneous near-field and far-field viewer for CARS and two-photon microscopy

2.1   Introduction

Wave-mixing is a nonlinear process that uses two or more input waves to generate an output wave; for example, in a three-wave-mixing process such as sum-frequency generation, two input waves interact within a nonlinear optical material to generate a third wave (the output) at a frequency that is the sum of the frequencies of the two input waves [46]. This process is "nonlinear" because the optical material generates an output that scales nonlinearly with the applied optical field.

Current optical microscopy techniques for biomedical imaging such as sum-frequency generation (SFG) microscopy [65, 66, 67, 68], four-wave mix-

ing microscopy [69, 70, 71, 72], and coherent anti-Stokes Raman scattering microscopy (CARS) [47, 48, 51, 52] routinely use wave-mixing to either provide the excitation beam or to excite the specimen to produce the optical signal. The nonlinear nature of wave-mixing means that it offers intrinsic three-dimensional optical sectioning and low phototoxicity as in two-photon fluorescence microscopy because the signal is confined to the focal plane of the illumination [41, 43], increased penetration depth as a result of reduced scattering when using long excitation wavelengths [73], and label-free detection and imaging of non-fluorescent objects [74, 38].

2.2 Simultaneous near-field and far-field viewer

The four-wave mixing nature of CARS and the three-wave mixing nature of SFG mean that both are multi-photon processes. This dictates that the strength of the generated signal is directly dependent on the temporal and spatial overlap of the incident pulses [53, 75, 76]. These techniques therefore require the standard method of achieving temporal overlap between two pulses, which is through optimization of the SFG output of the beams through a nonlinear crystal [77]. In the case of spatial overlap, the experimental setup normally incorporates a folded beam path made up of a series of folding mirrors for evaluating beam overlap both in the near-field and far-field [78]. In the context of this work, the near field is defined as the point where the beams are just about to enter the microscope scan head, and the far field a point in the microscope specimen plane. The folded beam path, typically 5–10 m, occupies much additional space in a laser system that is

already large and exposes the beam to thermal and mechanical disturbance, which can negatively affect the performance of the microscope.

I have constructed a compact optoelectronic instrument to visualise spatial beam overlap, using a single camera to view the near-field and far-field simultaneously. This is very useful in aligning laser beams such that they are accurately coincident and coaxial because it eliminates the need for aligning the beams in the near-field first, and then doing the same in the far-field, and repeating this several times because aligning for the near-field affects the alignment in the far-field and vice-versa. Apart from speeding up the alignment process, the instrument replaces the folded path, saving space on the optical table and reducing the likelihood of eye or skin exposure to the laser beams. This instrument is simple to build and use and I will show its application in a homebuilt CARS microscope and in a homebuilt SFG-based two-photon laser scanning microscope.

2.3 Wave-mixing-based biomedical imaging

2.3.1 Coherent anti-Stokes Raman scattering microscopy

Coherent anti-Stokes Raman scattering (CARS) is a four-wave mixing process in which a pump beam at a frequency ω_p, a Stokes beam at a frequency ω_S, and a probe beam at a frequency ω_{pr} interact with the specimen and generate an anti-Stokes beam at a new frequency [46]. The anti-Stokes beam is the CARS signal, with a frequency ω_{CARS} [47], and the process is coherent in the sense that the signal propagates in the same direction as the three input beams. The diagram of the CARS process is shown in Fig. 2.1. In the

implementation of CARS in microscopy, the pump and probe beams are at the same frequency ω_p, giving the CARS frequency as $\omega_{CARS} = 2\omega_p - \omega_S$, and the pump and Stokes beams are chosen such that the difference frequency $\omega_p - \omega_S$ coincides with a molecular vibration ω_{vib} within the specimen, greatly enhancing the CARS signal [47, 48].

CARS was first reported by Maker and Terhune in 1965 from experiments on frequency mixing in crystalline and isotropic materials [79]. In the early 1970s, Levenson *et al.* studied the generation of anti-Stokes radiation using wave-mixing in diamond [80, 81], while Byer and co-workers used CARS for
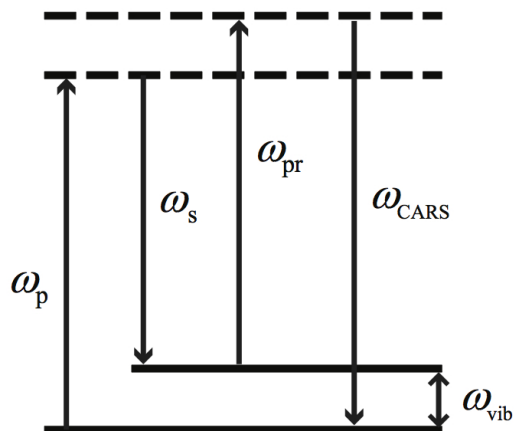
Figure 2.1: Energy-level diagram for the CARS process. The CARS signal is generated from the interaction of molecules with the pump (ω_p), Stokes (ω_S) and probe (ω_{pr}) beams, with a new frequency $\omega_{CARS} = \omega_p - \omega_S + \omega_{pr}$, and is greatly enhanced when the difference frequency $\omega_p - \omega_S$ between the pump and Stokes beams coincides with a molecular vibration ω_{vib}.

spectroscopy [82]. In the early 1980s, Duncan *et al.* were the first to propose and demonstrate CARS microscopy [49, 50], and in 1999, Zumbusch, Holtom and Xie improved the sensitivity of the CARS microscope, making three-dimensional optical sectioning possible [47]. In the study by Zumbusch *et al.*, the Raman shift region was higher than 2000 cm^{-1}. This was extended to the fingerprint region of organic molecules (typically 500–1800 cm^{-1}) by Hashimoto, Araki and Kawata in 2000 [48].

CARS microscopy is particularly useful in imaging specimens without the need for fluorescent staining, since CARS is sensitive to specific molecules and their conformation [48]. Chemical imaging is also possible with confocal Raman microscopy, which uses a high-resolution spectrometer and a confocal pinhole in the detection [83, 84, 85]. But the signal in Raman microscopy is intrinsically weak, requiring the use of high laser powers, typically >10 mW, whereas the high sensitivity in CARS microscopy requires average powers of only ∼0.1 mW, tolerable by most biological specimens [47]. For this reason, CARS microscopy is now routinely being used for label-free imaging in biology and medicine (reviewed by Volkmer [51] and Evans and Xie [52]).

2.3.2 Sum-frequency generation-based two-photon laser scanning microscopy

Another optical microscopy technique that makes use of wave-mixing is sum-frequency generation (SFG)-based two-photon laser scanning microscopy, where SFG is used to generate the source for two-photon excitation. Two-photon absorption, a process in which a molecule makes a transition from ground state to an excited state via the simultaneous (within ∼0.5 fs [39]) ab-

sorption of two photons, was first proposed by Maria Göeppert-Mayer in 1931 [40]. In fluorescence excitation by two-photon absorption, shown in Fig. 2.2, a molecule in its ground state absorbs two photons simultaneously (red arrows), is promoted to an electronically excited state, and returns to the ground state by emission of a photon (green arrow) [21]. As with single-photon-excited fluorescence, the energy of the emitted photon in two-photon-excited fluorescence is lower than the sum of the energies of the absorbed photons because of energy loss due to non-radiative decay, for example, between vibrational energy levels.
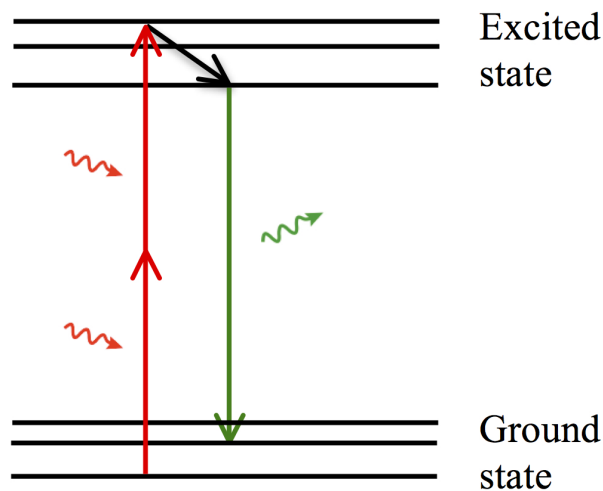
Figure 2.2: Energy-level diagram for fluorescence excitation by two-photon absorption. A molecule in the ground state absorbs two photons simultaneously, is promoted to an electronically excited state, and returns to the ground state by emission of a photon.

After Maiman demonstrated the first working laser in 1960 [86, 87], Kaiser and Garrett performed two-photon excitation in $CaF_2:Eu^{2+}$ crystals in 1961 and generated blue fluorescent light ($\lambda = 425$ nm) from red excitation ($\lambda = 694.3$ nm) [88]. In a paper submitted the same day as Kaiser and Garrett's but published in 1962, Kleinman derived an equation for the two-photon absorption cross section thereby providing a direct estimate of the expected number of fluorescence photons [89]. Kaiser and Garrett's experi-

mental values for photon flux agreed with calculations using Kleinman's theory [88]. Shortly thereafter, Abella reported the observation of two-photon excitation in cesium vapour using the ruby laser [90].

In 1990, shortly after the development of the confocal laser scanning microscope, Denk, Strickler and Webb demonstrated two-photon laser scanning microscopy [41], using a microscope designed by White and Amos [33, 34].

In two-photon laser scanning microscopy, it is only at the focal plane where the photon density is high enough to maximise the probability of two-photon absorption [42]. This means that for fluorescent specimens, only structures at the focal plane will emit fluorescence and as a consequence two-photon excitation has inherent three-dimensional optical sectioning and reduced photobleaching and phototoxicity when considering a volume larger than the focal volume [41, 43, 39, 44]. Two-photon laser scanning microscopy therefore allows imaging studies in intact tissues and in organs of living animals.

Traditionally, the femtosecond-pulsed Ti:sapphire laser is the excitation source for two-photon fluorescence imaging [91]. This laser provides an average power in excess of 1 W and is wavelength-tunable in the range of 680–1080 nm, which makes it ideal for imaging a wide range of endogenous and synthetic fluorophores. However, there are fluorophores such as NAD(P)H and flavoprotein that have an increasing two-photon cross section towards wavelengths shorter than 700 nm [92], not accessible by the Ti:sapphire laser. Therefore, in order to perform efficient two-photon fluorescence imaging on these molecules, non-traditional laser sources are required. One route towards achieving this is by using sum-frequency generation.

In the SFG process, two input waves at frequencies ω_1 and ω_2 interact with a nonlinear material to generate a third wave at a new frequency [46]. The energy-level diagram of the SFG process is shown in Fig. 2.3, where radiation is generated at a frequency $\omega_3 = \omega_1 + \omega_2$. SFG can therefore be applied to produce radiation with a wavelength below 700 nm for two-photon laser scanning microscopy in the ultraviolet range.
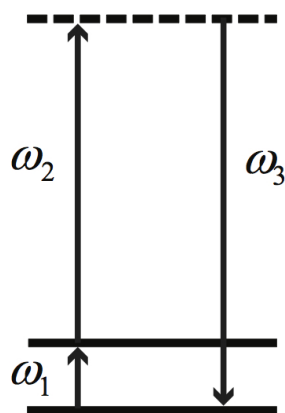
Figure 2.3: Energy-level diagram for sum-frequency generation. Two input beams at frequencies ω_1 and ω_2 interact with a nonlinear material and generate an output beam with frequency $\omega_3 = \omega_1 + \omega_2$.

2.4 Experiment and Results

2.4.1 Near-field and far-field viewer

A key component of the simultaneous near-field and far-field viewer is a 50% beamsplitter (25 BI 00, Comar Instruments, UK) which divides the beams into near-field and far-field components, allowing a microscope image of both beam cross-sections to be formed at a near position and a telescope image to be formed at an infinite distance, as shown in Fig. 2.4. The effective focal length of the combination of a positive and negative lens is given by the equation [93]:

$$\frac{1}{f_e} = \frac{1}{f_p} + \frac{1}{f_n} - \frac{d}{f_p f_n},$$ (2.1)

where f_e is the effective focal length, f_p is the focal length of the positive lens, f_n is the focal length of the negative lens and d is the distance between the two lenses. A far-field optical system is constructed by using a 40 mm positive lens and a 25 mm negative lens separated by a distance of 15 mm in order to give an effective focal length of infinity, as given by Eq. (2.1). A ray diagram of the telephoto combination is shown in Fig. 2.5. By using this lens combination and a 75 mm lens for imaging the beams in the near-field, the near-field and far-field are viewed at the same time using a single camera (DCU223C, Thorlabs GmbH, Germany). To ensure that the camera is not saturated, individual continuously variable neutral density filters (NDL-10C-4, Thorlabs GmbH, Germany) are placed in both the near-field and far-field beam paths to give control of the average power of both sources independently. To check whether the density of the filter altered the beam profiles thereby leading to erroneous alignment, the beam ellipticity was measured as a function of the

optical density.

Before proceeding further, I will first discuss the chromatic dispersion introduced by the wavelength difference between each pair of laser beams in both the CARS and SFG processes. The wavelength-dependence of the refractive index of a transparent optical material is given approximately by the Sellmeier formula, which is of the form:

$$n^2 = A + \frac{B\lambda^2}{\lambda^2 - C} + \frac{D\lambda^2}{\lambda^2 - E}, \tag{2.2}$$

where λ is the wavelength in micrometers and, for the borosilicate glass
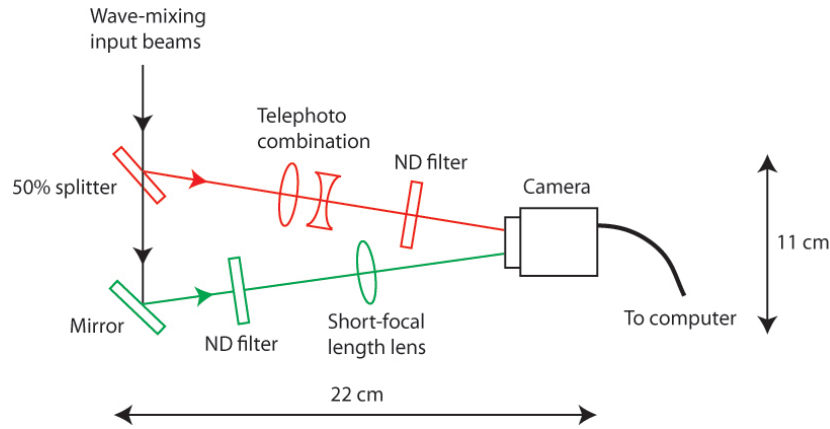
Figure 2.4: Schematic diagram of the near-field and far-field viewer. The telephoto combination is composed of a 40 mm positive lens and a 25 mm negative lens separated by a distance of 15 mm such that the effective focal length is infinity. The short focal length lens is a 75 mm positive lens. The near-field (green) and far-field (red) images of the beam cross-sections are viewed simultaneously using a single camera.

Schott BK7 used in our lenses here, the coefficients are $A = 1.43131380$, $B = 0.84014624$, $C = 1.28897582 \times 10^{-2}$, $D = 0.97506873$ and $E = 100$ [94]. The refractive indices were calculated for the CARS pump and Stokes beams and the SFG input beams, and were used to obtain the focus difference between the beams as they propagate through the lenses.

Comar Instruments specifies a centre wavelength of 587 nm for the focal lengths of the lenses used in the instrument. At this wavelength, Eq. (2.2) gives a refractive index of 1.51682 for BK7. This refractive index was used to obtain the radii of the lenses from the lensmaker's equation [61]:

$$\frac{1}{f} = (n - 1) \left(\frac{1}{R_1} - \frac{1}{R_2} + \frac{(n - 1)d}{n R_1 R_2} \right), \tag{2.3}$$

where f is the focal length, n is the refractive index, R_1 and R_2 are the radii of curvature, and d is the thickness of the lens. To illustrate, we use our 40 mm planoconvex lens as an example. The radius of curvature R_2 for this lens is infinity. Using the refractive index for the centre wavelength, R_1 is therefore obtained to be 20.67280 mm from Eq. (2.3). Using this value for R_1, the wavelength-dependent focal lengths in Eq. (2.3) are then

f=+40 mm   f=-25 mm

Figure 2.5: Ray diagram showing a collimated beam incident on the telephoto combination composed of a 40 mm positive lens and a 25 mm negative lens separated by 15 mm. The effective focal length of the combination is infinity.

Table 2.1: Table of wavelength-dependent indices of refraction for BK7 and the chromatic dispersion introduced as the wave-mixing beams propagate through the lenses. The wavelength-dependent focal lengths are in mm. The calculated focus difference ranging from 182 μm for the CARS pump and Stokes beams to 891 μm for the SFG input beams were compensated by using mode-matching optics before the beams are combined.

λ (μm)	n	f=40 mm focus	f=-25 mm focus	f=75 mm focus
0.752	1.51179	40.39313	-25.24571	75.73712
0.957	1.50812	40.68488	-25.42805	76.28415
1.064	1.50664	40.80373	-25.50233	76.50699
1.538	1.50081	41.27873	-25.79921	77.39762

calculated using the refractive indices from Eq. (2.2). For the CARS pump and Stokes beams of 752 nm and 957 nm, respectively, there is a 291.75-μm focus difference. In the case of the SFG inputs of 1064 nm and 1538 nm, there is a 475.00-μm focus difference. The calculations are summarised for all three lenses in Table 2.1. These focus differences were compensated for by using mode-matching optics in the individual beam paths. In addition to addressing the dispersion in focal lengths, the dispersion in astigmatism was also investigated by varying the centering of the beams on the lenses until the image contrast vanished in the resulting microscope image and quantifying the beam separation as viewed on the alignment device camera.

2.4.2   Application in CARS microscopy

Because of its extremely small footprint of only 22 cm x 11 cm x 16 cm, the near-field and far-field viewer can be inserted easily into the beam path to check that the beams are coaxial and removed again after any necessary adjustment. We used it thus to align and match the pump and Stokes beams in a homebuilt CARS microscope. This microscope had been built previously [95]. I rebuilt it when the Centre for Biophotonics moved to a new building.

The CARS microscope used the output from a picosecond-pulsed Ti:sapphire laser as the pump beam and that from an optical parametric oscillator (OPO) as the Stokes beam. An OPO is made up of a nonlinear crystal into which an incident laser beam (the pump) is focused, generating two output beams (the signal and idler) of lower frequency. The crystal is placed in a cavity made up of mirrors highly reflecting at the signal and/or idler wavelengths and when the gain in the nonlinear interaction exceeds the loss in the cavity, the OPO exceeds threshold and breaks into oscillation, acting like a laser [96]. Because the signal and idler frequencies can be chosen depending on the pump frequency and the properties of the crystal and the cavity, the OPO is very useful as a tunable source of radiation [46].

Figure 2.6 shows a schematic diagram of the homebuilt CARS microscope. After passing through the beamsplitter BS1, 90 % of the output of a Ti:sapphire laser at 752 nm is used to pump an OPO based on a periodically poled lithium niobate (PPLN) crystal 0.5 mm thick and 10 mm long and suitable for pumping at around around 750 nm. The crystal was antireflection coated at both the pump wavelength and the calculated signal wavelength tuning range of 920–1200 nm. This OPO signal was used as

the Stokes beam for the CARS process. As the OPO signal wavelength is temperature-dependent [97], the crystal was mounted in an oven to allow operation at elevated temperatures of up to 200 °C. The bow-tie cavity consisted of four CaF_2 cavity mirrors (Laseroptik GmbH, Germany): two highly reflective curved mirrors (CM1 and CM2) with a radius of curvature of 100 mm, one plane highly reflective end mirror (M8) and one output coupling mirror (OC). The pump beam was focused into the crystal to a spot size of ~13 μm in radius, and the combination of a half-wave plate (HW) and a polarizer (P) were employed as a variable attenuator for the incident pump power.
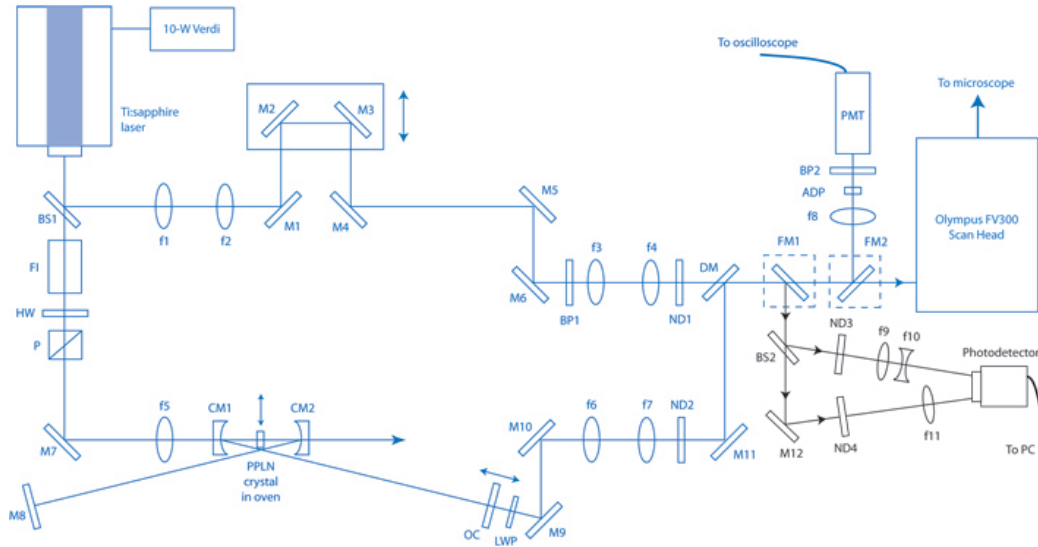
Figure 2.6: Schematic diagram of the homebuilt CARS microscope (blue) incorporating the near-field and far-field viewer (black). BS1=90/10 beamsplitter, f1-f8=planoconcave lenses, M1-M11=highly reflective mirrors for near IR, FI=Faraday isolator, HW=half-wave plate, P=polarizer, CM1-2=OPO cavity mirrors, PPLN=periodically poled lithium niobate crystal for parametric generation, OC=output coupler, LWP=long-wave pass filter, BP1=Semrock FF01-769/41 band pass filter, BP2=Chroma HQ430/50m-2p band pass filter, ND1-2=neutral density filters, DM=dichroic mirror, FM1-2=flip-mounted mirrors, ADP=ammonium dihydrogen phosphate crystal for sum-frequency generation, PMT=photomultiplier tube.

The remaining 10 % of the total power from the Ti:sapphire laser was used as the pump beam in the CARS process. This was picked off by the beamsplitter BS1 and guided through an optical delay line to enable overlapping spatially and temporally with the OPO signal beam, which was used

as the Stokes beam. The beams were combined at the dichroic mirror DM (z850dcspxr, Chroma Technology, USA) and focused onto an ADP crystal (Type I, United Crystals, USA) to optimise the temporal overlap between the two pulses by maximising the sum-frequency generated signal detected by a photomultiplier tube (1P28, Hamamatsu Photonics).

For achieving spatial beam overlap using the near-field and far-field viewer, the near field is defined as the point where the beams are just about to enter the microscope scan head and the far field to be at the microscope specimen plane. Mirrors M5 and M6 were used to adjust the pump beam, and M10 and M11 for the Stokes beam, to aid in the alignment process. By viewing the near-field and far-field beams on the same camera, achieving spatial overlap and proper matching of beam diameters is straightforward and quickly done, producing a CARS image when the beams are coupled into the microscope scan head. The beam alignment is then further optimized to obtain maximum image contrast as viewed on the microscope. The device is therefore a useful tool in speeding up the CARS imaging process.

Figure 2.7 shows the spatially overlapped Ti:sapphire and OPO near-field and far-field beams as viewed on the camera. The near-field and far-field viewer was found to be sensitive to very small changes in the alignment of either beam, making it highly useful both for initial alignment setting and periodic maintenance. To investigate whether the density of the filters in the beam path altered the beam profiles thereby leading to erroneous alignment, the beam ellipticity was measured as a function of optical density using a beam profiler (BP209-IR, Thorlabs, Ltd., UK). It was observed that the neutral density filter had no appreciable effect on the beam profiles. By
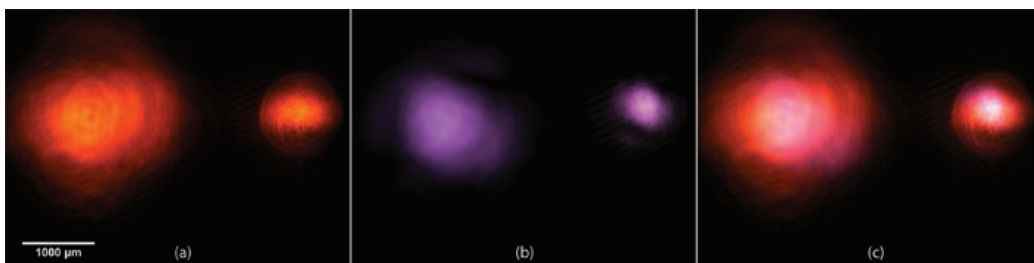
Figure 2.7: (*a*) The Ti:sapphire beam (orange) with the OPO blocked, (*b*) the OPO beam (violet) with the Ti:sapphire blocked, and (*c*) the Ti:sapphire and OPO beams both unblocked, showing spatial overlap as viewed on the camera. The far-field is on the left side of each panel while the near-field is on the right.

evaluating the shift in the beam positions on the camera image as the beam alignment is adjusted, it was observed that the pump and Stokes beams need to be coaxial to better than 400 μrad, otherwise the CARS image contrast vanishes and CARS image disappears. In addition, by varying the centering of the beams on the lenses, it was observed that the CARS image disappears if the beams are off-center by 50 μm, corresponding to a center-to-center distance of separation of 380 μm between the beams as viewed on the near-field and far-field viewer.

A sample image from the homebuilt CARS microscope is shown in Fig. 2.8. A fresh unstained mouse ear tissue was imaged using a pump wavelength of 752 nm and a Stokes wavelength of 957 nm, resulting in a Raman shift of 2850 cm^{-1} that coincides with the CH$_2$ stretching vibration, suitable for imaging lipids in biological specimens [52]. The image shows a cluster of lipid-rich se-

baceous glands surrounding a hair follicle. The image size is 512 x 512 pixels taken at 1 frame per second. The pump power and Stokes power incident on the specimen were approximately 20 mW and 40 mW, respectively.
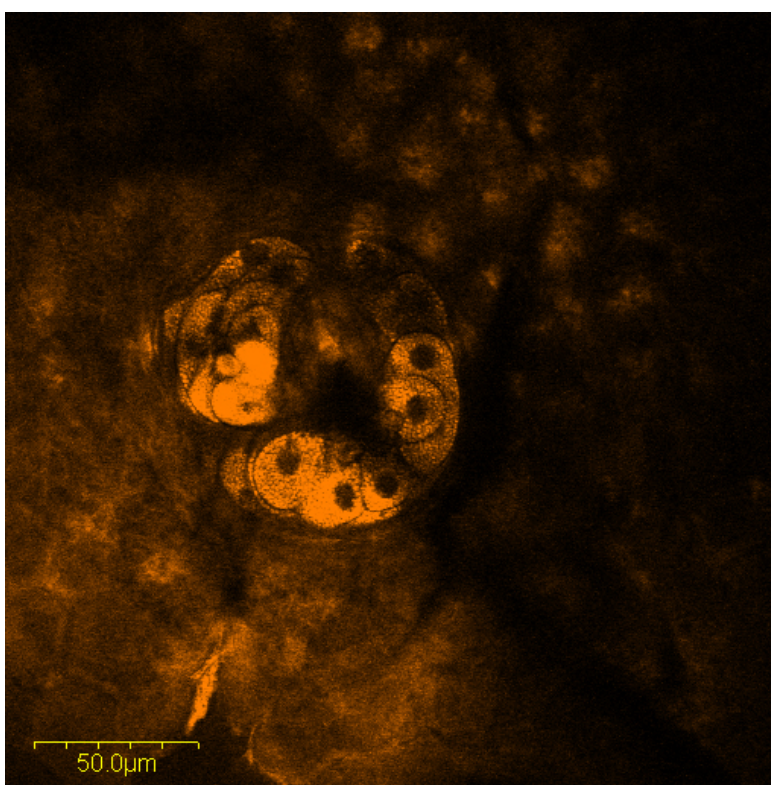
Figure 2.8: A CARS image showing a cluster of sebaceous glands in a fresh unstained mouse ear tissue. The image was taken at a Raman shift of 2850 cm^{-1} to coincide with the CH$_2$ stretching vibration.

2.4.3 Application in SFG-based two-photon laser scanning microscopy

The near-field and far-field viewer was also used to align and match the input beams in a homebuilt SFG-based two-photon laser scanning microscope. A schematic diagram of the microscope is shown in Fig. 2.9. A mode-locked Yb-doped fibre laser (Femtopower 1060-2-s, Fianium, UK) served as the pump source, with an average power of 2 W and repetition rate of 80 MHz, pulses of 260 fs duration at a wavelength of 1064 nm and with a spectral width of 12 nm. The laser output was split into two components by the 50/50 beamsplitter BS1. The first beam was used to synchronously pump an OPO, the output of which was recombined spatially and temporally with the second pump beam in a second nonlinear optical crystal to perform sum-frequency generation.

A periodically poled lithium niobate (PPLN) crystal 3 mm long was used to provide maximum output power at an OPO signal wavelength of range of 1450–1600 nm. All of the mirrors in the OPO resonator were highly reflective at the signal wavelength except for the output coupler OC, which was 50 % reflecting at the signal wavelength. The crystal was kept in a home-made oven at a temperature of 100 °C to ensure fixed signal wavelength operation. The OPO provided a 260 fs output which was continuously tunable between 1450 and 1600 nm and had an output power of ∼200 mW.

Figure 2.9: Schematic diagram of the homebuilt two-photon microscope (blue) incorporating the near-field and far-field viewer (black). M1-M7=highly reflective mirrors for IR, FI=Faraday isolator, HW1-4=half-wave plates, BS1=50% splitter, f1-f8=planoconcave lenses, CM1-2=OPO cavity mirrors, PPLN1=periodically poled lithium niobate crystal for parametric generation, OC=output coupler, PPLN2=periodically poled lithium niobate crystal for sum-frequency generation, M8-11=highly reflective mirrors for VIS, Galvos=galvanometer scanning mirrors, PMT=photomultiplier tube.

The remaining 50 % of the pump beam was steered towards a trombone arrangement of two dielectric mirrors highly reflective at the pump wavelength (M6 and M7), mounted on a linear translation stage to create a time delay. This permitted a temporal displacement of the pump pulse, which was used to synchronise it with the signal pulse from the OPO within a second

PPLN crystal for sum-frequency generation.

As with the CARS microscope, the near-field and far-field viewer was used to achieve beam overlap and proper matching of beam diameters. Before combining in the second PPLN crystal for sum-frequency generation, the pump and OPO signal beams were diverted into the viewer by the flip mirror FM. Since the laser wavelengths were much longer in this microscope, an IR disk (VRC2, Thorlabs GmbH, Germany) was used in place of the camera. Achieving spatial overlap and matching of beam diameters was again straightforward, and with the flip mirror out of the way, the beams were combined in the PPLN crystal. With the pump wavelength of 1064 nm and the OPO signal wavelength range of 1450–1600 nm, the sum-frequency generated output had a wavelength range of 622–636 nm, well-suited for imaging fluorophores with peak two-photon excitation in the ultraviolet region [98]. The beam alignment was then further optimised to obtain maximum power as measured with a power meter. This SFG output was then coupled into a homebuilt laser scanning microscope, serving as the laser source for two-photon excitation of fluorescence.

A periscope system (M8 and M9) was used to steer the SFG signal towards the scanning mirrors (Galvos). The scan head comprised of two galvanometer-driven mirrors (6215HB, Cambridge Technology, USA) and was mounted on an elevated breadboard at the back of the microscope. The beam from the scanning mirrors was focused through an achromatic doublet (f7) with a focal length of 80 mm (80 DQ 25, Comar, UK), which served as the scan lens. The scan lens was positioned 80 mm from the midway point between the scanning mirrors on one side and 80 mm from the intermediate

image plane of the tube lens on the other side. The tube lens (not shown) was an achromatic doublet with a focal length of 160 mm (160 DQ 25, Comar, UK), placed 240 mm from the scan lens and 160 mm from the back aperture of the objective lens. The scan lens and tube lens combination doubled the beam width so that the back aperture of the objective lens was consistently overfilled.

A 20x/0.75 N.A. dry objective lens (Plan Fluor, Nikon, UK) was used in the excitation path and a 0.9 N.A. condenser lens was used in the transmission path to collect the fluorescence signal. A 700 nm short-pass filter (et700sp-2p8, Chroma, USA) and a 550 nm bandpass filter (NT65-704, Edmund Optics Ltd., York, UK) were used to block the excitation wavelength and any harmonic generation, such that only fluorescence from the specimens was transmitted. A photomultiplier tube (RFI-QL-30F, Thorn EMI, London, UK) was used to collect the fluorescence signal and the freely available MPScope software developed by Nguyen *et al.* [99] was used to control the scanning mirrors and for image capture.

Figure 2.10 shows a sample image from the homebuilt two-photon fluorescence microscope using the sum-frequency-generated laser source for the excitation. The excitation wavelength used was 630 nm, suitable for imaging two-photon autofluorescence in the ultraviolet region. The image size is 512 x 512 pixels, taken at 2 frames per second. The figure shows the radula of the marine snail *Littorina*, a rasp-like structure used for feeding [100]. The arrangement of chitinous teeth on the radula ribbon is clearly visible.
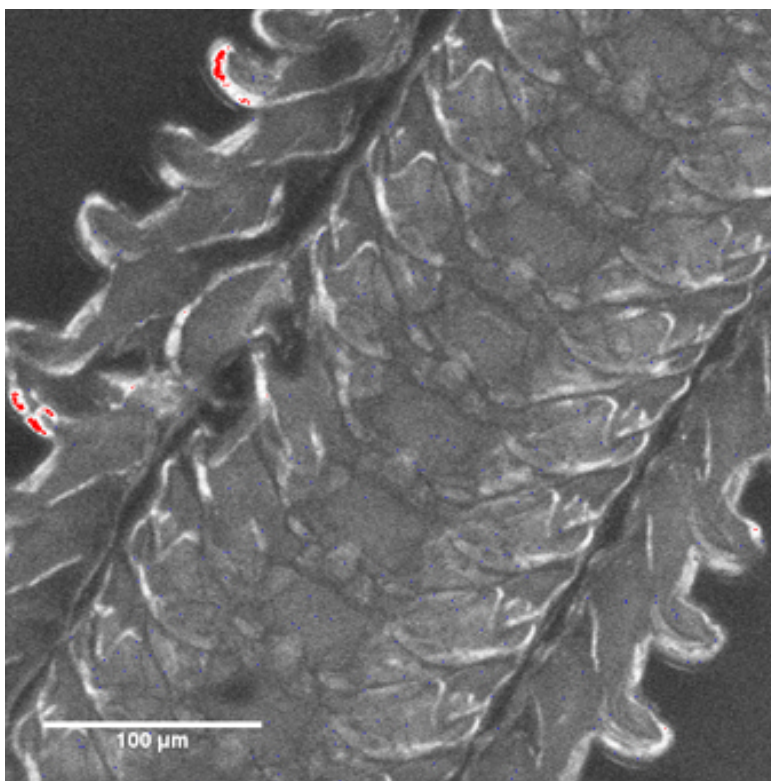
Figure 2.10: A two-photon autofluorescence image of the radula of a snail, a rasp-like structure used for feeding. The image was taken using the sum-frequency generated laser source for two-photon excitation, at a wavelength of 630 nm. The arrangement of chitinous teeth on the radula ribbon is clearly visible.

The successful application of the simultaneous near-field and far-field in aligning the wave-mixing input beams in CARS and SFG as described above illustrate that it is a useful device in speeding up wave-mixing experiments. In addition, the use of a telephoto combination and a short-focal length lens is a simple and effective way of viewing the near-field and far-field beams

71

simultaneously on a single camera or detection screen, making it a compact device, saving premium space on an optical table by replacing the folded beam path normally used for viewing wave-mixed beams in the far-field.

2.5 Conclusion

In this chapter, I have described a simultaneous near-field and far-field viewer to evaluate spatial overlap in wave-mixing experiments. Wave-mixing is a multi-photon process, and this dictates that the strength of the generated signal directly depends on the temporal and spatial overlap of the incident pulses.

I have shown that by using a telephoto combination and a short focal length lens, one is able to view the near-field and far-field beams simultaneously on a single camera or detection screen. The instrument is compact, saving space in the optical table by replacing the folded beam path for evaluating spatial overlap in the far-field.

I have demonstrated the successful application of this near-field and far-field viewer by incorporating it in a homebuilt CARS microscope and a homebuilt two-photon laser scanning microscope. Using a specimen of fresh unstained mouse ear tissue, I have shown that the CARS microscope is useful for label-free imaging of biological specimens. Using a specimen of the radula of a snail, I have also shown that the homebuilt SFG-based two-photon microscope is appropriate for two-photon excitation of fluorescence in the ultraviolet region.

The near-field and far-field viewer is simple to build and use, and its

application in the above-mentioned microscopes have speeded up the process of beam alignment and actual imaging.

Chapter 3

A laser-scanning confocal system using the Mesolens

The Mesolens is a giant microscope objective with a 5 mm field of view, designed for imaging large-volume specimens. In this chapter, I will discuss the work that I did in implementing a laser-scanning configuration for the Mesolens, allowing the acquisition of optical sections of large specimens for three-dimensional imaging. I will also discuss the possibility of two-photon excitation with the Mesolens, by showing calculations of pulse dispersion and two-photon absorption using some common dyes.

3.1   Introduction

Ever since its development in the late 1980s [29, 30, 31, 32, 33, 34], the confocal laser scanning microscope has been highly successful in its role as a standard tool in biomedical imaging because it produces images of good

quality and allows three-dimensional reconstruction of the specimen from optical sections. However, owing to the fact that microscope objectives are constructed in such a way that aberrations are minimised, that is, objective lenses are built small, the field of view of any microscope, including the confocal laser-scanning microscope, is small and so in order to image large specimens such as intact embryos [101, 102] or the brain [103, 104, 105], hundreds of images need to be stitched together, a process that requires considerable time and effort. It is important to be able to image large specimens such as intact mouse embryos in order to study the organism as a whole, focusing not only on the individual systems within, but also on the interplay between these systems, which plays a major role in the development of the organism.

It is for this reason that William Bradshaw Amos, co-developer of the confocal laser scanning microscope at the Medical Research Council Laboratory of Molecular Biology in Cambridge, and Esmond Reid, an expert in lens design, built the Mesolens, a giant microscope objective that can image large specimens in a single snapshot. The Mesolens in a laser-scanning implementation extends the range of the confocal microscope to cover larger volumes, with every cell in a piece of tissue or an entire mouse embryo recorded in three dimensions and with detail in the sub-cellular level.

Previous approaches to three-dimensional imaging of large-volume specimens include optical projection tomography (OPT) and selective plane illumination microscopy (SPIM) or light sheet microscopy.

OPT was developed by James Sharpe and co-workers in 2002 at the Medical Research Council Human Genetics Unit in Edinburgh [106, 107]. In OPT,

75

the specimen is rotated through 360° around a single axis while being held in position for imaging by a microscope. The specimen is supported in a transparent cylinder of agarose gel and rotated through angular steps of 0.9°. A digital image of the static specimen is taken at each of the 400 rotated positions. After the 400 images are taken, virtual sections are reconstructed using a back-projection algorithm and producing high-resolution representations of sections through the specimen. Although OPT has proved very useful in biological studies because of its ability to view gene expression in three dimensions for specimen volumes of up to several cm^3 [108], it does not provide sub-cellular resolution [107], having a lateral resolution of 6.77 μm [108].

SPIM or scanned light sheet microscopy was developed by Ernst Stelzer and co-workers in 2004 at the European Molecular Biology Laboratory in Heidelberg [109, 110, 111, 112, 113]. In light sheet microscopy, the specimen is embedded in a cylinder of agarose gel and the agarose cylinder is immersed in an aqueous medium filling a chamber. Optical sectioning is achieved by illuminating the specimen along a separate optical path perpendicular to the detection axis. The excitation light is focused by a cylindrical lens to a sheet of light that illuminates only the focal plane of the detection objective, and therefore no out-of-focus fluorescence is generated, resulting in optical sectioning. In this way light sheet microscopy is similar to confocal laser scanning microscopy with the difference that only the plane being observed is illuminated and so photobleaching is localised. Unlike OPT, light sheet microscopy achieves a lateral resolution below 1 μm, the resolution being 1.06, 0.44, and 0.32 μm for 10x/0.3 N.A., 40x/0.8 N.A., and

100x/1.0 N.A. water-immersion objectives respectively [114]. However, light sheet microscopy is best suited for imaging highly transparent specimens, as absorption and scattering lead to non-homogeneous illumination. An alternative is inverted selective plane illumination microscopy (iSPIM), developed by Hari Shroff and co-workers in 2011 at the National Institutes of Health in Bethesda [115]. In iSPIM, two water-immersion objectives (one to illuminate the specimen with a light sheet and one to collect the resulting fluorescence) are mounted orthogonally onto a z translation stage placed above the specimen, allowing high-speed non-invasive imaging of live specimens, scanning a volume every 2 seconds. Because it was developed as a direct add-on to an inverted microscope, iSPIM can image specimens prepared on coverslips, as in conventional microscopy. However, it may be difficult to overlap the objective focal planes in iSPIM.

3.1.1 Optical sectioning and axial resolution

In order to perform three-dimensional optical sectioning, a microscope needs to have an objective that has good resolution in the axial direction. The axial resolution, measured along the optical axis of the of the microscope, is inversely proportional to the square of the numerical aperture [116]:

$$Axial\ resolution = \frac{2n\lambda}{N.A.^2},$$
(3.1)

where n is the refractive index, λ is the wavelength of light, and N.A. is the numerical aperture, which is the product of the refractive index and the sine of the half-angle θ of the cone of light accepted by the objective lens:

$$N.A. = nsin\theta.$$
(3.2)

Because of the inverse square dependence on the numerical aperture, the axial resolution deteriorates rapidly with low N.A.

However, in order to image specimens of large volume, the objective lens magnification needs to be low, typically 4x, to increase the field of view, and conventional low-magnification objectives have a low numerical aperture (typically 0.1–0.2). These objectives therefore do not have good axial resolution and are not suited for three-dimensional microscopy, as the axial slices will be too thick. A graph of axial resolution versus numerical aperture is shown in Fig. 3.1, where the index of refraction is taken to be 1.5 and the wavelength is 500 nm.
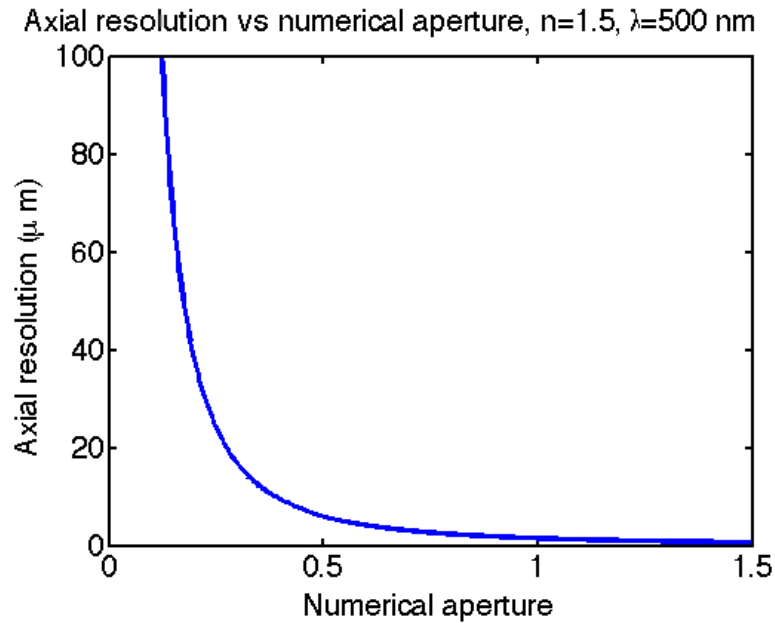
Figure 3.1: Axial resolution versus numerical aperture for light of wavelength 500 nm and a medium refractive index of 1.5. The axial resolution is inversely proportional to the numerical aperture and deteriorates rapidly for low-magnification objectives, which have a typical numerical aperture of 0.1–0.2.

Amos and Reid designed the Mesolens such that it should have a high numerical aperture along with its large field of view. At a magnification of 4x and a working distance of 3 mm, the Mesolens field of view is 5–6 mm, sufficient to image a whole mouse embryo in a single shot. The Mesolens is a multi-immersion lens, making it suitable for diverse imaging conditions. More importantly, its numerical aperture of 0.47 means that the axial resolution at a wavelength of 500 nm and using oil immersion (n=1.5) is 6.8 μm, sufficient for three-dimensional optical sectioning of specimens such as whole mouse

embryos. In addition, the lateral resolution, given by [116]

$$Lateral\ resolution = \frac{1.22\lambda}{2N.A.}, \tag{3.3}$$

is 0.65 μm at a wavelength of 500 nm, which means that structures within the cell can be resolved. The large field of view necessitates that the lens itself is large: it is about 70 cm long and 8 cm in diameter. Since a large lens is accompanied by magnified aberration problems, the design incorporates multiple elements (14 lens elements) shaped to a high standard and positioned to better than 3 μm centration accuracy to achieve a high degree of correction. Figure 3.2 shows the multi-element design of the Mesolens.

Figure 3.2: The Mesolens design. The Mesolens is made up of 14 lens elements shaped to a high standard and positioned to better than 3 μm cent ration accuracy. The lens is about 70 cm long and 8 cm in diameter.

3.1.2 The Mesolens as a camera lens

Before its incorporation in a laser-scanning configuration at the University of Strathclyde, the Mesolens was used as a camera lens for widefield epi-fluorescence and brightfield imaging at the Medical Research Council (MRC) Laboratory of Molecular Biology (LMB) in Cambridge, where it was developed. A Hamamatsu EMCCD camera (C9100-13 ImageEM) was used to acquire images. Because of the high light collection efficiency as a result of

the Mesolens' high numerical aperture, short exposure times in the order of milliseconds were sufficient (for the camera), even for specimens with weak signals. Figure 3.3 shows a camera image from the Mesolens, showing a large area of an embryonic rat brain explant (transferred to a nutrient medium). The specimen was prepared by Yvonne Vallis at the MRC LMB. The neurones have been labelled with Alexa 488 staining beta III tubulin (a neuron-specific marker) to emit green fluorescence, the astrocytes (star-shaped glial cells) with Alexa 546 staining GFAP (glial fibrillary acidic protein) to emit red, and the nuclei with DAPI to emit blue. Figure 3.3a shows the 5 mm field of view, showing a large number of neurons, astrocytes, and nuclei. Figure 3.3b shows the field when zooming in by a factor of 10, with the fine structural detail preserved and resolved.
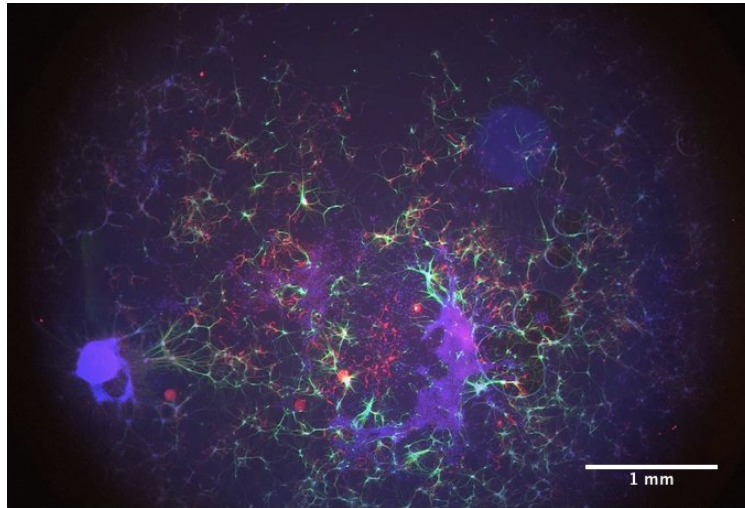
(a)
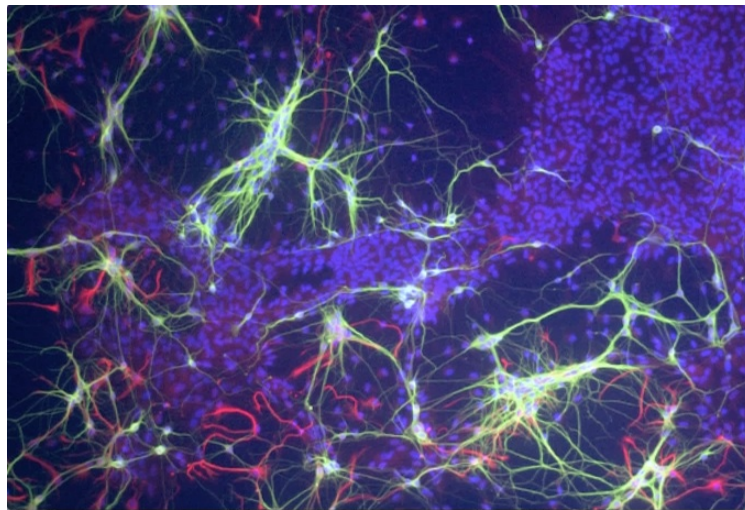
(b)

Figure 3.3: The Mesolens as a camera lens. (*a*) Fluorescence image of an embryonic rat brain explant showing neurons stained with Alexa 488 (green), astrocytes stained with Alexa 546 (red), and nuclei stained with DAPI (blue) in the 5 mm field of view. (*b*) The 10x magnified image of neurons shows fine detail. Specimen prepared by Yvonne Vallis, MRC LMB. Image © 2010 William Bradshaw Amos.

Although the Mesolens as a camera lens produced images of very high quality, what was needed was for it to be used in a laser-scanning confocal system, where the potential to do optical sectioning because of the high numerical aperture will be realised. This work was to be done at the University of Strathclyde, where Amos and Reid collaborated with Gail McConnell and John Dempster at the Strathclyde Institute of Pharmacy and Biomedical Sciences.

3.2 The Mesolens in a laser-scanning confocal system

From the outset, I was responsible for setting up the Mesolens for laser-scanned confocal imaging, performing early tests to trace the source of jitter problems with the galvanometer mirrors, adding a module for differential phase contrast in the transmission path, and obtaining the very first confocal images of a whole mouse embryo. After this, I also added a second laser source in the excitation path and performed two-colour imaging on doubly-labeled mouse embryos from collaborators at the Victor Chang Cardiac Research Institute in Sydney.

After Amos brought the Mesolens to the University of Strathclyde in 2011, McConnell enlisted the services of Gerard Drinkwater in building the scanner electronics and Dempster wrote the MesoScan software for image acquisition and for controlling the scanning mirrors.

3.2.1 Imaging in camera mode

We first tested the Mesolens as a camera lens after it arrived in Strathclyde from Cambridge. Among the interesting specimens we used were mouse ear specimens prepared by Owain Millington, injected with 0.1 μm FluoSpheres polystyrene beads (Molecular Probes) loaded with a proprietary dye to emit green fluorescence in the presence of blue excitation. The ears were harvested at various times after the injection of the beads. In this experiment, we would expect to see the lymphatic vessels being lit up by the beads as these vessels serve an important role in the body's immune system, draining extracellular fluid and antigens through the secondary lymphoid organs, where lymphocyte activation occurs [117]. During lymphocyte activation, B cells and T cells are activated by antigen-specific receptors on their cell surface, causing them to proliferate and differentiate; for example, T cells become cytotoxic T cells, able to destroy any cell that poses a threat to the host organism [118].

Figure 3.4 shows a series of epi-fluorescence images of mouse ears harvested 5 min, 1 hour, and 6 hours after injection with green fluorescent FluoSpheres beads. As expected, the lymphatic vessels which drain the ear of extracellular fluid, antigens and debris are clearly visible, with the vessel network being particularly well-defined in Fig. 3.4a, an image of the ear specimen harvested 5 minutes after injection. Figure 3.4a shows a very quick uptake of the beads by the lymphatic vessels, after only 5 minutes, with less of the vessel network being visible after 1 hour (Fig. 3.4b), and with the vessels appearing to have been drained after 6 hours (Fig. 3.4c). This type of experiment gives us an idea of the time frames involved in the circulatory function of the lymphatic system.
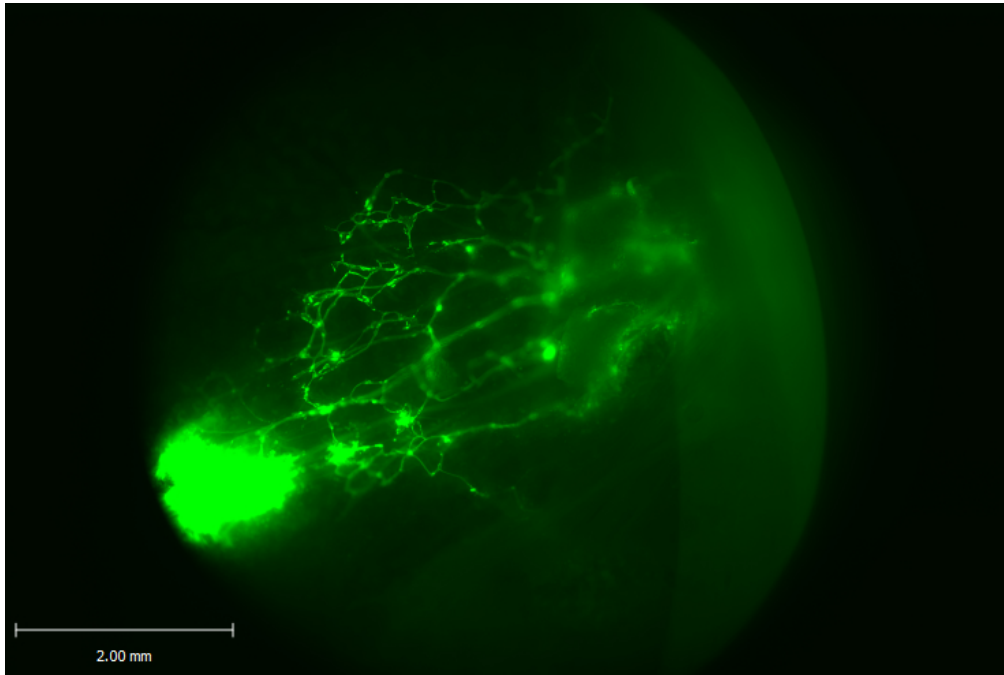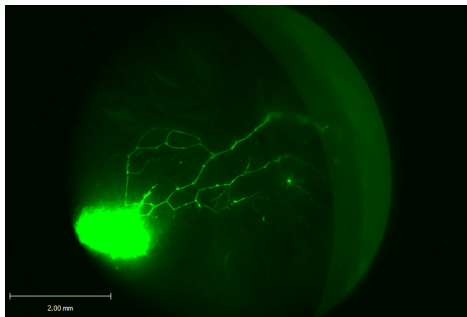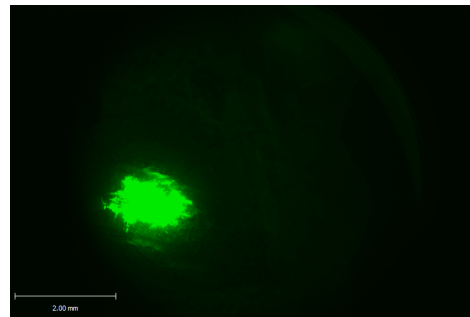
Figure 3.4: Epi-fluorescence images of mouse ear specimens harvested (a) 5 minutes, (b) 1 hour and (c) 6 hours after being injected with green fluorescent FluoSpheres beads. The network of lymphatic vessels which drain the ear is clearly visible, with the ear specimen harvested 5 minutes after injection showing a very quick uptake of the beads. The vessels appear to have been drained after 6 hours. Scale bar=2 mm.

3.2.2 Laser-scanned confocal imaging

Amos, McConnell and I built the laser-scanning confocal setup for the Mesolens shown in Fig. 3.5. The excitation beam is directed by steering mirrors (BB1-E02, Thorlabs, Ltd., UK) through an 8-mm focal length lens into an 80/30 beamsplitter that served as the chromatic splitter. The beamsplitter is not wavelength-selective and is positioned in such a way that the 30 % reflecting side is facing the excitation beam and therefore transmits most of the emission signal. The 8-mm focal length lens and the 1,000-mm focal length lens before the galvanometer mirrors serve to magnify the excitation beam to have the 30-mm diameter required at the Mesolens back aperture. The galvanometer mirrors (Cambridge Technology, USA) that scan the beam across the specimen have a 50-mm clear aperture and are made of beryllium, making them quite heavy. The mirrors have been back-thinned by milling so as to reduce their mass. The fluorescence signal emitted by the specimen is collected by the Mesolens and takes the reverse path with respect to that of the excitation, is transmitted by the 80/30 beamsplitter and enlarged by a 200-mm focal length lens before reaching the confocal aperture, which is placed far from the scanning optics. This was done so that it is possible to use an ordinary iris diaphragm, with the aperture as large as a millimetre, making it easy to align the beam, without the need for micro-manipulators. Behind the aperture is the photomultiplier tube for detecting the fluorescence signal (PMM02, Thorlabs Ltd., UK), and various emission filters can be used to detect the desired fluorescence wavelength.
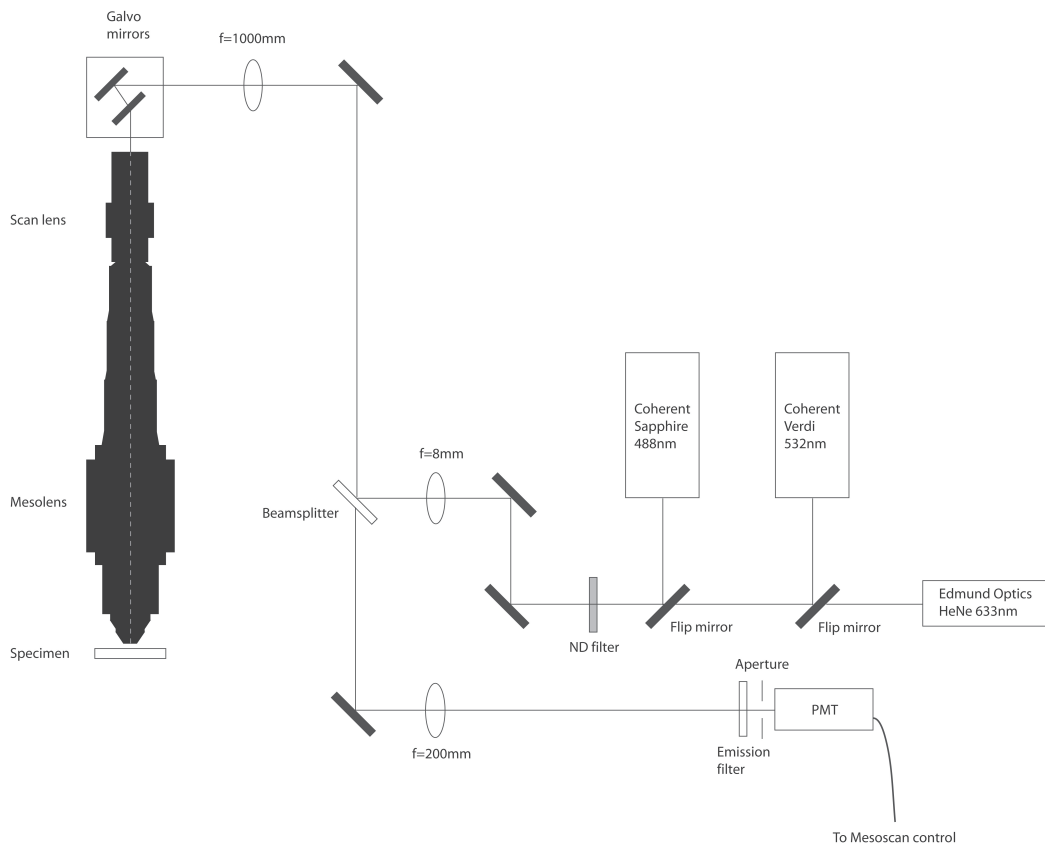
Figure 3.5: Schematic diagram of the Mesolens in a laser-scanning setup. The galvanometer mirrors have a clear aperture of 50 mm and a lens of 1 m focal length is used to magnify the beam in order to have the 30-mm diameter required at the Mesolens back aperture. The scan lens is an f-theta lens, which ensures that the input and output beams are directly proportional, allowing the scanning mirrors to run at constant angular velocity, greatly simplifying the control electronics. The whole setup is homebuilt, including the scanner electronics and the MesoScan software.

A laser-scanned image of an electron-beam-fabricated resolution target is
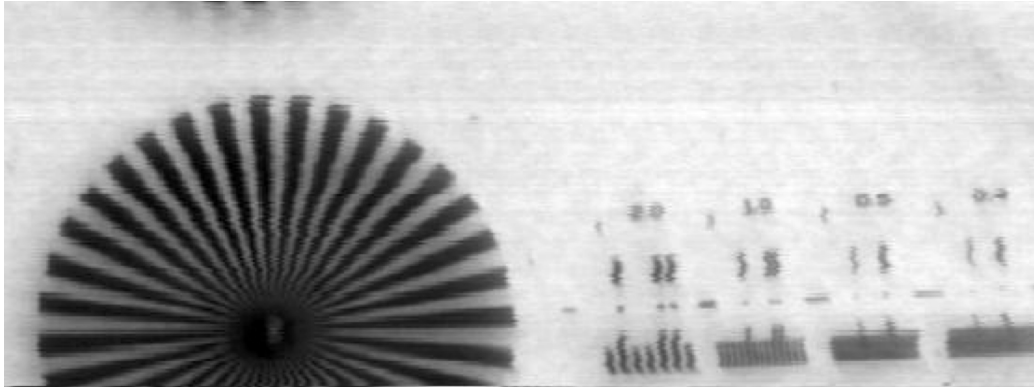
Figure 3.6: Laser-scanned image of electron-beam-fabricated target imaged in reflection mode. The image shows jitter but the grating second from left is a 1-μm grating, which demonstrates that 1-μm objects are resolved.

shown in Fig. 3.6, imaged by reflection at a wavelength of 488 nm. The image shows jitter, which limits the resolution but the grating second from the left is a 1-μm grating, demonstrating that 1-μm objects are resolved. This actual lateral resolution of 1 μm is less than the theoretical value of 0.65 μm, but it is enough to demonstrate the capabilities of the Mesolens in confocal mode.

The jitter can be studied more closely by performing a line scan on a specimen with many vertical lines across the field of view. I prepared such a specimen by vertically rubbing a piece of aluminium with fine emery paper. Normally, if the system were free of jitter, a line scan will produce regular straight lines, without deviation. Also, if there is mirror jitter corresponding to a variation of a few microradians and line scans are obtained at increasing zoom settings, that is, by scanning the mirrors through increasingly smaller angles, the effect of the jitter in producing apparent horizontal deviation of

the vertical lines would be proportional to the zoom. I obtained line scans of the rubbed aluminium specimen at a frequency of 100 Hz using zoom settings of 4.5x, 20x, 50x and 100x, shown in Fig. 3.7. As expected, the horizontal deviation in the vertical lines of the line scan output is proportional to the zoom, indicating that the jitter is in the fast galvo mirror that does the horizontal scan.

(a)

(b)

(c)

(d)
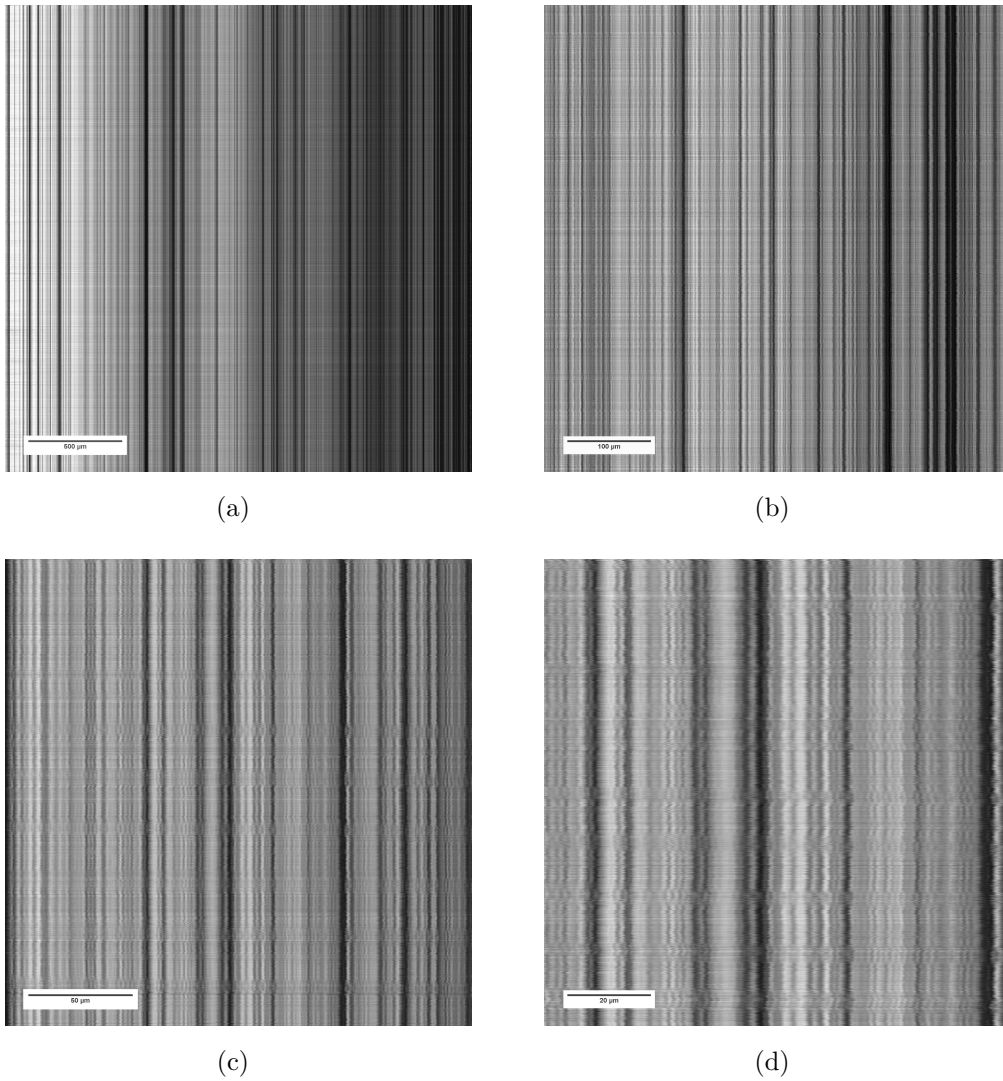
Figure 3.7: Line scans from a piece of aluminium rubbed vertically with fine emery. The horizontal deviation in the vertical lines is proportional to the zoom setting, increasing as the line scan is obtained at a zoom of (*a*) 4.5x, (*b*) 20x, (*c*) 50x, and (*d*) 100x, indicating that the jitter is originating from the mirror.

91

A comparison of line scans at the same zoom setting of 100x but taken at frequencies of 10 Hz and 100 Hz, shown in Fig. 3.8, shows that there is less deviation from the vertical in the 100 Hz scan than in the 10 Hz scan. This can be attributed to the fact that a faster oscillation at 100 Hz is near mechanical resonance and as resonance is approached, there is a tendency for the mirrors to follow a sinusoidal scan with reduced jitter effects from the bearings.

(a)   (b)
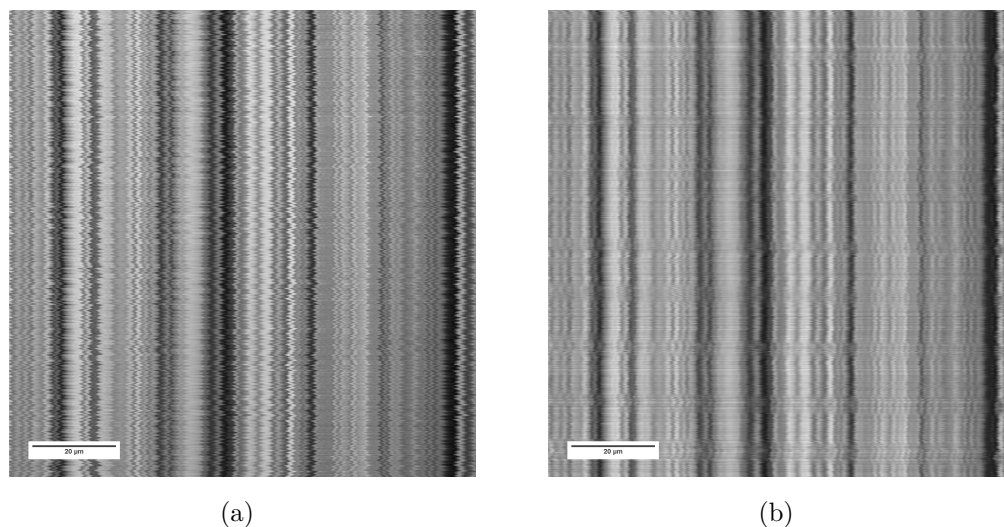
Figure 3.8: Line scans at the same zoom setting but different frequencies. 100x zoom line scans obtained at (*a*) 10 Hz and (*b*) 100 Hz show that there is less horizontal deviation in the vertical lines when using a faster scan. This suggests that a faster oscillation of 100 Hz is near mechanical resonance where there is a tendency for the mirrors to follow a sinusoidal scan with a reduced jitter effect from the bearings.

In spite of the problems with mirror jitter, which is markedly present at high zoom settings, for example at 100x zoom as in Fig. 3.8, the fact that the jitter effect is minimal at a low zoom, for example at 4.5x zoom as in Fig. 3.7a, meant that it was possible to get good confocal images of a whole mouse embryo, at a zoom of 1, using the confocal Mesolens system in its current condition.

Ch3-Supplementary Video 1 shows a three-dimensional reconstruction of a 10-day-old mouse embryo. Although the images obtained for the reconstruction are not in high resolution, the video shows that with the Mesolens in confocal laser-scanning mode, there is very good optical sectioning, otherwise the axial resolution would be too low and it would not be possible to make a 3D reconstruction.

Figure 3.9 shows a confocal image of a whole mouse embryo, obtained in January 2012. The specimen is a 10-day-old embryo, prepared as acridine orange whole mount, and fixed and cleared. The immersion medium is glycerol and the laser wavelength used for fluorescence excitation was 488 nm, with an average power of about 30 μW at the specimen. A 520 nm bandpass filter (FF01-520/15-25, Semrock, Inc., USA) was used as the emission filter. The Mesolens takes 100 seconds to record an image that is 3,000 $\times$ 3,000 pixels in size. The field of view is 5 mm, sufficient to show the whole organism, but the fine detail in the image makes the microanatomy clearly visible also. Structures such as the developing heart at the centre of the image can be clearly made out, as well as the circular structure at the bottom right of the image which is the developing ear, and the many muscle blocks, or somites, on the left hand side. Midway between the developing heart and the

ear are the developing lung and and branchial artery, with the white balloon shape being the gill arch. Above the developing heart, in close proximity to the muscle blocks, is the canal of the spinal cord. The fact that all these structures can be studied in an intact organism at different stages of its development means that the Mesolens in confocal mode is certain to have a huge impact in developmental biology [119, 120].

Figure 3.9: Confocal image of a whole mouse embryo stained with acridine orange, taken with the Mesolens. The field of view is 5 mm, showing the whole organism, but with the microanatomy clearly visible, such as the developing heart in the very centre, the developing ear, visible as a circular structure in the lower right, and the series of muscle blocks on the left hand side.

Equally important is the fact that the lateral resolution of the Mesolens

is below 1 μm; 0.65 μm theoretically, and at least 1 μm in practice from the resolution target image in Fig. 3.6. This means that if we zoom in on the image of the whole embryo in Fig. 3.9, we should be able to see sub-cellular structures also.

Ch3-Supplementary Video 2 is a movie showing a confocal image of the embryo, starting with the image of the whole organism shown in Fig. 3.9, and then zooming in to see fine detail. The full field of view shows the mouse embryo with structures such as the neural tube on the left, several somites, and the developing heart in the centre. Zooming in makes it possible to see individual cells, with the bright dots being individual Golgi apparatuses inside the cells. Thus, with the confocal Mesolens, we were able to record the whole microanatomy of the embryo and then zoom in to see sub-cellular detail. To our knowledge, this was the first record of such an observation in optical microscopy.

Figure 3.10 is a zoomed-in image of Fig. 3.9, showing a close-up view in the region of the developing heart. It is clear from the figure that in addition to the ventricles of the heart, which show up as long streaks of developing muscle fibres, the Golgi apparatuses are also clearly visible, showing up as countless white dots in the image, sometimes flattened and sometimes in the shape of a crescent. The Mesolens is therefore able to show the organism in full, with its microanatomy intact, and also the structures in the sub-cellular level.
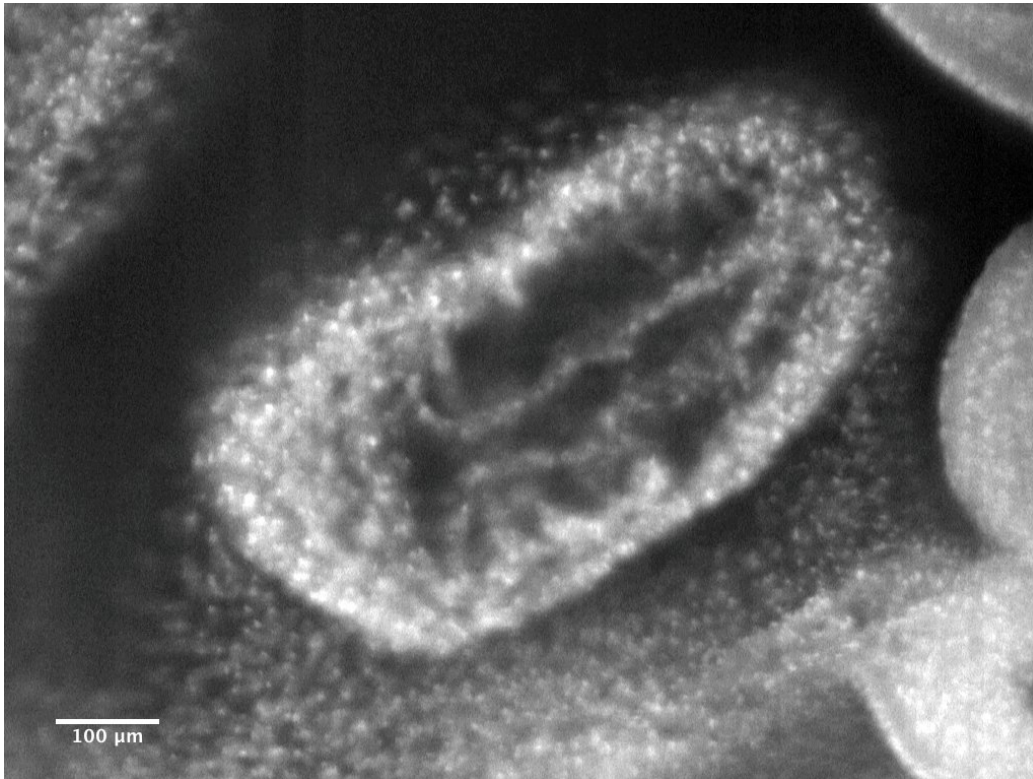
Figure 3.10: Close-up view of the region of the developing heart, obtained by zooming in on the full-frame image in Fig. 3.9. In addition to the ventricles, which are long streaks of developing muscle fibres, the Golgi apparatus is clearly visible also, with flattened or crescent shapes sometimes visible. The Mesolens is therefore able to resolve structures within the cell.

The mirror jitter evident in Figs. 3.7 and 3.8 affect the lateral resolution of the Mesolens image. But in the axial direction, there is no jitter, since there is no jitter in the stepper motor that moves the specimen stage. Therefore, the axial resolution of the Mesolens is unaffected and should be near the

theoretical value of 6.8 μm. This means that obtaining optical sections with 10 μm separation, for example, should show marked changes in the whole-embryo image. I obtained a series of full-frame images of the mouse embryo in this way, fifteen slices in total, moving the specimen by 10 μm each time. Figure 3.11 shows a montage of the stacks. As expected, this series of images show marked differentiation in the structures visible in the microanatomy of the embryo as the specimen is moved axially, and therefore we are able to perform three-dimensional optical sectioning with the Mesolens. As the laser-scanning Mesolens performs just like a regular confocal microscope in that the excitation beam is spread out over a volume that extends outside of the focal plane, we would expect to see more photo-bleaching relative to SPIM, where the excitation is confined within the light sheet. However, the ability to use specimens prepared in the conventional way (in coverslips, as opposed to being embedded in a cylinder of agarose) and to image not only those specimens that are highly transparent constitute a desirable advantage.
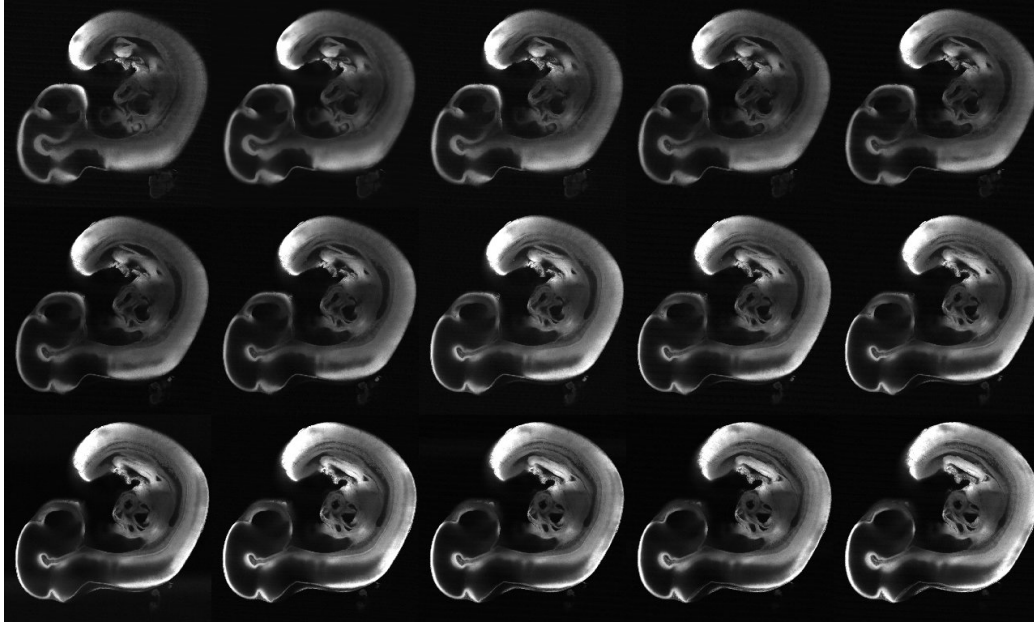
Figure 3.11: Montage showing 15 confocal images taken by moving the embryo 10 μm each step axially. The field of view is 5 mm. There is a marked difference in the microanatomy recorded in each section, demonstrating the expected depth discrimination with the Mesolens and allowing three-dimensional reconstruction as in a conventional confocal microscope.

Two years after we obtained the first confocal images with the Mesolens, the mirror jitter had been minimised in such a way that lateral and axial resolution measurements were possible. Using 1 μm fluorescent beads as test specimens, the lateral resolution was measured to be 0.9 μm and the axial resolution was measured to be 8 μm. Figures 3.12a and 3.12b show plots of the intensity profiles through one bead in the lateral and axial direction, respectively. These data were obtained by Johanna Tragardh, who joined

the Mesolens project in 2013.
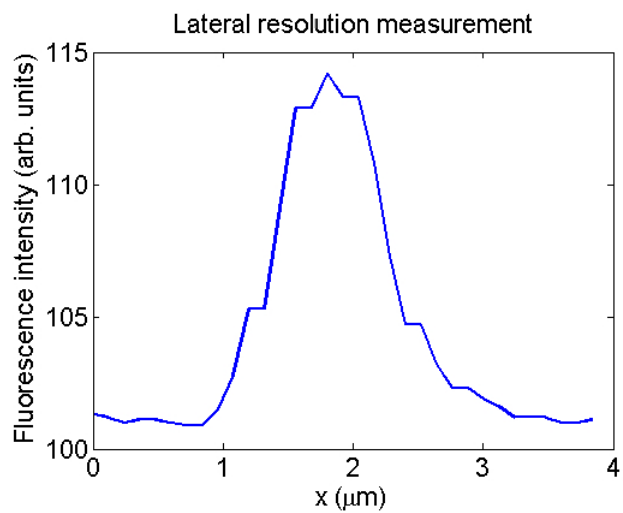
(a)
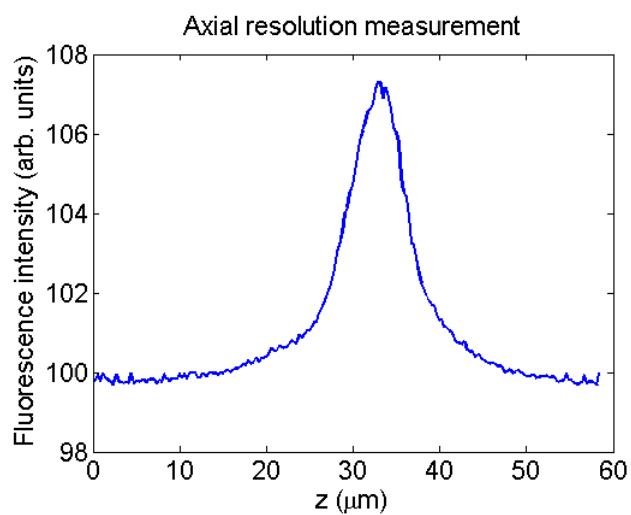
(b)

Figure 3.12: Plots of the intensity profiles through a 1 μm fluorescent bead in the *(a)* lateral and *(b)* axial direction. The lateral resolution was measured to be 0.9 μm and the axial resolution 8 μm. Data obtained by Johanna Tragardh, who joined the Mesolens project in 2013.

3.2.3 Two-colour imaging

In the schematic diagram presented in Fig. 3.5, in addition to the 488-nm (Sapphire 488 LP, Coherent, Inc., USA) laser for blue excitation, I have added 532-nm (Verdi-V5, Coherent, Inc., USA) and 633-nm (Edmund Optics, Inc., USA) for green and red excitation and two- or three-colour fluorescence imaging. Table 3.1 shows the transmission data for the Mesolens confocal setup at measured using commonly-available laser wavelengths for fluorescence excitation. Typical values in the visible spectrum are 10–20 %, acceptable for fluorescence imaging since the laser power can easily be adjusted in order to obtain the fluorescence image. Transmission data in the infrared region (780 and 800 nm) are well below 10 % because all the optical elements were optimised for fluorescence excitation using visible wavelengths.

Because of Amos's collaborative links with the Victor Chang Cardiac Research Institute in Sydney, we obtained doubly-labeled 11-day-old mouse embryo specimens prepared by Gavin Chapman. These specimens were labeled with smooth muscle actin (SMA) antibody stain for green fluorescence from muscles and platelet endothelial cell adhesion molecule (PECAM) antibody stain for red fluorescence from vessels. I imaged these specimens using the 488-nm laser for blue excitation of the SMA stain and the 532-nm laser for green excitation of the PECAM stain, using a 520-nm emission filter (FF01-520/15-25, Semrock, USA) in front of the confocal aperture for green fluorescence and a 620-nm filter (FF01-620/14-25, Semrock, USA) for red fluorescence. The image size was 1000×1000 pixels. Figure 3.13 shows the resulting two-colour fluorescence image, where the green lines of muscle in the somites are clearly visible, as well as the network of blood vessels.

Table 3.1: Table of transmission percentages for the Mesolens confocal setup at different excitation wavelengths. Transmission values of 10–20 % are acceptable because the output power from the laser can be adjusted accordingly in order to obtain a fluorescence image. Transmission at 780 and 800 nm is below 10 % because the optics optimised for visible wavelengths at the time the measurements were made.

λ (nm)	Transmission
488	20 %
532	10 %
633	10 %
780	6 %
800	4 %

Fluorescence imaging of specimens labelled with multiple dyes is very useful in biomedical imaging because this allows the study of independent proteins simultaneously and provides more structural and/or functional information [121], allowing one to see the relationship between the distributions of different proteins and to evaluate whether their functions are linked. Therefore with additional laser sources in the Mesolens confocal system for fluorescence excitation of multiple stains, even more information is available which maximises the use of fluorescent specimens and speeds up experimental studies where more than one structure or function is investigated.
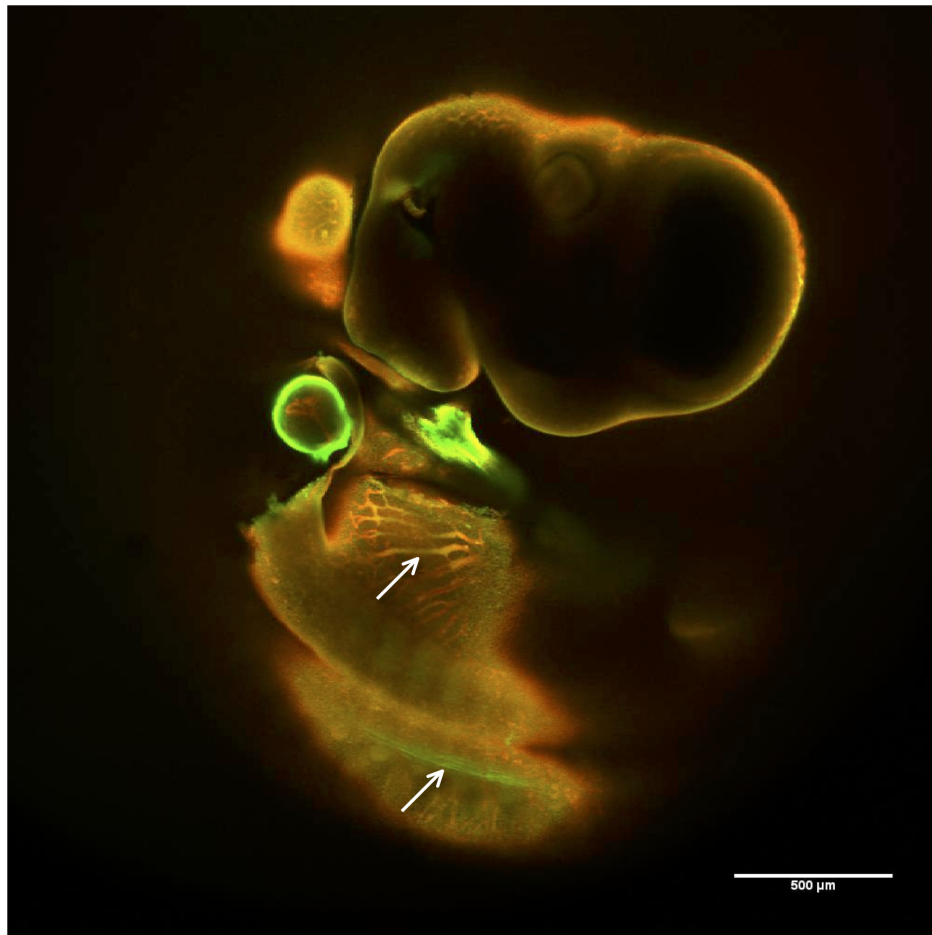
Figure 3.13: Two-colour fluorescence imaging using the Mesolens. Fluorescence image of an 11-day-old mouse embryo specimen labeled with smooth muscle actin (SMA) antibody stain (green) and platelet endothelial cell adhesion molecule (PECAM) antibody stain (red) for vessels. The green lines of muscle in the somites are clearly visible (bottom arrow), as well as the network of blood vessels (top arrow).

3.3 Towards two-photon microscopy with the Mesolens

With a laser-scanning confocal system for the Mesolens in place, it is natural to think of two-photon excitation as a possible next step. Two-photon excitation using the Mesolens is an attractive prospect firstly because it will extend the penetration depth, as the Mesolens was designed for imaging specimens of large volume that will therefore be thick in most cases, and secondly because two-photon excitation has inherent sectioning capability, with the excitation confined to the focal plane which also leads to less photodamage and photo-toxicity in the regions of the specimen that are outside the focal plane, with the result that imaging specimens *in vivo* is possible [41, 43, 42, 122, 44].

The next-generation version of the Mesolens, which allows rapid switching between camera and confocal laser scanning modes, is currently being built by Amos and Reid. This newer version will come in a folded configuration, shown in Fig. 3.14a. This design has 21 optical elements in total. Most manufacturers do not make the prescription of their lenses available and so this calculation is usually impossible, but in the case of the Mesolens, the batch-specific Sellmeier coefficients of each lens element are known, permitting a reliable calculation and prediction of pulse stretching.

In order to perform two-photon excitation of fluorescence, in which a fluorophore absorbs two photons simultaneously and is promoted to an electronic excited state from where it decays back into the ground state by emission of fluorescence, the photon density required is about six orders of magnitude larger than that in single-photon excitation [44]. In two-photon excitation,

the number n_a of photons absorbed per fluorophore per pulse depends on the pulse duration τ, repetition rate $\Delta\nu$, average incident laser power P_{av}, and the numerical aperture $N.A.$ of the objective lens, given by [41]

$$n_a \approx \frac{P_{av}^2 \delta}{\tau \Delta\nu^2} \left(\frac{N.A.^2}{2\hbar c \lambda} \right), \tag{3.4}$$

where c is the speed of light, $\hbar$ is Planck's constant divided by 2π, and δ is the two-photon cross section. Pulse stretching is therefore undesirable in two-photon excitation because it reduces the probability of two-photon absorption.

I have made calculations of pulse stretching as a 150-fs input pulse propagates through all 21 individual elements of this design, using the equation [123]:

$$\tau(L) = \tau_0 \sqrt{1 + \left(\frac{8aL \; ln(2)}{\tau_0^2} \right)^2}, \tag{3.5}$$

with

$$a = \frac{\lambda^3}{4\pi c^2} \frac{d^2 n(\lambda)}{d\lambda_0^2}, \tag{3.6}$$

where τ_0 is the input pulse duration, λ is the wavelength, L is the thickness of the optical element, and $d^2 n(\lambda)/d\lambda_0^2$ is the Sellmeier equation [94]. The plot of the output pulse duration as a function of wavelength given in Fig. 3.14b shows an output pulse duration of around 250 fs at 800 nm, and so two-photon excitation should be possible as far as the issue of pulse stretching is concerned. I have also made calculations for the two-photon absorption

of 80 μM fluorescein (a reference standard dye) in water (pH 11), 100 μM DiI (a membrane dye) in methanol, and Fluo-3 (a calcium indicator). For these calculations, I used the output pulse durations computed using Eq. 3.5 above, an average power of 20 mW at the specimen, and two-photon excitation cross-section data from Xu and Webb [124] and Cornell University's Developmental Resource for Biophysical Imaging Optoelectronics [125]. The calculated two-photon absorption values, shown in Fig. 3.14c, show that it should be possible to do two-photon excitation with the Mesolens, with the right choice of wavelength depending on the dye.

(a)
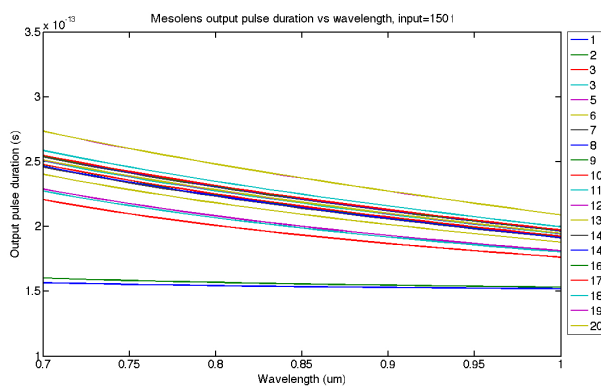
(b)
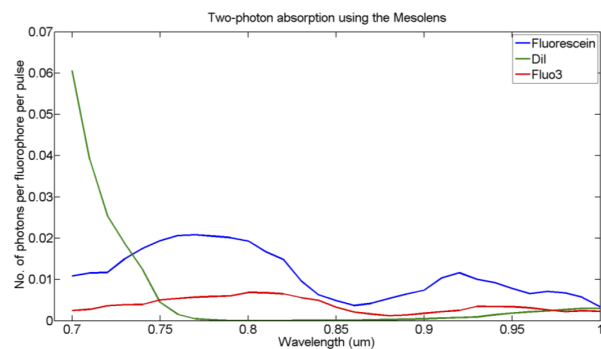
(c)

Figure 3.14: (*a*) Mesolens design with 21 elements. (*b*) Pulse duration after each element (indicated by numbers) vs wavelength for an input pulse of 150 fs. The output pulse duration at 800 nm is ∼250 fs. (*c*) Two-photon absorption of fluorescein, DiI and Fluo-3, calculated using data in *b*.

3.4 Conclusion

In this chapter, I have discussed the work that I did in setting up the Mesolens for laser-scanning confocal microscopy. I began with a time-lapse experiment on the lymphatic vessels in a whole mouse ear specimen, using the Mesolens as a camera lens, and showed that with the 5-mm field of view, it is possible to visualise the network of lymphatic vessels in the whole mouse ear.

I then presented the confocal system that we built, and after discussing some of the early issues with jitter in the scanning mirrors, I presented the first confocal images obtained using the lens. These images contain a wealth of information owing to the fact that the field of view of 5 mm is able to show a whole organism, and the lateral resolution of at least 1 μm (the theoretical lateral resolution is 0.65 μm, but this has slightly been made worse by the jitter) is able to show structures in the sub-cellular domain.

I have discussed my results with two-colour fluorescence imaging using doubly-labeled mouse embryos, showing muscle fibres and blood vessels in a single image. The sequential visualisation of independent proteins in a single specimen is important because it maximises the use of a limited resource (the intact mouse embryo) and allows the visualisation of the relationship between the distributions of different proteins and the evaluation of whether their functions are linked.

Finally, I have ended this chapter by presenting some relevant calculations pertaining to the use of the Mesolens for two-photon excitation of fluorescence, where its usefulness will be even more magnified owing to the advantages of two-photon excitation such as deep penetration, excitation confinement, and reduced photodamage and phototoxicity.

109

Chapter 4

A widefield microscope for two-photon imaging without scanning

In this chapter, I will discuss work on a widefield microscope for two-photon fluorescence imaging without scanning. Being widefield, the image acquisition is limited only by the speed of the camera and I will show its use in imaging fast calcium events in live neurones at 100 frames per second.

4.1   Introduction

4.1.1   Speeding up two-photon microscopy

After the development of the confocal laser scanning microscope in the late 1980s [29, 30, 31, 32, 33, 34], Denk, Strickler and Webb demonstrated two-

photon laser scanning microscopy in 1990 [41]. Denk *et al.* used the faster scan head developed at the Medical Research Council Laboratory of Molecular Biology in Cambridge by White, Amos, Durbin and Fordham [33, 34] combined with a femtosecond-pulsed dye laser. In 1992, shortly after the report by Denk *et al.*, White, Amos, Curley and Ferguson were the first to perform two-photon excitation of fluorescence using the now-standard Ti:sapphire laser at the University of Strathclyde [91].

For a significant number of two-photon absorption events to occur, in which a dye molecule absorbs two long-wavelength photons simultaneously, the photon density must be about a million times that required in single-photon excitation [44]. The number n_a of photons absorbed per fluorophore per pulse depends on the pulse duration τ, repetition rate $\Delta\nu$, average incident laser power P_{av}, and the numerical aperture $N.A.$ of the objective lens, and is given by [41]:

$$n_a \approx \frac{P_{av}^2 \delta}{\tau \Delta\nu^2} \left(\frac{N.A.^2}{2\hbar c\lambda} \right), \tag{4.1}$$

where c is the speed of light, $\hbar$ is Planck's constant divided by 2π and δ is the two-photon cross section. The very high photon density required in two-photon excitation is fulfilled by focusing a pulsed illumination beam, where during the peak of the pulse the instantaneous intensities at the beam focus are high enough to deliver two photons virtually simultaneously to within the absorption cross section of the molecule, bringing it to its excited state and consequently the excitation energy is emitted as fluorescence [42].

Two-photon laser scanning microscopy was adopted in many fields of biomedicine immediately after its introduction [43]. Its chief advantages are deeper tissue imaging compared with single-photon excitation owing to less tissue absorption and scattering for infrared light than for light at shorter wavelengths [126, 122], the creation of optical sections by the combination of a conical beam geometry with an excitation proportional to the square of the local illumination intensity thereby confining fluorescence excitation at the focal plane [42], and the more efficient utilization of scattered emission than is possible in a confocal microscope because confocal detection is not required [39, 44]. The chief drawbacks were the slow scanning speed, which restricted the original instruments to a rate of approximately one image per second, often unusable for electrophysiology where millisecond time resolution may be needed, and the high rate of photo-bleaching if the laser intensity was increased [127, 128, 129].

To overcome the slowness, faster scanning mirrors have been used [130], and parallelism has been achieved in two-photon imaging by the use of slit scanning [131] or the scanning of multiple foci, preferably uncorrelated in time [132, 133, 134]. Two-photon light-sheet microscopy has also been used to increase the rate of imaging [135], but because scattering and absorption in the specimen causes inhomogeneous illumination, this method is best suited to highly transparent tissue volumes.

More recently, Konnerth and co-workers developed the powerful method of low-power temporal oversampling (LOTOS)-based two-photon scanning, achieving image acquisition rates of as high as 1,000 frames per second [136, 137]. LOTOS uses an acoustic-optic deflector for the fast x-scan. When a

conventional 12-kHz resonant mirror is used for the x-scan instead of the acoustic-optic deflector, LOTOS-based two-photon imaging acquires images at a rate of 200 frames per second [138]. But the much reduced image size in LOTOS, corresponding to 28 μm $\times$ 9 μm at 1,000 frames per second and a 27–42 μm field of view at 200 frames per second, means that it is best suited to imaging single dendritic spines. Also, the method is technically challenging and complex and comes at a high cost.

A simple and elegant approach to two-photon illumination is to use a large stationary spot of light from a mode-locked femtosecond-pulsed laser in a conventional microscope, and to image the emission from structures within the spot. This method was not favoured by Fittinghoff et al, who were apparently the first to try it [132], was shown by Hwang *et al.* to provide images of good quality [139]. Although Hwang *et al.* imaged medically-important specimens such as a tissue phantom composed of a nude mouse skin and a retinal specimen of Alzheimer's disease from a transgenic mouse model, their work seems to have only a limited effect on normal practice in general, possibly because the illuminated spot was no greater than 60 μm in diameter and the loss of optical sectioning has been regarded as serious. I will show how their unexpected result of having obtained useful images from widefield two-photon excitation can be explained by the vastly-increased exposure time in a widefield microscope, where a camera is used instead of a photomultiplier tube. This chapter extends the approach by Hwang *et al.*, increasing the field size to a diameter of 90 μm and concentrating on fast transients in living neurones, a specimen where the potentially unlimited time resolution of the stationary beam can be evaluated, assuming a fluorophore with a sufficiently

fast response rate is used and that a sensor of high sensitivity is used for fluorescence detection.

4.1.2 Excitation and detection of two-photon fluorescence

Awareness of the high peak intensities required for two-photon excitation has probably deterred experimentation on widefield two-photon microscopy. Here I will compare the excitation and detection parameters in the widefield two-photon microscope with that in a standard laser scanning two-photon microscope.

For the laser source, let us assume a wavelength of λ=780 nm, repetition frequency $\Delta\nu$=80 MHz and pulse duration τ=140 fs with a 60x/0.9 N.A. water dipping lens, as used in the live cell imaging experiments discussed in the succeeding sections. Let us also assume that pulse stretching is negligible, and is similar in both the laser scanning and widefield microscopes.

In a laser scanning two-photon microscope, the time-averaged power at the specimen plane is typically P_{av}=15 mW. The peak power is then given by [140]:

$$
\begin{aligned}
P_{peak} &= \frac{P_{av}}{\tau\Delta\nu} \\
&= \frac{15 \times 10^{-3}\ W}{(140 \times 10^{-15}\ s)(80 \times 10^{6}\ Hz)} \\
&= 1.34\ kW.
\end{aligned}
\tag{4.2}
$$

The beam waist radius of the excitation laser at the specimen plane is given by [141]

$$
w_0 = \frac{\lambda}{\pi\theta},
\tag{4.3}
$$

114

where θ is the half-angle of the beam divergence which is a function of the numerical aperture,

$$N.A. = nsin\theta. \tag{4.4}$$

For the 60x/0.9 N.A. water dipping lens (n=1.33), Eq. 4.3 for the beam waist radius therefore becomes

$$
\begin{aligned}
w_0 &= \frac{\lambda}{\pi sin^{-1}(N.A./n)} \\
&= \frac{780 \times 10^{-9}\ m}{\pi sin^{-1}(0.9/1.33)} \\
&= 334 \times 10^{-9}\ m.
\end{aligned}
$$

This gives the peak intensity in the laser-scanned excitation spot as

$$
\begin{aligned}
I_{peak} &= \frac{P_{peak}}{\pi w_0^2} \tag{4.5} \\
&= \frac{1.34 \times 10^3\ W}{\pi (334 \times 10^{-9}\ m)^2} \\
&= 3.82 \times 10^{15}\ W/m^2.
\end{aligned}
$$

In the widefield two-photon microscope, a time-averaged power of P_{av}=360 mW is used at the specimen plane which, from Eq. 4.2 when considering the same pulse duration and pulse repetition frequency, gives a peak power of

$$
\begin{aligned}
P_{peak} &= \frac{360 \times 10^{-3}\ W}{(140 \times 10^{-15}\ s)(80 \times 10^6\ Hz)} \\
&= 32\ kW.
\end{aligned}
$$

Instead of focusing to a diffraction limited spot by overfilling the back aperture, the beam is instead focused to a small spot near the back aperture to obtain a weakly focusing spot at the specimen plane with a radius of w_0=45

μm. This gives the peak intensity in the widefield two-photon microscope as

$$
\begin{aligned}
I_{peak} &= \frac{P_{peak}}{\pi w_0{}^2} \\
&= \frac{32 \times 10^3 \ W}{\pi (45 \times 10^{-6} \ m)^2} \\
&= 5.03 \times 10^{12} \ W/m^2.
\end{aligned}
$$

Note that this peak intensity is approximately three orders of magnitude lower than the peak intensity for a point-scanning two-photon microscope.

This substantially lower peak excitation intensity is compensated by the fact that the beam is not scanned in a widefield microscope. By continuously irradiating across the whole field, a much longer integration time can be used for collecting the fluorescence signal.

In a laser scanning two-photon microscope, the point dwell time is typically T=5 μs and since the fluorescence lifetime of the fluorophore is very short (in the order of ns), it is safe to assume that fluorescence is generated and collected over the same 5 μs duration. For an image that is 640 $\times$ 560 pixels, which is the same image size used in the widefield setup described in this chapter, this point dwell time yields a frame rate of 0.56 Hz. The excitation radiation applied to the specimen for each point is therefore I_{peak} $\times$ T=1.91 $\times$ 10^{10} W$\cdot$s/m^2.

In the widefield two-photon microscope, the specimen is continuously irradiated with the femtosecond-pulsed laser radiation, but in comparison with the laser scanning two-photon microscope, the dwell time can be considered to be equivalent to the frame rate of the camera. For images taken at 100 Hz (i.e. a T=10 ms exposure time), the excitation radiation applied to the specimen during the image capture is I_{peak} $\times$ T=5.03 $\times$ 10^{10} W$\cdot$s/m^2. The overall

total excitation radiation applied in the widefield two-photon microscope is therefore similar to that used in laser scanning two-photon microscopy.

In summary, when using widefield excitation, the peak intensity is orders of magnitude lower than in laser scanning excitation and the total excitation radiation applied is similar. By collecting the light on all the pixels in parallel we achieve long per pixel integration times, and can collect enough photons for imaging at fast frame rates. Moreover, the quantum efficiency of an sCMOS camera, which is 60 % for the Zyla 5.5 camera that we used [142], is likely to be higher than the efficiency of a photomultiplier tube used in a laser scanning two-photon microscope ($\sim$30 %), therefore offering the possibility of high detection sensitivity.

4.2   Experiment

4.2.1   Experimental setup

The simple widefield two-photon microscope was configured as shown in Fig. 4.1. A commercial upright epi-fluorescence microscope (BX51WI, Olympus) was modified for two-photon excitation. A chromatic reflector (FF670-SDi01, Semrock) reflecting wavelengths longer than 670 nm and transmitting shorter wavelengths was used to direct excitation towards the specimen and to transmit fluorescence. A cooled sCMOS camera (Zyla 5.5, Andor) controlled by a PC running the freely available software WinFluor [143] was used to detect fluorescence from the specimen. To block the laser source from the camera and to ensure that only the fluorescence signal contributed to the image, 680 nm and 694 nm short-wave pass filters (FF01-680/SP and FF01-

694/SP, Semrock) were used in the collection path. A commercially available wavelength-tunable femtosecond-pulsed Ti:Sapphire laser (Chameleon Ultra II, Coherent) was used as the excitation source. This laser delivered a maximum time-averaged power of 2.3 W at a repetition rate of 80 MHz with a pulse duration of 140 fs. The weakly divergent output from the Ti:Sapphire laser was steered using a pair of highly reflecting mirrors (BB1-E03, Thorlabs) and then attenuated using a variable neutral density filter (NDC-25C-4, Thorlabs) and expanded to a diameter of 22 mm using a plano-convex lens pair of focal lengths f=+35 mm and f=+100 mm (LA1027-B and LA1509-B, Thorlabs). The beam height was changed using a two-mirror periscope (BB1-E03, Thorlabs) to permit coupling of the laser into the upright microscope. At height, the beam was focused using a single plano-convex lens of focal length f=+75 mm (LA1608-B, Thorlabs), with the beam waist close to the back aperture of the objective lens. This produced a wide and weakly-focused beam in the specimen plane which did not contribute significantly to the optical sectioning power. A beam diameter was found experimentally which allowed excitation of the dye but with minimal photo-bleaching at a time-averaged laser power of 360 mW at a wavelength of 780 nm. The illuminated area then had a diameter of 90 μm and a 1.6$\times$ magnifier was used to fill the camera sensor. All live cell imaging data presented here used a 60x/0.9 N.A. water dipping lens (Olympus). With the Zyla 5.5 camera pixel size of 6.5 μm and a total magnification of 96$\times$, the pixel size of the camera on the sample is 0.068 μm.

For single-photon widefield imaging experiments, the short-wave pass filters were removed and the long-wavelength chromatic reflector was replaced

with a filter cube (XF22, Omega Optical, Inc.) that comprised an excitation filter with a peak wavelength of 485 ± 22 nm, a chromatic reflector with a 505 nm long-wave pass filter and an emission filter with a peak wavelength of 530 ± 30 nm. The 75 mm plano-convex tube lens was removed, and the mercury arc lamp excitation source (U-ULS100HG, Olympus) and coupling optics originally supplied with the microscope were reattached. At a wavelength of 485 nm, the maximum time-averaged power at the specimen plane exiting the 60x/0.9 N.A. water dipping lens was 240 μW. The same camera was used with the same PC and controlling software as with widefield two-photon excitation.
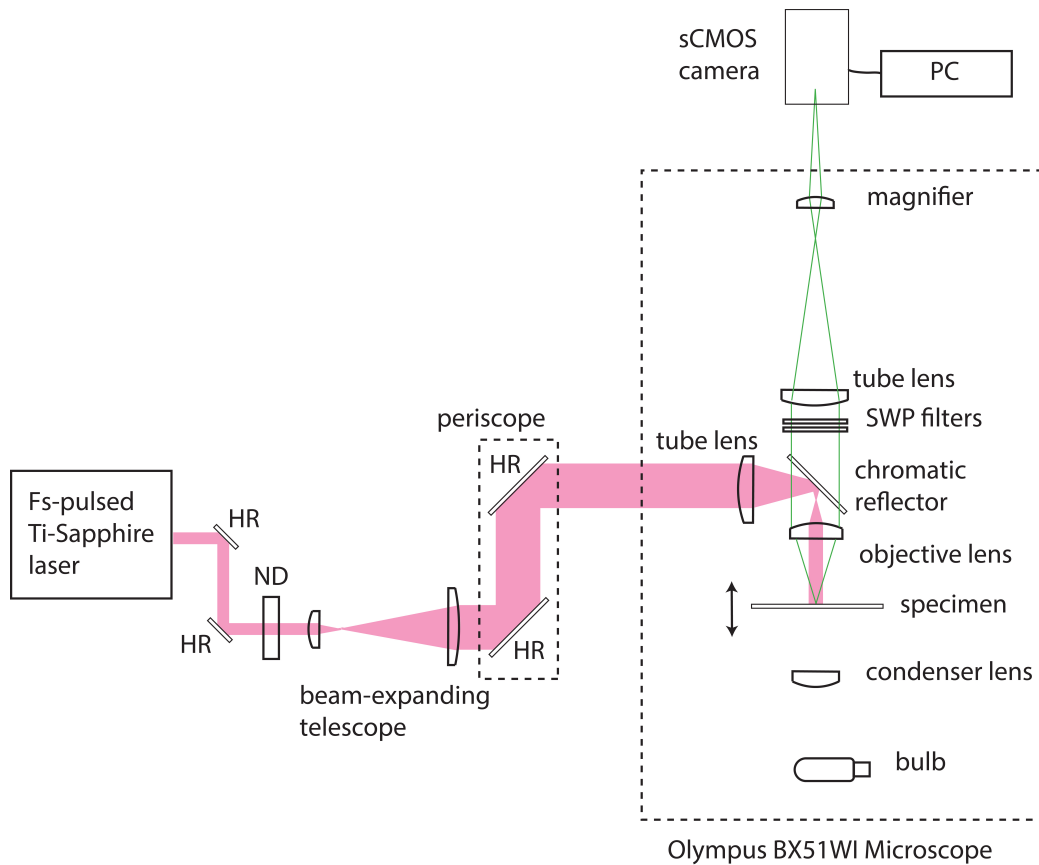
Figure 4.1: Widefield two-photon microscope and image capture system. An upright microscope was modified for two-photon excitation by changing the excitation, emission and dichroic filters. A cooled sCMOS camera was used to detect fluorescence from the specimen. A femtosecond-pulsed Ti:Sapphire laser was used as the excitation source. The weakly divergent output from the Ti:Sapphire laser was coupled into the microscope and focused to provide a beam waist close to the back aperture of the objective lens. This produced a wide and weakly-focused beam in the specimen plane which did not contribute significantly to the optical sectioning power. HR=highly reflecting mirror, ND=neutral density filter, SWP=short-wave pass filter.

4.2.2 Imaging primary rat hippocampal cultures

Widefield two-photon excitation of fluorescence was performed on primary rat hippocampal cultures to demonstrate the capability of rapid imaging. Primary rat hippocampal cultures were prepared in the laboratory of Dr Trevor Bushell at SIPBS, as described in Ref. [144]. Briefly, Sprague-Dawley rat pups 1–2 days old were killed by cervical dislocation and decapitation following Schedule 1 procedures of the UK Home Office guidelines, UK Animals (Scientific Procedures) Act of 1986, and the brain removed. The hippocampi were then dissected out, incubated in a papain solution (1.5 mg/ml, Sigma-Aldrich) at 37 °C for 20 minutes. The hippocampi were then washed in solution containing bovine serum albumin (10 mg/ml), dissociated by trituration and plated onto coverslips previously coated with poly-L-lysine (0.1 mg/ml) at a final density of 3×10^5 cells/ml. Cultures were incubated in Neurobasal-A Medium (Invitrogen) supplemented with 2 % (v/v) B-27 (Invitrogen) and 2 mM L-glutamine and maintained in a humidified atmosphere at 37 °C/5 % CO_2. After 5 days *in vitro* (DIV), cytosine-D-arabinofuranoside (10 μM) was added to inhibit glial cell proliferation. Cells were used experimentally from 11-14 DIV.

For imaging, hippocampal cultures were washed twice with a HEPES-buffered saline (HBS) containing (in mM): NaCl 140, KCl 5, $MgCl_2$ 2, HEPES 10, D-glucose 10 and $CaCl_2$ 2, pH 7.4, and transferred to HBS containing Fluo-4 AM (10 μM, 45–60 min, room temperature). Once loaded, cells were washed with HBS and images were obtained from the cell bodies of neurones with constant irradiation and with frame rates of up to 100 Hz. Pixel binning was used to increase the signal to noise ratio of the images: four pixel binning

was used at frame rates of 1–50 Hz, and eight pixel binning was used for camera frame rates of 100 Hz. Experiments were performed on cultures at room temperature. Cells were identified as the cell bodies of neurones based on their morphological characteristics. Data were calculated as changes in fluorescence ratio from the fluorescence signal intensity at time t=0 s.

The fluorescence signal intensity measured over time in the live cell neuronal preparations were also compared using both single-photon and two-photon widefield excitation to investigate photo-bleaching at different frame rates. For these measurements, time-averaged powers of $\sim$50 μW for single-photon and $\sim$100 mW for two-photon excitation at 1 Hz, $\sim$400 μW and $\sim$170 mW at 10 Hz, and $\sim$2.5 mW and 360 mW at 100 Hz were used. These were chosen to facilitate the best comparison of single-photon and two-photon excitation. Similar initial fluorescence signal intensity counts were obtained by adjusting the excitation radiation in one region of the specimen then moving to an adjacent region for recording. It is perhaps helpful to note here that this setup procedure was possible by eye, since the two-photon excitation of fluorescence could be observed using the binocular viewer of the microscope.

To determine whether the transient changes in fluorescence signal intensity over time were caused by synaptically-driven events, NBQX (20 μM, Abcam) and DL-AP5 (100 μM, Abcam), AMPA receptor and NMDA receptor antagonists respectively, were applied in order to block excitatory synaptic activity. Additionally in separate experiments, the GABA$_\text{A}$ receptor antagonist bicuculline methiodide (20 μM, Abcam), was applied to determine the consequence of reducing the intrinsic inhibitory tone present in the cultures. Data were recorded using widefield two-photon excitation (λ=780 nm,

P_{av}=180 mW and a frame rate of 10 Hz for NBQX/DL-AP5, P_{av}=250 mW and a frame rate of 50 Hz for bicuculline) before either the NBQX/DL-AP5 or bicuculline was added to the bath. The excitation source was then blocked to prevent irradiation of the specimen for 10 minutes, and then further data were recorded using the same excitation and detection parameters.

4.3   Results

High-resolution, high-contrast two-photon excited fluorescence images of Ca^{2+} transients in live neuronal cell bodies were obtained at frame rates of up to 100 Hz. Figure 4.2a shows widefield single-photon and widefield two-photon excited fluorescence images of live cells with continuous irradiation. The frame rates were 1 Hz, 10 Hz and 100 Hz. The excitation power was adjusted to give a similar subjective appearance in the first images of all the series. This strategy was adopted to achieve similar signal-to-noise values at the start of all the series. The fluorescence signal intensities for three regions of interest (ROIs) located over neuronal cell bodies in each culture dish were measured from time t=0 to 590 seconds at 5-second intervals using ImageJ [145]. An average value of fluorescence intensity from the three ROIs was obtained for each dataset, and was then normalised relative to the fluorescence signal intensity at time t=0 seconds. The resultant plots of normalised average fluorescence signal intensity with time for single-photon excitation and two-photon excitation are presented as Figs. 4.2b and 4.2c.
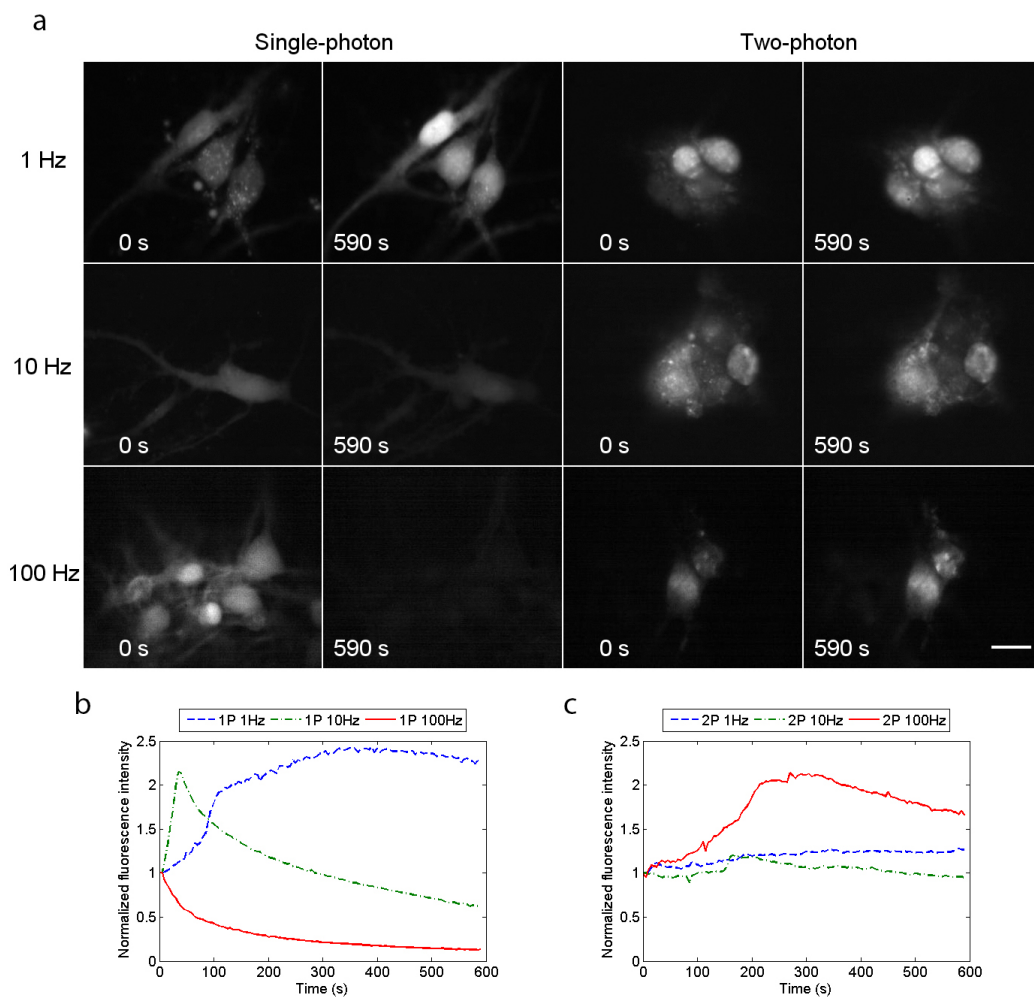
Figure 4.2: Reduced photo-bleaching using widefield two-photon excitation. (*a*) Single-photon and two-photon widefield images of live neurones, taken at frame rates of 1, 10 and 100 Hz with continuous irradiation for 590 s. The normalised fluorescence intensities are plotted vs time in (*b*) for single-photon and (*c*) for two-photon excitation. Photo-bleaching was observed when using single-photon excitation at 10 Hz and 100 Hz because of the higher light doses required to compensate for the short exposure times, whereas no photo-bleaching was observed when using two-photon excitation at similar frame rates. Scale bar=15 μm.

For both single-photon and two-photon excitation at a frame rate of 1 Hz, the overall fluorescence signal intensity increased over time but was much greater in the single-photon case, with an increase in signal in excess of 100 % compared to a 25 % increase using two-photon excitation over the same time period. However, at a frame rate of 10 Hz, there was very rapid fading using single-photon excitation (following a large Ca^{2+} spike at around 30 seconds), whereas the fading using two-photon excitation was minimal, with less than 5 % loss of fluorescence signal intensity after 590 seconds. At a frame rate of 100 Hz, however, recordings were quite different under the two illumination regimes. Using single-photon excitation, there was a rapid decrease in fluorescence signal intensity, with almost no fluorescence recorded after 590 seconds. For two-photon excitation, the fluorescence signal intensity increased slowly over the first 200 seconds and then began to decrease. So even at this fast framing rate (with increased irradiation to compensate for the shorter integration time), useful images were being obtained with widefield two-photon excitation long after the conventional single-photon recordings had faded totally. We noted also that the rate of fluorescence intensity increase under two-photon excitation at 100 Hz was less rapid than that measured for single-photon excitation at the much slower speed of 1 Hz.

The use of the calcium indicator dye Fluo-4AM and therefore the presence of Ca^{2+}-driven fluctuations in fluorescence intensity has complicated the analysis of the photo-bleaching data, but the primary purpose of this study was to consider the suitability of the fast widefield two-photon microscope for calcium imaging, because of the known difficulties with photo-bleaching in single-photon epi-fluorescence recording. Photo-bleaching by itself could be

125

better studied by using fluorescent dyes that are not calcium indicators, such as FITC and acridine orange. This would eliminate fluctuations in signal intensity owing to calcium fluctuations.

Ch4-Supplementary Video 1 shows time-lapse recordings of live neuronal cell bodies loaded with Fluo-4 AM at a frame rate of 100 Hz using single-photon (left) and two-photon (right) widefield excitation. The neuronal cultures were irradiated continuously for 590 seconds and the video shows a frame every 5 seconds, demonstrating very clearly the rapid decrease in fluorescence intensity observed using widefield single-photon excitation, while no significant reduction in fluorescence intensity was observed using widefield two-photon excitation.

The mechanisms responsible for such light-induced changes over time are at present not understood. Increased fluorescence has often been observed and it has been suggested that this results from the photo-induced release of Ca^{2+} [146, 147] or from direct photo-activation of the fluorescent dye [148, 149] or effects of sample heating on membrane permeability [150], all of which can be expected at the short wavelengths applied in single-photon microscopy. The commoner problem of photo-bleaching due to the destruction of the dye by free-radicals generated by illumination [151] is a serious limitation in all single-photon live cell imaging. Our present results suggest that widefield two-photon microscopy may overcome the bleaching problem at frame rates between 10–100 Hz.

To confirm the two-photon nature of the excitation process, images with frame rates of 1 Hz, 10 Hz, 50 Hz and 100 Hz were obtained at five time-averaged incident powers. Log-log plots of fluorescence intensity from five

126

ROIs with excitation power gave gradients of between 1.8 and 2.3 for all frame rates, confirming two-photon excitation. An example time course with three ROIs chosen in three adjacent cell bodies is shown in Fig. 4.3, and Ch4-Supplementary Video 2 shows slow ($\sim$seconds) Ca^{2+} transients at a camera frame rate of 100 Hz over a duration of 10 seconds. For display purposes, the video file has been reduced in size by 50 %. In this video, three ROIs were chosen in three adjacent cell bodies to not only demonstrate the rate of image capture but also to confirm that the measured change in fluorescence signal intensity with time was not global across the image, but is localised to individual cell bodies at different times. This evidence suggests that the change in measured fluorescence signal intensity was not a consequence of fluctuations in laser power or camera instability but arose from localised changes in intracellular Ca^{2+} concentration.
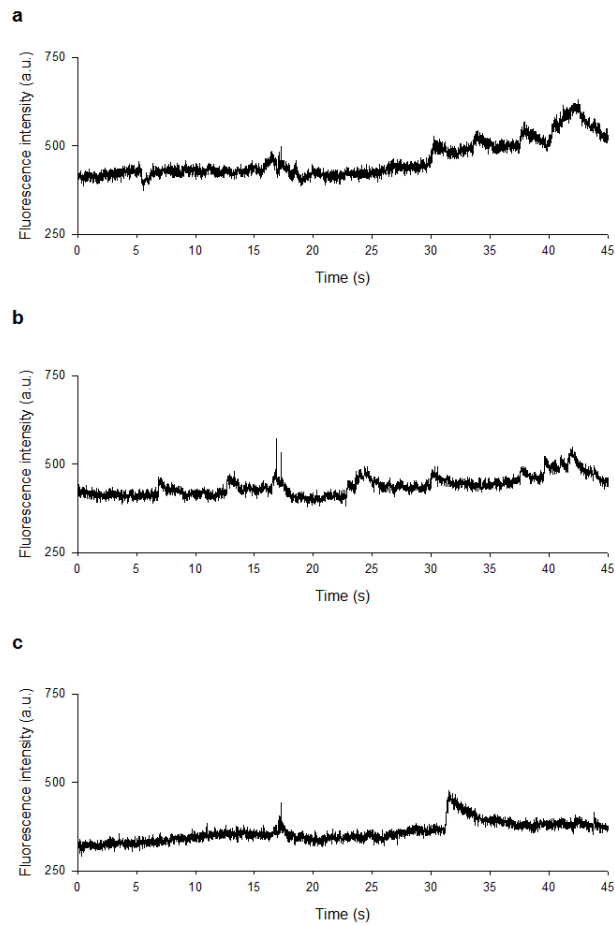
Figure 4.3: Localisation of changes in fluorescence intensity. (a), (b) and (c) show widefield two-photon excited fluorescence intensities within three adjacent live neuronal cell bodies loaded with Fluo-4 AM, acquired at a frame rate of 100 Hz over a duration of 45 seconds. This confirms that the measured change in fluorescence signal intensity with time was not global across the image, but was instead localised to individual cell bodies at different times.

Having established that widefield two-photon excitation reduces photo-bleaching at high frame rates, we then examined whether Ca^{2+} events in-

duced by synaptic activity could be observed in primary hippocampal cultures. Figure 4.4a and Ch4-Supplementary Video 3 (left panel), acquired at a frame rate of 10 Hz, shows spontaneous changes in fluorescence intensity in live neuronal cell bodies over a 60-second time period, which were abolished in the presence of the AMPA and NMDA receptor antagonists NBQX (20 μM) and DL-AP5 (100 μM) (Fig. 4.4b) and right panel of Ch4-Supplementary Video 3), indicating that these events are driven by glutamatergic excitatory synaptic activity. The sensitivity to NBQX/DL-AP5 is similar to that observed when using the whole-cell patch clamp technique to monitor synaptically driven events including spontaneous action potential firing using identical cultures (Fig. 4.4c and 4.4d) [144, 152] thus highlighting the functional capability of this method.

Additionally, separate experiments show the consequence of reducing the intrinsic inhibitory tone present in the cultures through the application of the $GABA_A$ receptor antagonist bicuculline (20 μM). Figure 4.4e and Ch4-Supplementary Video 4, acquired at a frame rate of 50 Hz, shows that spontaneous changes in fluorescence intensity initially became more frequent and erratic in nature but at later time points were not present given the large rise in fluorescence within the neuronal cell bodies due to uncontrolled glutamatergic activity. Because glutamate is the major excitatory transmitter in the brain and is present virtually everywhere in high concentrations [153], the reduction of the inhibitory tone in the glutamatergic synapses (which consist of glutamate receptors) through the addition of bicuculline has led to these synapses firing all the time, increasing the fluorescence signal within the neurones.

129
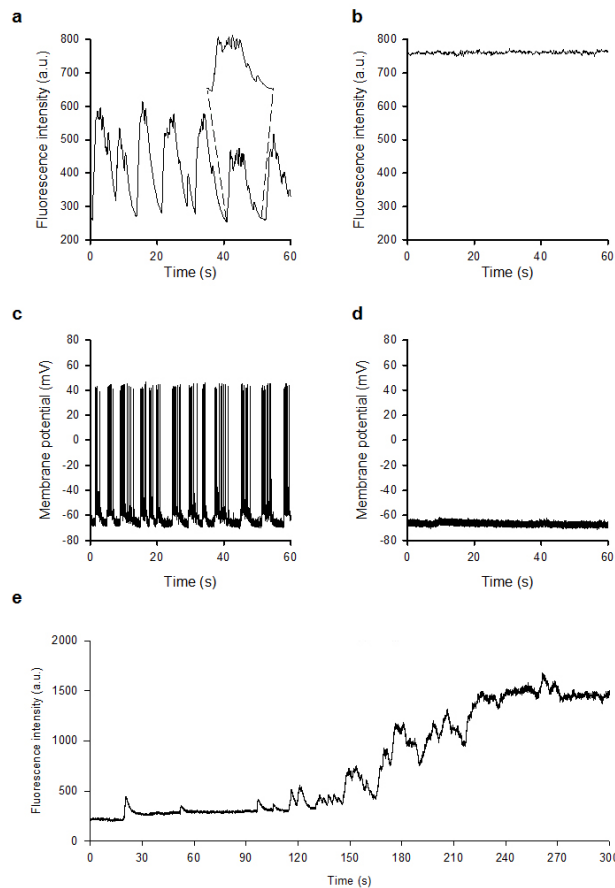
Figure 4.4: Widefield two-photon excitation for recording fast synaptic activity. (*a*) Fluorescence recording at 10 Hz shows spontaneous changes in fluorescence intensity in live neurones, abolished in the presence of DL-AP5 and NBQX (*b*). The expanded region of (*a*) shows an envelope of events indicating fast activity. (*c*) Whole-cell current clamp recordings revealing spontaneous action potential firing, abolished in the presence of DL-AP5 and NBQX (*d*). (*e*) Fluorescence recording at 50 Hz following the application of bicuculline shows spontaneous changes in fluorescence intensity initially becoming more frequent and erratic but at later time points were not present given the large rise in fluorescence due to uncontrolled glutamatergic activity.

130

Since the cell preparations used here were a thin monolayer of cells, optical sectioning was not performed. However, some optical sectioning of thicker specimens was possible. Figure 4.5 shows optical sectioning of an auto-fluorescent fixed *Taraxacum* pollen specimen mounted in Histomount, obtained at an excitation wavelength of 820 nm and using the same chromatic reflectors and emission filters shown in Fig. 4.1. Here a 60x/1.35 N.A. oil immersion objective was used, and the montage was obtained by moving the specimen by 1 μm increments axially over a range of 25 μm. The frame rate was set to 10 Hz for each image. The spikes at the top and bottom of the pollen grain are clearly independently resolved without deconvolution or other image processing methods.
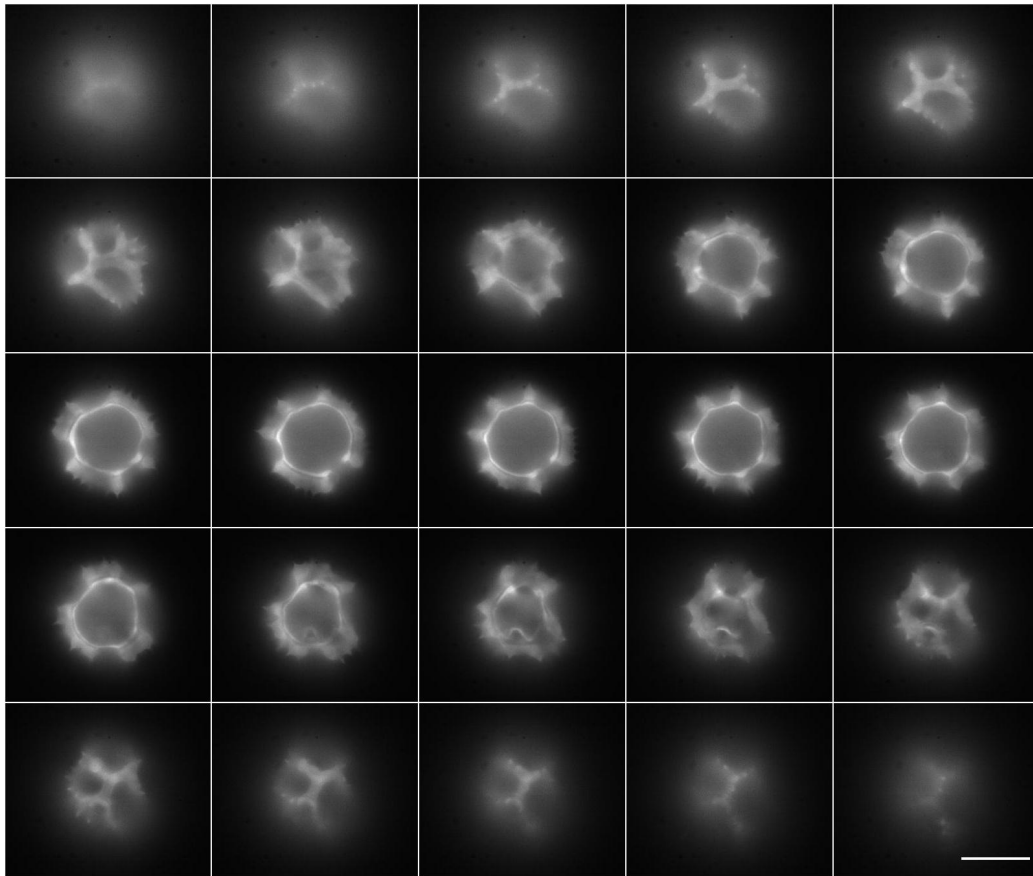
Figure 4.5: Optical sectioning of pollen specimen. (*a*) Widefield two-photon microscopy shows some optical sectioning of an auto-fluorescent fixed *Taraxacum* pollen specimen, obtained by moving the specimen by 1 μm increments axially over a range of 25 μm. No post-processing was performed on the images except for cropping to display only a single pollen grain within the image field. The optical sectioning shown here is closely similar to that obtained in a widefield single-photon fluorescence microscope. This confirms that the optical depth of field is due to the focusing of the emission only. Scale bar=15 μm.

4.4 Discussion

In evaluating this widefield two-photon microscopy method, it is natural to ask what advantages it confers in relation to conventional two-photon scanning and single-photon widefield microscopy.

The most important advantage of the method is the low photo-bleaching rate, compared with both two-photon scanning and single-photon widefield methods, when applied to the imaging of fast events. This would appear to present a great experimental advantage. The reason for this advantage is almost certainly that our widefield regime requires an excitation intensity that is about three orders of magnitude less than that used in laser scanning two-photon microscopy. Lowering the excitation intensity may bring a disproportionate benefit, since it is known that photo-bleaching has a dependency on intensity even higher than two-photon fluorescence [127, 154]. The LOTOS-based two-photon scanning of Konnerth and co-workers allows even faster imaging with reduced photo-bleaching and phototoxicity [136, 137, 138], but the LOTOS method is technically challenging and complex, requiring in-house expertise, and it comes at a high cost. Widefield two-photon microscopy is easy to implement, with no costly additions to the microscope apart from the laser, and we believe that this method could prove advantageous when using fluorophores or photoproteins with fast photo-bleaching rates, including the Ca^{2+}-sensitive dyes, CFP [155], eBFP [156] and YFP [157]. This technique may also reduce unwanted photo-bleaching in FRAP, FLAP and other similar experimental methods, where photo-bleaching of the untargeted region can compromise results [158, 159]. We have used a single camera and fluorophore here, but our method could be easily adapted for

simultaneous multi-channel recording using an image splitter and a second camera.

The advantage in time-resolution over conventional two-photon scanning is plainly shown by the results at high frame rates. The penetration ability of two-photon, as compared with single-photon excitation, which has been well established [126], has not been measured here, but is expected in this method also, because it depends on the lower scattering of longer wavelengths and the low absorption of the ultra-short pulsed infrared excitation wavelengths. The widefield two-photon method cannot be expected to perform as well as conventional scanned two-photon excitation in optical sectioning ability. By imaging fluorescent test specimens using the 60x/1.35 N.A. oil immersion lens at 820 nm, we measured an axial point spread function of around 5 μm and a measured lateral resolution of 850 nm. These resolution values are lower than for a point-scanning two-photon microscope system with similar excitation parameters, but they are an expected consequence of weak focusing of the excitation beam. Nevertheless, the results from our live cell experiments and imaging of thicker specimens suggest that this method could be adapted for in vivo imaging, with the advantage of reduced photo-bleaching. Although no temporal focusing [160] was used here, our widefield method could be used with temporal focusing to obtain improved optical sectioning, without the low image contrast and much reduced resolution observed in multi-focal two-photon microscopy [161].

Ultra-short pulsed near-infrared lasers of the type used here have been previously used to generate Ca^{2+} waves in differentiated cells. Smith *et al.* [162] used a single diffraction-limited beam focus of w_0=0.3 μm, with an

average power $P_{av} > 20$ mW, λ=775 nm, repetition frequency $\Delta\nu$=82 MHz and pulse duration τ=140 fs, which gives a peak intensity $I_{peak} > 6.16 \times 10^{15}$ W/m^2. However, since the peak intensity of illumination used in our two-photon widefield microscope is around three orders of magnitude less than Smith *et al.* used in their experiments, it is highly unlikely that we are observing light-induced Ca^{2+} transients. Indeed, the sensitivity of the observed Ca^{2+} events to blockade of glutamatergic synaptic activity indicates that the events are synaptically driven and are presumably triggered by action potentials arriving at the neuronal cell body, the consequence of which is the transient increase in intracellular Ca^{2+} level due to membrane potential depolarisation. The close similarity between the optical transients observed here and those recorded electrically in individual cells by the whole-cell path clamp technique in current clamp mode are a clear demonstration of the sensitivity, time resolution and usefulness of this method. We have concentrated here on the improved time resolution and remarkably low level of photo-bleaching, but, as already pointed out by Hwang *et al.*, there may be other advantages over single-photon imaging, such as improved discrimination against auto-fluorescence and clearer imaging of dense tissues.

4.5   Conclusion

In this chapter, I have discussed our work on a widefield two-photon microscope and its use in recording fast synaptic activity in live neurones. Two-photon excitation of fluorescence in a widefield configuration has been described previously by Hwang *et al.*, but we have extended their approach by

enlarging the field of view and, more importantly, increasing the frame rate to 100 frames per second.

By determining the overall total excitation radiation applied in both widefield and laser scanning two-photon microscopy, I have shown that the detection of two-photon-excited fluorescence (which requires the high peak intensities normally found in a laser scanning microscope) is possible in a widefield setup because of the vast increase in exposure time.

The widefield two-photon microscope is simple to build and use, and there are no costly components, unlike in often complex approaches to increasing the imaging speed in two-photon laser scanning microscopy. The image quality, phototoxicity and bleaching at frame rates of 1–100 Hz have been explored by recording synaptically-driven Ca^{2+} events in live neurones. These show that photo-bleaching is greatly reduced when using widefield two-photon excitation in comparison with single-photon excitation, particularly at high frame rates.

The general use of two-photon microscopy in biomedical imaging has been limited by photo-bleaching and the high cost of confocal laser scanning microscopes. I have shown here that widefield two-photon microscopy is a viable alternative by demonstrating its use in fast two-photon calcium imaging. This simple and low-cost approach should promote the wider use of two-photon imaging in biomedicine in general.

Chapter 5

A standing-wave fluorescence microscope

In this chapter, I will discuss our work on standing-wave excitation of fluorescence in a laser scanning microscope through the simple modification of placing a reflector beyond the specimen. I will demonstrate its usefulness in acquiring multiple super-resolved sections, with an axial resolution of ~ 90 nm. Fluorescence fringes from model specimens and red blood cells serve as precise contour maps, revealing three-dimensional structural information.

5.1 Introduction

A standing wave is so called because it appears to be stationary: that is, its nodes (points of no displacement) and antinodes (points of maximum displacement) are constant in position. In a nonmoving medium, a standing wave is the result of interference between two waves traveling in opposite

directions. When a standing light wave is formed by reflection from a mirror as in Fig. 5.1, interference between the incoming wave (blue) and its reflection (green) gives rise to the standing wave (red). The mirror surface, located at x=0, is a node, where no radiation can be detected [59, 163, 93]. There are more nodes at intervals of half a wavelength and between the nodes, there are antinodes of high radiation intensity. The first antinode is a quarter of a wavelength away from the mirror and succeeding antinodes are at half-wavelength intervals. In fluorescence microscopy, standing-wave excitation is a simple way to increase the axial resolution of the microscope.
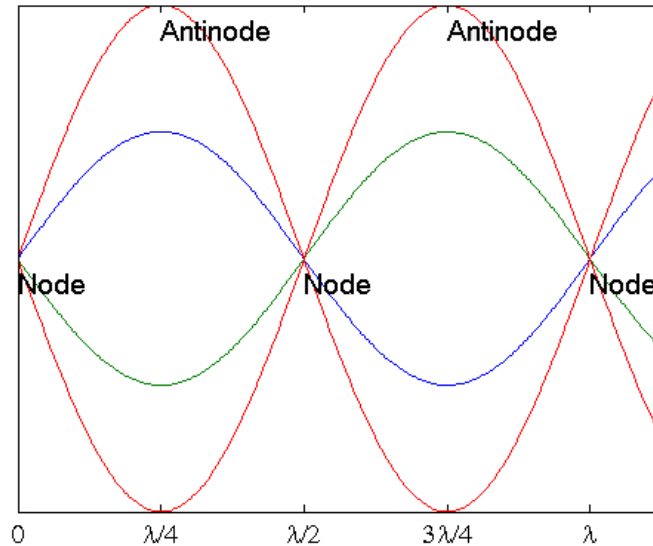
Figure 5.1: Standing-wave formation by reflection from a mirror. The incoming wave (blue) interferes with its reflection (green) and gives rise to a standing wave (red). The mirror surface at x=0 is a node, where there is zero displacement. There are more nodes at intervals of half a wavelength. Between the nodes, there are antinodes of high intensity. The first antinode is a quarter of a wavelength away from the mirror and succeeding antinodes are at half-wavelength intervals.

Standing light waves were first detected by Otto Wiener in 1890 by using silver halide crystals in photographic film as microscopic detectors [59, 60, 61]. The detection of standing light waves is not trivial because the nodes and antinodes are bunched very close together, separated by only about a hundred nanometres or so. Wiener used a very thin optically transparent layer of film, about 20 nm thick, deposited on a glass plate which he arranged to lie at a

139

very small angle of about 10^{-3} radians to a front-silvered mirror. He directed a parallel beam of quasi-monochromatic light normally upon the face of the mirror and the light passed through the film, was reflected at the mirror surface, and formed a standing wave. Upon developing the photographic emulsion, he found that it was blackened along a series of lines where the film cut the successive antinodal planes of the standing wave, separated by lines of no blackening where it crossed the nodes: for example, in the region of the film in contact with the mirror. In this way, Wiener was able to show that in photography, the chemical action of the light wave is joined to the vibrations of the electric field (and not the magnetic field) since the surface of a metal reflector was a nodal point of the electric field, as had been determined two years earlier by Heinrich Hertz in his experiments with radio waves [163, 93]. In addition, the angle of 10^{-3} radians that the film made with the mirror meant that the distance between successive blackened lines in the emulsion was 1000 times the antinodal spacing of $\lambda/2$. This made it possible for Wiener to estimate that the wavelength of green light was 550 nm and show that red light had nearly double the wavelength of blue light [60].

Standing light waves were then detected in real-time by Paul Drude and Walther Nernst in 1892 by repeating Wiener's experiment using a fluorescent layer as the detector instead of photographic film [164]. In a related experiment, they coated half the area of a glass plate with silver, deposited a very thin fluorescent layer on top, and directed a parallel beam of light perpendicular to the plate. They found no fluorescence in the area coated with silver and strong fluorescence in the area that was uncoated. In this way, they

140

showed that the surface of the silver reflector is a node of the standing wave and that, in the same way that it is so in photography, the chemical action of the light wave in fluorescence is joined to the vibrations of the electric field.

A century later, Stefan Hell and Ernst Stelzer performed standing-wave excitation of fluorescence in a microscope using the 4Pi geometry, where counter-propagating coherent waves are directed into the specimen [165, 166], while Frederick Lanni and his co-workers used quasi-parallel widefield illumination by placing a mirror beyond the specimen to reflect the laser beam coming out of the microscope objective, an approach much simpler to implement [64]. By their method, Lanni and his co-workers made two quasi-collimated Gaussian laser beams interfere and created a standing wave with nodal surfaces that could be considered planes parallel to the mirror. They used this standing-wave pattern of illumination to excite fluorescent specimens of actin stress fibres in a fixed 3T3 fibroblast and improved the axial resolution to the intensity peaks at the antinodes, with a full width at half maximum (FWHM) of $\lambda/4n$, where λ is the excitation wavelength and n is the medium refractive index. It is worth noting here that the FWHM gives the positional uncertainty of a fluorophore in the antinodal plane. The next antinodal plane is $\lambda/4n$ away, and in this distance between two successive planes there is missing information. If one were to separate two fluorophores in the axial direction, the best separation achievable would then be $\lambda/2n$, because if the two fluorophores were separated by $\lambda/4n$, one of them would be in the dark space between antinodal planes of excitation and would not be observed [167]. Therefore if the axial resolution was defined as the ability to separate two objects in z, it would be $\lambda/2n$ and $\lambda/4n$ would be the slice

141

thickness. In this work we will define the axial resolution as the positional uncertainty indicated by the antinode FWHM $\lambda/4n$.

Recently, Elsayad *et al.* used the reflection method in laser-scanning, growing fluorescently labeled cells on a dielectric layer of appropriate thickness deposited on a reflector and using a narrow detection bandwidth ($<$ 10 nm) to obtain an axial distance-dependent spectral signature [168]. By using optimal coatings, they obtained an image of the fluorophore closest to the substrate (< 100 nm) then computed for the mean axial distance of the fluorophore assuming normal axial distributions, building up an image by assigning false colour to axial distance. But they listed the following drawbacks to their method: it is computationally demanding, sensitive to accurate coating fabrication and characterisation, limited in the number of fluorophore species that can be simultaneously studied, and growing samples (which have to be somewhat transparent) on special coverslips is inconvenient and limits the application [168].

In this work, what we set out to do was to utilise not only the first antinode of the standing wave (which is essentially what Elsayad *et al.* did), but several antinodes all at the same time, each one contributing to the fluorescence image and therefore eliminating the need for any computation. We chose to do this work in a laser scanning microscope because the presence of apparently planar antinodes in laser scanning, even though the beam is focussed to a spot and therefore should produce antinodes that are curved, has not really been explained and was an exciting prospect for microscopy in our view. For the reflector, we intended to use an ordinary aluminised first-surface mirror (BB1-E02, Thorlabs, Ltd., UK) which has excellent and

142

predictable reflectance characteristics and is also readily available.

But the drawback in using multiple antinodes in standing-wave excitation is that if the thickness of the specimen is greater than the antinodal spacing $\lambda/2n$, several planes may be excited simultaneously, making their contributions difficult to separate from each other [169, 170]. However, if the specimen has differentiated structure axially and the variation in height is not too abrupt across the field of view, individual fringes can be produced in lateral images and used as contours for mapping three-dimensional objects.

5.2 Standing-wave excitation in a laser-scanning microscope

5.2.1 Model specimens

An ideal specimen for showing multiple planes of emission is a monolayer of dye attached to a planoconvex surface. I sent 63 mm and 250 mm focal length planoconvex silica lenses (63 PS 16 and 250 PS 25, Comar Instruments, UK) to Sumeet Mahajan at the University of Southampton, who coated them with a monolayer of Atto 532 dye. Mahajan used Atto 532 because I wanted to use 514 nm to excite the dye. Mahajan's method involved rinsing the lenses thoroughly with dry acetone and dipping them in a 2 % mass concentration solution of 3-amino-propyltrimethoxysilane (APTMS, Sigma-Aldrich, USA) in dry acetone. The optimum time for coating the silica surface with APTMS was found to be 6 hours. After this time the lenses were taken out, rinsed with dry acetone a few times and gently blow-dried with nitrogen. A 10 μM

solution of Atto 532 NHS ester (88793, Sigma-Aldrich, USA) was prepared in pH 8.1, 0.01 M phosphate buffer. The lenses were soaked in this solution in a vial, sealed with parafilm and left overnight in a dark chamber wrapped in aluminium foil. Thereafter, the remaining solution was recovered and the silica surfaces thoroughly rinsed with deionised water. The lenses were then blow-dried with nitrogen and protected from light.
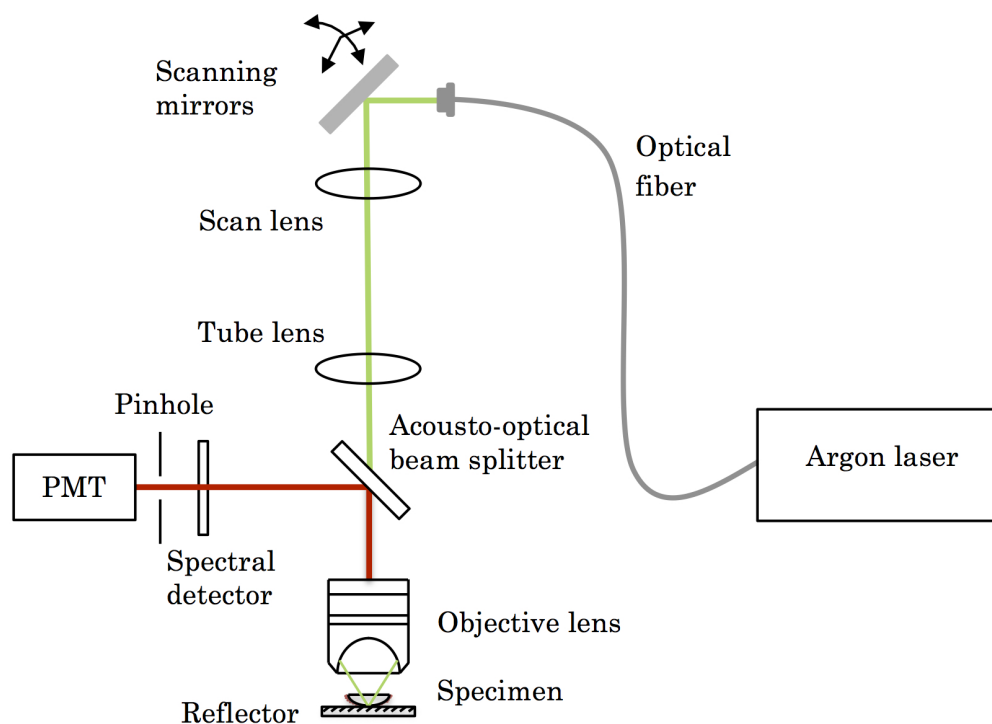
Figure 5.2: Schematic diagram for standing-wave excitation of fluorescence in a laser-scanning microscope. The specimen is placed on top of a mirror, which reflects the beam coming out of the microscope objective, creating a standing-wave pattern of illumination that simultaneously excites fluorescence at multiple planes.

I performed single-spot laser-scanning on the planoconvex specimen using a Leica SP5 DM600 confocal microscope, as shown in Fig. 5.2. For fluorescence excitation of the monolayer of Atto 532 dye which had an excitation maximum at 532 nm, I used the 514 nm line of an Argon laser, with an

average power of about 5 μW at the specimen using a 5x/0.15 N.A. dry objective. The specimen was placed on top of a mirror, as in Fig. 5.3a, and the mirror reflected the beam coming out of the microscope objective, creating a standing-wave pattern of excitation. I obtained concentric fluorescence fringes as shown in Fig. 5.3c, with the fringe spacing as one would expect if the fluorescent monolayer cut through the multiple antinodes of a standing wave. The centre of the fringes is the point of contact between the specimen and the mirror, and it is dark as expected because the mirror surface is a node of the standing wave. This result is the equivalent of Wiener's experiment in a laser scanning microscope [59].

We sought to extend this experiment to include objectives of high numerical aperture, such as are needed in cell biology imaging, with the aim of using a standing wave method to visualise cell specimens. These have a limited working distance of a fraction of a millimetre. I coated a glass coverslip with a thin layer of fluorescein dye by dissolving fluorescein in ethanol at a concentration of 10 μM and placing a 5 μL drop of the solution on the coverslip, allowing the liquid to evaporate and produce a thin coating of fluorescein on the glass. I placed the coverslip on top of a planoconvex silicon lens (#69-673, Edmund Optics, Inc., USA) which served as a mirror, as in Fig. 5.3b. We would expect the dye-coated coverslip placed on top of a planoconvex mirror to give a similar pattern of concentric fluorescence fringes as the planoconvex specimen placed on top of a flat mirror. I performed laser-scanning in this setup using a 40x/1.30 N.A. oil immersion objective and 488 nm line of the Argon laser, with an average power of 20 μW at the specimen, and again observed a pattern of concentric fluorescence

146

fringes, shown in Fig. 5.3d, consistent with standing-wave excitation, in spite of the presence of rays at a wide range of angles of incidence.

explain that the curved mirror and coverslip is analogous to the mirror and coated lens in terms of the fluorescence pattern you expect to get.
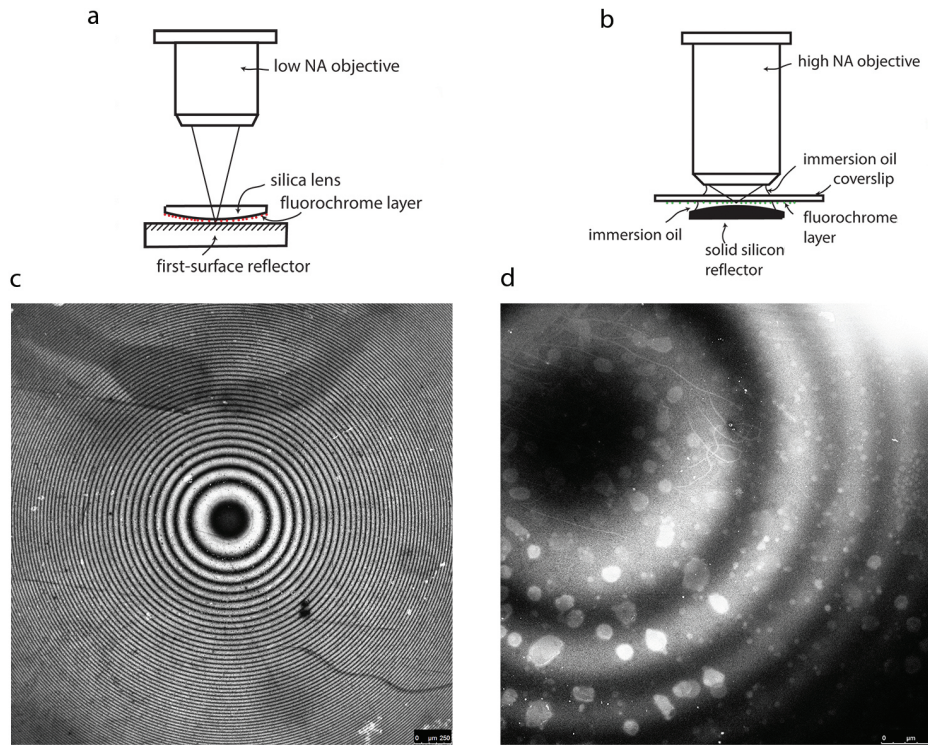
Figure 5.3: Standing-wave-excited multiplanar fluorescence in a laser-scanning microscope. (*a*) A planoconvex silica lens coated with a monolayer of Atto 532 dye is placed on top of a mirror and scanned using a 5x/0.15 N.A. dry objective. (*b*) In order to use objectives of high numerical aperture and limited working distance, a glass coverslip with the underside coated with a thin layer of fluorescein is placed on top of a planoconvex silicon lens acting as a mirror and scanned using a 40x/1.30 N.A. oil immersion objective. (*c*) Fluorescence image from the setup in (*a*), showing concentric fringes from multiple planes of excitation at the standing-wave antinodes. Scale bar=250 μm. (*d*) Fluorescence fringes from the setup in (*b*), consistent with standing-wave excitation in spite of the presence of rays at a wide range of angles of incidence. Scale bar=50 μm.

148

I verified that the axial spacing of the fringes is constant and comparable to the antinode spacing $\lambda/2n$ by plotting the fringe intensity as a function of height from the mirror surface. Figure 5.4a shows a median section of the half-spherical surface of the specimen in Fig. 5.3a, of radius R and centred at O, in contact with the mirror. A bright fringe of radius r_1 is at a height L_1 above the mirror, and the next fringe, of radius r_2, is at a height L_2. I obtained the height separating the two fringes from the two triangles formed separately by r_1 and r_2, the lengths of which are given by the Pythagorean theorem: $R^2 = r_1^2 + (R - L_1)^2$ and $R^2 = r_2^2 + (R - L_2)^2$. The separation height is $L_1 - L_2 = \sqrt{R^2 - r_2^2} - \sqrt{R^2 - r_1^2}$. From the intensity profile along a radial line in Fig. 5.3c, we plotted the fluorescence intensity as a function of radial distance, shown in Fig. 5.4b, which shows the fringe spacing getting smaller with distance from the centre, as expected of a fluorescent shell of spherical shape excited by the evenly-spaced antinodes of a standing wave. Using the result $L_1 - L_2$ for the separation height between two successive fringes, I translated the radial plot in Fig. 5.4b into one of fluorescence intensity versus height from the mirror surface, as in Fig. 5.4c, which this time shows evenly-spaced peaks of fluorescence emission corresponding to where the dye is excited by the standing-wave antinodes. The plot shows 37 peaks, and by locating the positions of the maxima by vertically flipping the plot and using *fminbnd* in MATLAB, which finds the minimum of a function within an interval, I measured an antinodal spacing of 255 nm. The actual antinodal spacing $\lambda/2n$ is 257 nm, using $n = 1$ for air between the specimen and the mirror and $\lambda = 514$ nm for the excitation wavelength. The experimental result is therefore within 0.78 % of the actual value. The measured antinodal

149

spacing in Fig. 5.4c and the actual lateral separation of the fringes in Fig. 5.4b then allows an accurate reconstruction of the planoconvex specimen in three dimensions, as shown in Fig. 5.4d.

I tested whether the fluorescence fringes were caused by standing-wave excitation formed by the interaction of the excitation light with the mirror and not by a Fabry-Perot cavity effect, where the silica-air interface on one side and the mirror on the other formed the cavity. For this test, I put immersion oil ($n = 1.52$) [171], pure glycerol ($n = 1.47$) [172] and a solution of 91 % glycerol in water ($n = 1.46$) [172] between the specimen and the mirror. Putting a film of fluid that has the same refractive index as the planoconvex silica lens ($n = 1.46$) [173] eliminates reflection from the convex surface. I still observed the concentric fluorescence fringes in all cases, shown in Fig. 5.5, proving that the fringe pattern is caused by a standing wave only.
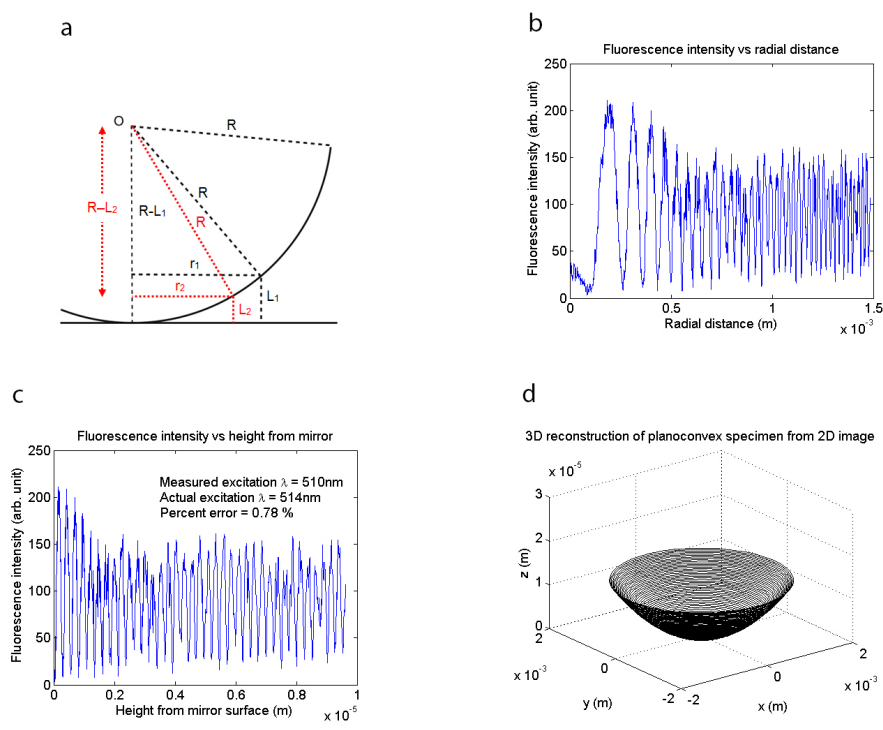
Figure 5.4: Three-dimensional reconstruction from a two-dimensional image. (a) Diagram of planoconvex specimen in contact with the mirror as shown in Fig. 5.3a. (b) Fluorescence intensity in Fig. 5.3c plotted versus radial distance, showing the fringe spacing getting smaller with distance from the centre, consistent with a fluorescent shell of spherical shape excited by the evenly-spaced antinodes of a standing wave. (c) Fluorescence intensity plotted versus height from the mirror surface, obtained using the geometry in (a), showing evenly-spaced peaks where the dye cut the antinodes of the standing wave. The measured antinodal spacing is 255 nm, accurate to within 0.78 % of the actual value of $\lambda/2n$=257 nm using an excitation wavelength of 514 nm and a refractive index of n=1 (air). (d) Three-dimensional reconstruction of the planoconvex specimen from the two-dimensional fluorescence image in Fig. 5.3c.

151
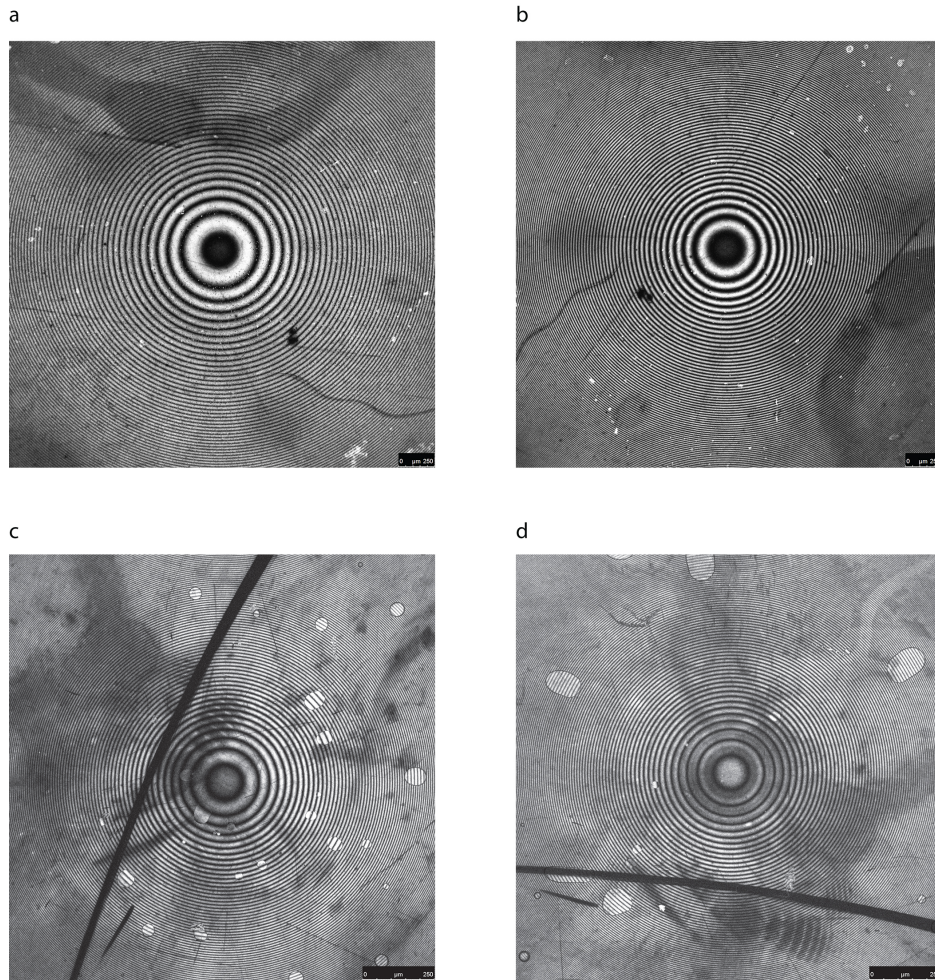
Figure 5.5: Testing whether the fringes are caused by a standing wave or by a Fabry-Perot cavity effect. Concentric fluorescence fringes in specimens with (*a*) air (n=1), (*b*) immersion oil (n=1.52), (*c*) pure glycerol (n=1.47), and (*d*) a solution of 91 % glycerol in water (n=1.46) between the planoconvex silica lens and the mirror. Putting a film of fluid that has the same refractive as the silica lens (n=1.46) eliminates reflection from the convex surface. The observation of fluorescence fringes in all cases proves that the fringe pattern is caused by a standing wave only. Scale bar=250 μm.

At this point I will discuss the origin of apparently planar antinodes in a point-scanning microscope even with objectives of high numerical aperture, where the focussed spot produces curved antinodes. As stated above, when a standing wave is formed by reflection from a mirror as in Fig. 5.6a, the mirror surface is a node. There are more nodes at intervals of half a wavelength and between the nodes, there are antinodes of high radiation intensity. The first antinode is a quarter of a wavelength away from the mirror and succeeding antinodes are at half-wavelength intervals. Spherical waves converging on a mirror surface AB will interfere with the reflected diverging spherical waves, creating nodes and antinodes as shown in Fig. 5.6b. The figure has taken into account the evolution of the wavefront radius of curvature with distance from the beam waist, hence the first antinode has a noticeably different radius of curvature. The fundamental Gaussian amplitude field, which is a solution to the beam wave equation [141], shows that as the beam comes into a focus at the mirror surface, the phase fronts are spherical with contracting radius of curvature. However, the radius of curvature reaches a minimum just before the focus then diverges so that the wavefront at the beam waist is planar. For an oil-immersion objective with a numerical aperture of 1.30 and using $\lambda = 488$ nm and $n = 1.52$, such as that which was used in Fig. 5.3b, this minimum occurs 210 nm away from the mirror surface. Therefore, beyond 210 nm, where all the antinodes except the first are located, the antinodes are curved.
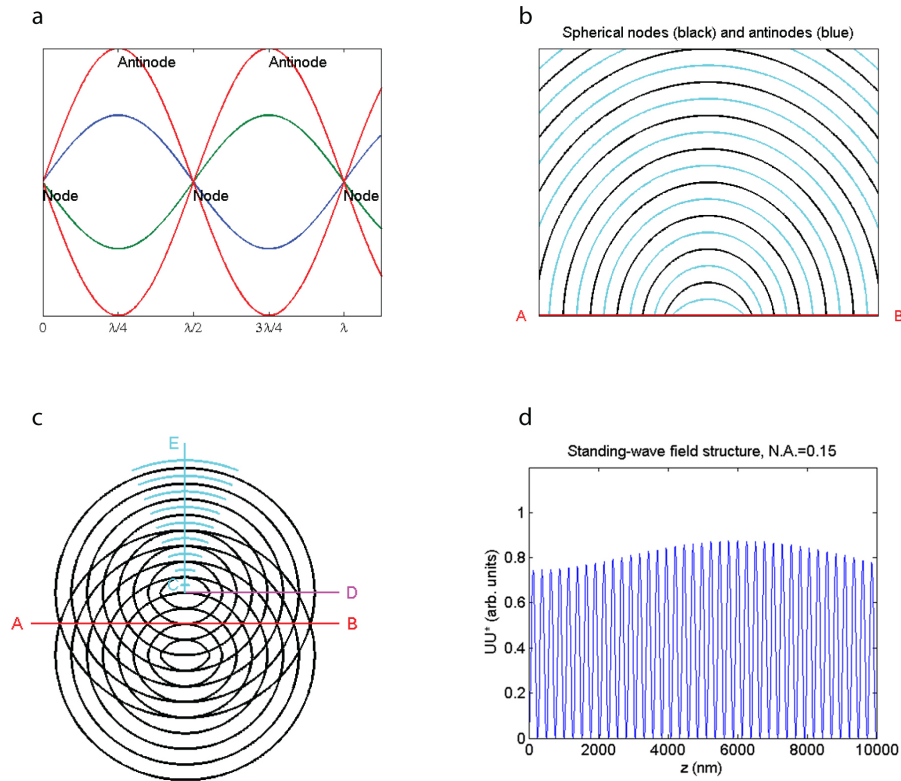
Figure 5.6: Detection of planar standing-wave antinodes in a point-scanning microscope. (*a*) Standing-wave formation by reflection from a mirror, showing nodes and antinodes. (*b*) Spherical waves converging on a mirror surface AB interfere with their reflection, creating spherical nodes (black) and antinodes (blue). (*c*) The mirror AB located one wavelength away from the focus creates a virtual image of the focus two wavelengths away. Along the line CE and at small angles to CE, there is a standing wave train with curved antinodes (blue sector) but these appear planar because the small emission in the disks is assigned to the central pixel as scanning takes place. (*d*) Standing-wave field structure for a 5x/0.15 N.A. objective, showing fringes of very high order can be detected using a low-N.A. objective with no appreciable change in fringe contrast.

154

Along all radii stretching out from the point of focus, the wave train is a perfect standing wave, but each node and antinode is a spherical shell. If a point-scanning microscope were used and a sub-wavelength fluorescent object were moved along the vertical axis away from the focus and towards the lens, we would expect to see strong maxima when it passed through the first few antinodes. Off-axis fluorescent objects would also be excited by the spherical antinodes but these would not be detected efficiently.

Figure 5.6c shows the effect of the mirror AB being located one wavelength away from the focus. This creates a virtual image of the focus two wavelengths or four node intervals away from the focus. Along the line CE, there is a standing-wave train, like one of the radii in Fig. 5.6b, but this is true only along CE and for directions at small angles to CE: that is, in the narrow sector where the antinodes are shown in blue. To take an extreme case, along CD, the phase front spacing is changing for the wave train originating in the mirror but is constant for the incoming wave train, supposing that the numerical aperture of the lens was sufficient to send in waves at such a high angle to the axis, and so the superposition of the incoming beam and its reflection produces no standing wave and there are no minima constant in position. This is true for most of the directions between CD and the blue sector. Since the illumination would have no minima in the wave trains at high angles, it would not discriminate depth. This explains why objectives of high numerical aperture fail to pick up high-order fringes, where the scanning spot is being reflected from a distant mirror such as in this case: the minima would be lost and a high background brightness would occur beyond the first few fringes, as is indeed observed. For the high-N.A. fringe pattern

155

in Fig. 5.3d, the contrast deteriorates rapidly from 93 % for the first fringe to 14 % for the fourth fringe. On the other hand, an objective of low numerical aperture could generate and detect only the wave trains in the blue sector and would ultimately approximate to a parallel-beam interferometer, capable of detecting fringes of very high order, as we have observed in Fig. 5.3c. Using the fundamental Gaussian amplitude field $U(r, z)$ [141], and taking $U_1 = U(r, z)$ for the incoming beam, $U_2 = -U(r, -(z - 2\Delta z))$ for the reflection from a mirror defocused by Δz, $U_S = U_1 + U_2$ is the superposition of the incoming and reflected beams and $U_S U_S^*$ gives the standing-wave field structure. For the 5x/0.15 N.A. objective used to obtain Fig. 5.3c, the plot of $U_S U_S^*$ versus z, shown in Fig. 5.6d, shows that indeed, fringes of very high order are detected with no appreciable change in fringe contrast, in agreement with the axial plot of fluorescence intensity in Fig. 5.4c. Therefore, the nodes and antinodes in a point-scanning microscope are spherical when the mirror is close to the focus but are reduced to progressively smaller disks centred on the axis as the mirror moves away from the focus, and the spherical shells appear planar because the relatively small emission in the disks is assigned to the pixel at the centre as scanning takes place.

In addition to fluorescence fringes detected at a wide spectral bandwidth of 100 nm, we also observed that the fringes were radially modulated in a precise way particularly when the detection bandwidth was reduced to 5 nm, which is the spectral resolution of the Leica SP5 microscope's SP® spectral detector [174]. In our experiments, the modulation has a frequency proportional to the Stokes shift, consistent with a moiré pattern between the excitation and emission, which occurs at the difference frequency between

the periodicity of the excitation standing-wave field and the periodicity of the standing-wave field created by the light at the selected emission wavelength. A moiré pattern arising from the presence of two distinct patterns has a spatial frequency that is the difference frequency between the two individual patterns [175, 176, 177]. Figure 5.7 shows the moiré pattern in the directly-observed fringes and clearly demonstrates the increasing frequency as the fluorescence is detected from 550 nm (Fig. 5.7a) through to 580 nm (Fig. 5.7d). Taking Fig. 5.7d as an example, a moiré pattern from 514 nm excitation and 580 nm emission has a theoretical spatial period of $L = 4520$ nm from $1/L = $ 1/514 nm $-$ 1/580 nm. Fig. 5.7h plots the fluorescence intensity in Fig. 5.7d as a function of height from the mirror surface, using the method described for Fig. 5.4. Using the spacing between peaks in the moiré pattern, equal to $L/2n$, we measured a spatial period of 4690 nm, accurate to within 3.8 % of the theoretical value.
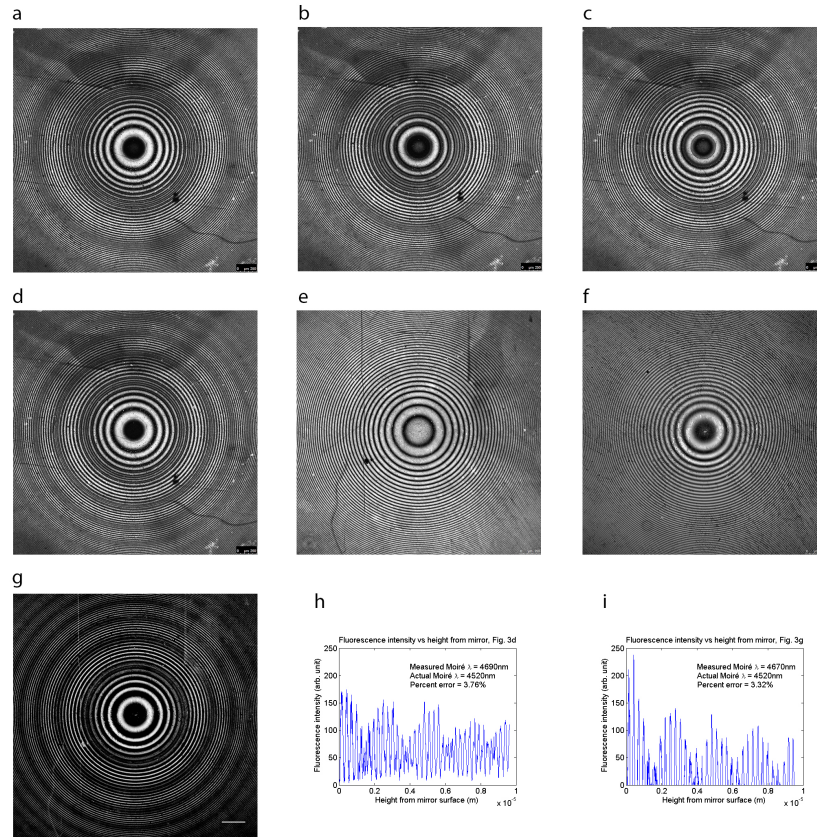
Figure 5.7: Moiré pattern from 5-nm-band detection. Fluorescence emission centred at (*a*) 550 nm, (*b*) 560 nm, (*c*) 570 nm and (*d*) 580 nm show the fringe pattern to be radially modulated with a frequency consistent with a moiré pattern between the excitation and emission standing-wave fields. (*e*) In the absence of the excitation standing-wave field, the modulation is absent in the 580 nm emission. (*f*) Excitation standing-wave field fringe pattern. (*g*) Subtraction of the emission-only fringe pattern (*e*) from the excitation fringe pattern (*f*) gives a modulated image identical to the moiré pattern in (*d*). The measured spatial periods in (*d*) and (*g*) are: (*h*) 4690 nm, and (*i*) 4670 nm, respectively. Scale bar=250 μm.

Previous work has shown that when fluorescent molecules are placed close to a mirror, the emitting molecule acts as an oscillating dipole (an antenna) and that the reflected and unreflected parts of the emitted fluorescence wave interfere with each other, producing fringes from wide-angle interference [178] and oscillations in the fluorescence decay time [179, 180, 181, 182], with analytic expressions for the radiation patterns derived from electrodynamic theory [183, 184, 185] and modified further from the fixed-dipole amplitude assumption to model the fluorophore as a dipole of constant power and variable amplitude [186]. Subsequent work in this area studied the modulation of fluorescence intensity with distance from the mirror, and explained the modulation as a consequence of the interference effects of the excitation and of the emission being both present [187]. We have obtained the fluorescence fringes from the standing-wave field created by the self-interference of the emission alone, by replacing the mirror with a laser-line notch filter (LL01-514-25, Semrock, Inc., USA) to transmit the excitation and therefore suppress the excitation standing-wave field. As shown in Fig. 5.7e, the modulation in the fringes detected at 580 nm is absent in this case. More importantly, as can be seen in Fig. 5.7g, subtraction of the 580 nm emission fringe pattern in Fig. 5.7e from the fringe pattern of the excitation in Fig. 5.7f gives a modulated fringe pattern identical to the moiré pattern in Fig. 5.7d. The spatial period of this modulation, as measured using the peak spacing in Fig. 5.7i, is 4670 nm, which is within 3.3 % of the theoretical value, confirming that it occurs at the difference frequency between the excitation and emission. The observation of a moiré pattern of the type we describe here appears to be novel in optical fluorescence microscopy.

159

5.2.2 Red blood cells

The work done by Elsayad *et al.* showed that the first antinode can be positioned near the contact between living cells and their substrate, by growing cells on a dielectric layer of appropriate optical thickness deposited on a reflector [168]. Since we wished to observe multiple antinodes, we selected as specimen mouse red blood cells whose characteristic shape, shown in Fig. 5.8, is a biconcave disk about 7-8 μm in diameter and about 1 μm thick at the thinnest point at the centre and 2.5 μm at the thickest point in the periphery [188]. To visualise fluorescence excitation at multiple antinodes, I stained the membrane of the red cells with the membrane-specific dyes DiI [189, 190, 191, 192] and DiO [191, 192]. DiI and DiO were chosen because their use as specific plasma membrane stains is well established and they can be excited by commonly available laser lines and they fluoresce brightly.

The red blood cell membrane is important because its biconcave shape and deformability facilitates large reversible elastic deformation of the red blood cell as it repeatedly passes through small capillaries during circulation, necessary to transport oxygen and carbon dioxide [193]. Disorders affecting the red blood cell surface area or membrane properties can disrupt or obstruct circulation, leading to restriction of blood flow to tissues, necrosis and organ damage [193, 194, 195].

(a)   (b)
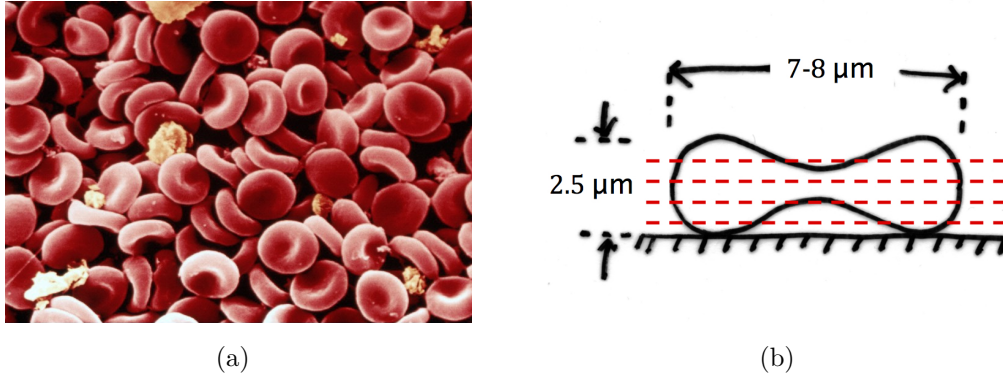
Figure 5.8: *(a)* Scanning electron microscope image of red blood cells, computer-coloured red. This image was obtained from Wellcome Images, contributed by the Electron Microscopy Unit of University College London Medical School, and is freely available for personal, academic teaching or study use. *(b)* Diagram of a red blood cell viewed from the side, showing the biconcave shape of the membrane, about 7-8 μm in diameter and 2.5 μm thick at the periphery. In the presence of multiple antinodal planes of excitation (red dashed lines), fluorescence from the membrane will generate contour lines.

For this experiment, we obtained fresh blood by cardiac puncture from healthy mice, yielding about 0.5 mL blood from one mouse. The blood was immediately mixed with the anti-coagulant acid citrate dextrose (ACD) to prevent clotting, at a ratio of 1 part ACD to 3 parts blood. 100 mL of ACD is 1.32 g trisodium citrate (BP327-500, Fisher Scientific, USA), 0.48 g citric acid (423565000, Acros Organics, USA), 1.40 g dextrose (BP350-500, Fisher Scientific, USA) and distilled water to make up 100 mL of solution. The

red blood cells were washed three times in phosphate-buffered saline solution (PBS: 137 mM NaCl, 2.7 mM KCl, 10.6 mM Na_2HPO_4, 8.5 mM KH_2PO_4, pH 7.4) and suspended to their original hematocrit (the ratio of the volume of red blood cells to the total volume of blood) in modified balanced salt solution (MBSS: 134 mM NaCl, 6.2 mM KCl, 1.6 mM $CaCl_2$, 1.2 mM $MgCl_2$, 18.0 mM HEPES, 13.6 mM glucose, pH 7.4, 37 °C). 200 μL of this suspension was set aside, resuspended in 4 % bovine serum albumin (BSA) (A7906, Sigma-Aldrich, USA) in PBS, and stored at 4 °C overnight for the preparation of intact red blood cell specimens.

In order to exclude the possibility of lensing or focussing effects from refractile material inside the cell, we also prepared red blood cell ghost specimens in addition to intact red blood cell specimens. Red blood cell ghosts have the same shape as normal red blood cells but with the haemoglobin removed from the interior. We used the protocol of Harris *et al.* [196] for the preparation of the ghosts. Washed red blood cells were suspended in 10 mL of PBS diluted 2/5 in distilled water with 1 mM $CaCl_2$. The lower osmotic pressure causes the cells to rupture and release their haemoglobin, creating ghosts. After 30 minutes at 0 °C, 5-fold concentrated PBS containing 1 mM $CaCl_2$ was added to the ghost preparation to restore isotonicity. The suspension was then incubated for 45 minutes at 37 °C to reseal the membrane, and sealed ghosts were collected by centrifugation at 2,500×g for 10 minutes. The ghosts were washed in PBS until the supernatant appeared free from haemoglobin and resuspended in 1 ml of 4 % BSA in PBS and stored at 4 °C overnight.

The ghosts and intact red blood cells were stained for the membrane by

adding a 1 mg/ml stock solution of DiI or DiO (D-282 and D-275, Invitrogen, Ltd., UK) in ethanol at a ratio of 1 part stock solution to 99 parts cell suspension, and the suspension was incubated for 30 minutes at 37 °C. The ghosts and cells were then spun down and rinsed with PBS and resuspended in 4 % BSA in PBS. To promote the adhesion of ghosts and cells to the surface of a mirror or microscope slide, these surfaces were coated with poly-L-lysine. A working solution of poly-L-lysine was made by preparing a 1 in 10 dilution of 0.1 % mass concentration poly-L-lysine stock solution (P8920, Sigma-Aldrich, USA) in water. The mirrors and microscope slides were sterilised in 95 % ethanol and dried before coating. These were submerged in poly-L-lysine in a sterile Petri dish, incubated for 15 minutes at 37 °C, washed three times with PBS, and placed under ultraviolet light in a cell culture hood for 15 minutes to sterilise. Specimens of red blood cell ghosts and intact red blood cells were then prepared by pipetting 5 μL of suspension onto a mirror and lowering a cover slip gently over the drop at an angle, allowing the liquid to spread out. We also prepared specimens of the ghosts and red blood cells on ordinary non-reflective glass microscope slides, to serve as controls. All specimens were mounted using 4 % BSA in PBS ($n = 1.34$) [197] to match the average refractive index of the membrane, and imaged with a 100x/1.40 N.A. oil immersion objective. The excitation wavelengths used were the 543 nm line of a Helium-neon laser for DiI, with an average power of about 1–3 μW at the specimen, and the 488 nm of the Argon laser for DiO, with an average power of about 3 μW at the specimen, and the fluorescence signal was detected at 555–655 nm for DiI and 498–598 nm for DiO.

With the ghosts on a slide, and therefore without standing-wave exci-

tation, we would expect to see, and did see, only the bright outline of the cell, as shown in Fig. 5.9c. With standing-wave excitation using a mirror, we saw a well-defined pattern of fringes, shown in Figs. 5.9a and 5.9b, as a result of multiple planes of fluorescence excitation due to the standing-wave antinodes. With the specimens of intact red blood cells mounted on top of a mirror, we also observed multiple planes of fluorescence in the membrane, as shown in Figs. 5.9d and 5.9e. In the control without the mirror, the fluorescence again comes only from the cell outline, as shown in Fig. 5.9f. Using 488 nm excitation, we have an axial resolution of $\lambda/4n \approx 90$ nm from the full width at half maximum of the high-intensity excitation light at the antinodes. This ability to simultaneously visualise red blood cells at multiple planes reveals three-dimensional structures such as the long membrane protrusions visible in Figs. 5.9b and 5.9e and could prove useful in the study of abnormally-shaped red blood cells, such as occur in blood disorders [198, 199, 200] and and in the study of the mechanisms of parasite invasion and egress in diseases which involve the red blood cell membrane, such as malaria [201, 202, 203, 204, 205, 206].
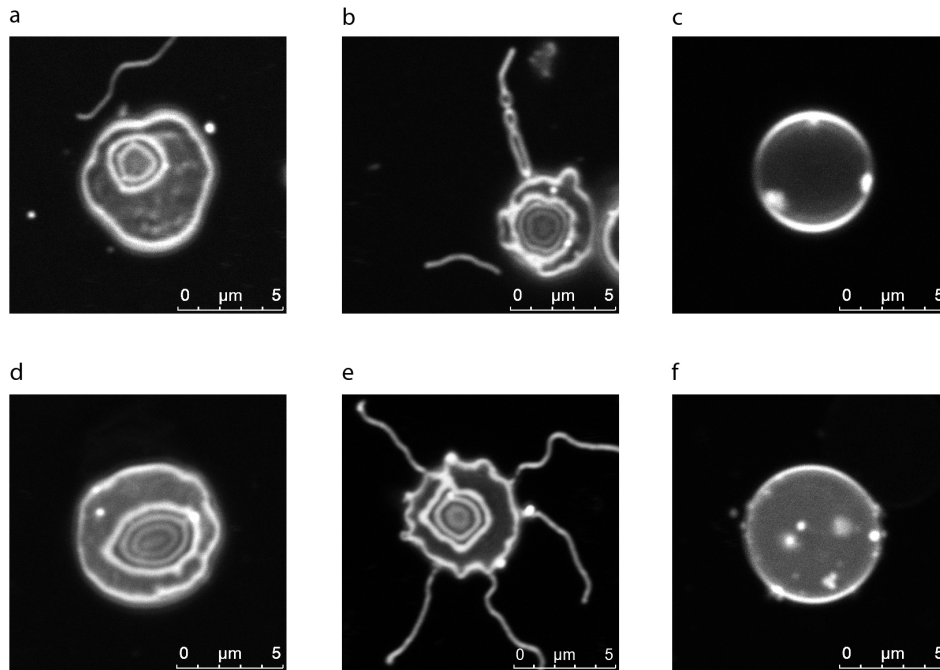
Figure 5.9: Precise contour-mapping of the red blood cell membrane. Fringes in red blood cell ghosts (*a* and *b*) and intact red blood cells (*d* and *e*) from multiplanar excitation of fluorescence at the standing-wave antinodes. The cells were stained with the membrane-specific dyes DiI (*a*, *b* and *d*) and DiO (*e*), and mounted on top of a mirror using 4 % BSA in PBS (n=1.34) to match the average refractive index of the membrane. Using an excitation wavelength of 488 nm for DiO, the axial resolution from the full width at half maximum of the high-intensity excitation light at the antinodes is $\lambda/4n \approx 90$ nm. Control specimens of red blood cell ghosts (*c*) and intact red blood cells (*f*) mounted on ordinary non-reflective glass microscope slides emit fluorescence only at the outline of the cell. Scale bar=5 μm.

165

5.3 Two-photon standing-wave microscopy

We sought to extend our standing-wave experiments in a laser scanning microscope further to include two-photon excitation, which has the advantage of inherent optical sectioning due to the confinement of the excitation to the focal plane [41, 43]. We sought to investigate whether the excitation confinement would lead to a sharpening of the fringes produced by fluorescence excitation at the antinodes in comparison with single-photon excitation, because in contrast to single-photon excitation where the excitation light generates fluorescence from a thick volume (at the focal plane as well as above and below it), two-photon excitation is localised to the focal plane and therefore the fluorescence should originate from a much thinner slice in z. This confinement of fluorescence excitation removes the need for confocal detection (a requirement in single-photon laser scanning microscopy to reject out-of-focus fluorescence not located at the focal plane [29, 33, 34]) and minimises photobleaching and photodamage [41, 43].

We used a coverslip with the underside coated with a thin layer of fluorescein dye as specimen, prepared in the manner described in Sec. 5.2.1. We arranged for this coverslip to lie at a small angle with respect to a mirror, as shown in Fig. 5.10a. We obtained an accurate measurement of the angle of inclination by using the reflection image from the laser scanning microscope, measuring the distance the reflection band moved laterally as the specimen was moved axially [207]. The lateral movement of the reflection band could be recorded in real-time if a slow scan was used, as we show in Fig. 5.10b. The intensity profiles through the shifted and unshifted parts of the reflection band (Fig. 5.10c) shows that movement of the specimen in the axial direction

166

by 25 μm displaces the bright band of reflection by 272 μm, which gives an angle of 5.3° from $tan\ \theta = axial\ displacement/lateral\ displacement$. This measurement was repeated four more times, using axial displacements of 5, 10, 15 and 20 μm, giving angles of inclinations of 5.3, 5.2, 5.3 and 5.4°, respectively. We therefore use an inclination angle of 5.3° where it is required.

For two-photon excitation, we scanned the specimen with a 20x/0.70 N.A. dry objective using the 800 nm output from a femtosecond-pulsed Ti:sapphire laser (Chameleon Ultra II, Coherent, Inc., USA). The two-photon excitation spectrum of fluorescein has a peak at around 800 nm [124]. We detected the fluorescence signal at 510–610 nm and observed a series of bright fringes of fluorescence where the fluorescein cut the standing-wave antinodes, separated by dark fringes with no fluorescence excitation where the fluorescein crossed the nodes, as shown in Fig. 5.10d. This result replicates Wiener's experiment [59] in a two-photon laser scanning microscope.

In the same way that Wiener estimated the wavelength of green light to be 550 nm from the separation between blackened lines in his layer of film, we also calculated the wavelength of excitation from the fringe spacing in Fig. 5.10d. Using an inclination angle of $\theta = 5.3°$ from above, the wavelength of excitation is obtained from $tan\ \theta = (\lambda/2n)/\Delta_s$, where Δ_s is the spacing measured laterally from the two-dimensional image, with an average value of 4293 nm. As we used a dry objective, we have $n = 1$, which gives the wavelength of excitation as $\lambda = tan\ 5.3° \times 4293\ nm \times 2 = 796$ nm, which has a 0.5 % difference from the actual value of 800 nm used.
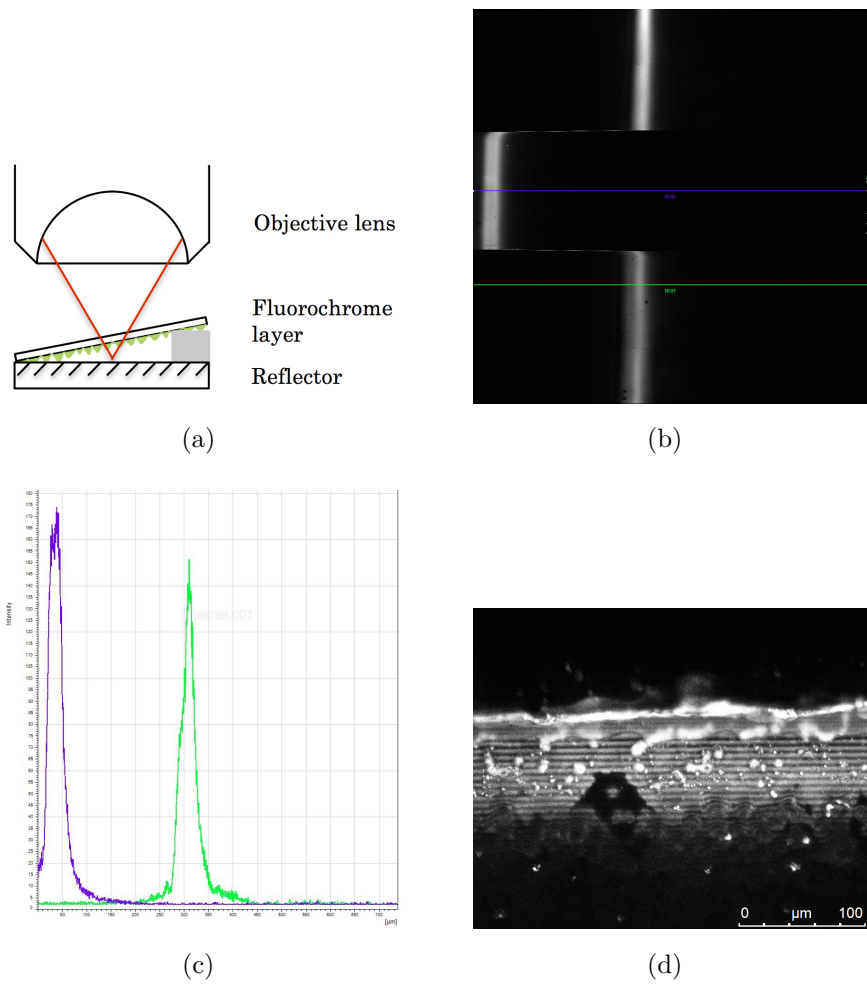
Figure 5.10: Two-photon standing-wave excitation of fluorescence. (*a*) Experimental setup showing a glass coverslip coated with a thin layer of fluorescein made to lie at angle on top of a mirror and scanned using a Leica 20x/0.70 N.A. dry objective. (*b*) Lateral movement of the reflection from the coverslip as the specimen is moved axially using a slow scan. (*c*) Intensity profiles through the shifted and unshifted parts of the reflection band show a lateral movement of 272 μm from 25 μm of axial movement. (*d*) Fluorescence image showing parallel fringes from multiple planes of two-photon excitation at the standing-wave antinodes. *Scale bar* = 75 μm.

168

A comparison of the fringes from two-photon standing-wave excitation, shown again in Fig. 5.11a, with the fringes from single-photon excitation in the same specimen (Fig. 5.11b) imaged under the same conditions except for the excitation wavelength, which was changed to 488 nm, fails to show a sharpening of the fringes in the two-photon standing-wave-excited image. For a further comparison, we also performed two-photon standing-wave excitation in the surface membrane of DiI-stained red blood cells, prepared using the same protocol described in Sec. 5.2.2. Using 700 nm for two-photon excitation of DiI [124], we obtained concentric fringes of fluorescence, shown in Fig. 5.11c. Comparing this with the single-photon standing-wave-excited image in Fig. 5.11d, obtained using 543 nm excitation, also does not show a sharpening of the fringes in the two-photon standing-wave-excited image. However, a comparison of the fringe spacings between the two sets of standing-wave images (Fig. 5.11a versus Fig. 5.11b, and Fig. 5.11c versus Fig. 5.11d) shows that the fringe spacing is increased when using two-photon excitation as expected, the fringe spacing $\lambda/2n$ being a function of the wavelength and refractive index only. The absence of fringe sharpening can be attributed to the fact that the fluorescence fringe thickness in standing-wave excitation, which is the full width at half maximum of the high-intensity peaks at the antinodes, is also a function of the excitation wavelength and refractive index only, given by $\lambda/4n$. Perhaps this negative result is what one should expect from the fact that even though two-photon excitation limits the excitation of fluorescence within the focal plane, it does not, by itself, increase the image resolution, the resolution spot being in fact being larger in the two-photon case compared with single-photon excitation because of

169

the longer wavelengths used [44].

(a)   (b)

(c)   (d)
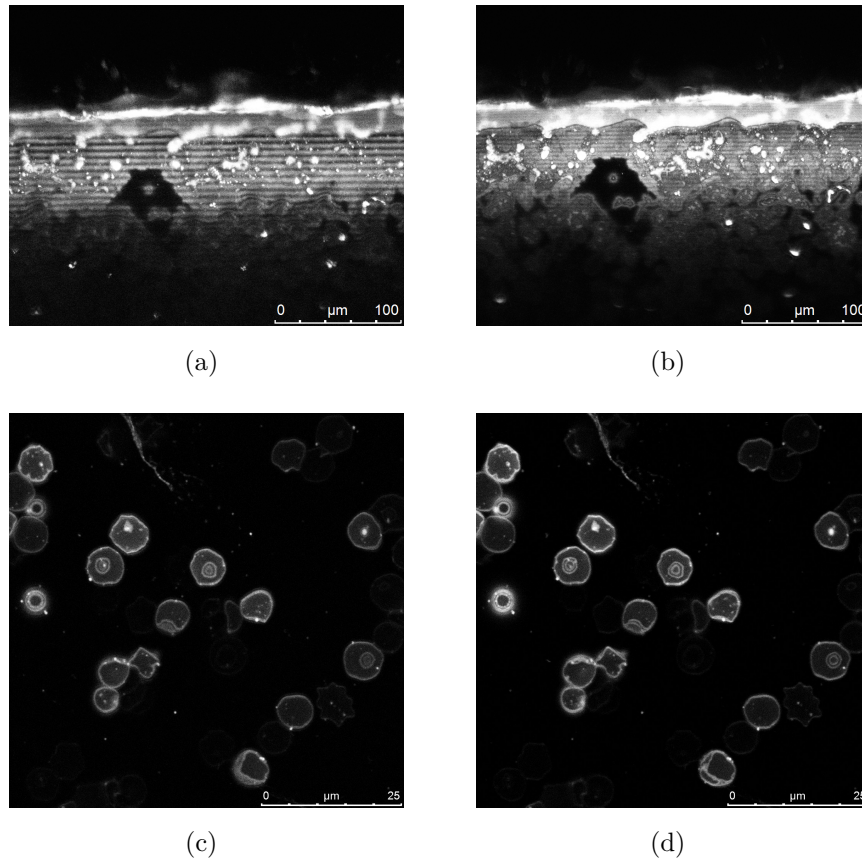
Figure 5.11: Comparison of two-photon and single-photon standing-wave excited fluorescence. (a) Parallel fringes of fluorescence from two-photon standing-wave excitation of fluorescein on a tilted coverslip using a wavelength of 800 nm. (b) Single-photon standing-wave-excited image of the same specimen using 488 nm excitation, showing reduced fringe spacing but no fringe sharpening. *Scale bar* = 75 μm. (c) Concentric fluorescence fringes from two-photon standing-wave excitation of red blood cells stained with DiI. (d) Single-photon standing-wave-excited image of the same red blood cells. The fringes are again farther apart in the two-photon case as result of the longer wavelength used, but fringe sharpening is absent. *Scale bar* = 25 μm.

5.4 Conclusion

A new method of obtaining super-resolved sections using standing-wave excitation in a confocal laser scanning microscope has been presented, with an axial resolution of ≈ 90 nm, and with the added benefit of multiplanar excitation at the standing-wave antinodes, separated by ≈ 180 nm. Using model specimens of planoconvex silica coated with a monolayer of fluorescent dye, we have obtained concentric fluorescence fringes from fluorescence excitation at multiple antinodal planes. We have shown that from one such two-dimensional fluorescence image, it is possible to reconstruct the specimen in three dimensions. The origin of apparently planar antinodes in a laser scanning microscope, where the focussed spot gives curved antinodes, has been discussed. The standing-wave antinodes are indeed curved in laser scanning, but are limited to the central area of the objective field and as point-by-point scanning is taking place, the small emission in the curve is assigned to the central pixel.

An interesting result from standing-wave excitation is the radial modulation of the fringes when the emission is detected using a small spectral bandwidth. The modulation has a frequency proportional to the Stokes shift of the fluorophore and has been shown to be a moiré pattern arising from the presence (and detection) of both the excitation standing-wave field and the emission standing-wave field. This phenomenon can prove useful in studies involving multiple colocalised dyes, to obtain even more structural information axially than what is already available with standing-wave excitation at a wide (100 nm) bandwidth of detection.

A useful application of standing-wave excitation in cellular imaging has

been presented, utilising the advantage of fluorescence excitation at multiple planes to obtain precise contour maps of the surface membrane of red blood cells. The contours of the red cell membrane show three-dimensional information and it is hoped that it proves useful in the study of blood disorders associated with the shape of red blood cells, and perhaps more importantly, in blood diseases such as malaria where the offending parasite introduces self-serving changes to the red cell membrane.

Finally, results from our investigation of whether sharpening of the fringes occurs in two-photon standing-wave excitation have been presented. Our experiments with model specimens of dye coatings on coverslips and also specimens of red blood cells show that since the excitation in standing-wave illumination is already confined to the high intensity peaks at the antinodes, the width of the fringes axially is dictated only by the wavelength of excitation and the refractive index of the medium and so fringe sharpening is not observed.

Chapter 6

Conclusion

6.1   Summary

In this thesis, I have discussed my work on the use of nonlinear and interference techniques in improving the performance of the light microscope.

In Chapter 2, I discussed my work on a homebuilt coherent anti-Stokes Raman scattering microscope, useful for label-free imaging of cells and tissues, and a homebuilt two-photon fluorescence microscope that used a sum-frequency generated source, appropriate for fluorescence excitation in the ultraviolet region. In the context of these two microscopes which both use wave-mixing, I also discussed an alignment device for looking at beam alignment simultaneously in the near-field and far-field. I have shown that by using a telephoto pair and a short focal length lens directing the beams to the same camera, spatial beam overlap, required in both the coherent anti-Stokes Raman scattering process and in sum frequency generation, is evaluated and achieved quickly and efficiently, speeding up the process of

aligning the beams and actual imaging.

In Chapter 3, I discussed the implementation of a confocal laser scanning setup for the Mesolens, a giant microscope objective built to address the problem of the minute field of view available in the laser scanning confocal microscope, making it unsuitable for fast imaging of large-volume specimens. I showed some of our early issues with the confocal Mesolens, particularly with jitter in the scanning mirrors, but although the jitter made the lateral resolution slightly worse than the theoretical value of 0.65 μm, I showed that the Mesolens in confocal mode excels at obtaining optical sections of whole mouse embryos, while at the same time resolving detail in the sub-cellular domain. I also presented my results with two-colour fluorescence imaging using doubly-labeled mouse embryos, showing muscle fibres and blood vessels in a single image, and ended the chapter by presenting relevant calculations relating to the use of the Mesolens in the two-photon excitation of fluorescence.

In Chapter 4, I presented our work on a widefield two-photon microscope, much easier to implement and cheaper than its laser-scanning counterpart, and capable of recording images at much higher frame rates of 100 frames per second. I showed the usefulness of this imaging method in the recording of fast synaptic events in neurones. I also showed that the widefield two-photon microscope is less phototoxic than its single-photon counterpart, making it advantageous for live cell microscopy. Although other methods have been developed in order to speed up two-photon microscopy, for applications particularly in neuroscience studies, I have shown that compared with these techniques, our method is simple to build and use and not costly

to implement, and argued that it should promote the wider use of two-photon microscopy in biomedical imaging in general.

In Chapter 5, I discussed my work on standing-wave excitation of fluorescence in a confocal microscope, a new method of obtaining super-resolved sections with the added benefit of visualising three-dimensional structure from a single image by virtue of simultaneous multiplanar excitation at the antinodal planes. Using model specimens of planoconvex silica coated with a monolayer of dye, I showed that it is possible to reconstruct the specimen in three dimensions from a single two-dimensional image. I also showed the interesting result of radial modulation in the standing-wave fringes when using using a small spectral bandwidth to detect the fluorescence signal. I showed that the modulation had a frequency proportional to the Stokes shift and that it is a moiré pattern arising from the presence and detection of both the excitation standing-wave field and the emission standing-wave field. I presented my results from the application of standing-wave excitation in cellular imaging, utilising the advantage of fluorescence excitation at multiple planes to obtain precise contour maps of the surface membrane of red blood cells, which could prove proves useful in the study of blood disorders associated with the shape of red blood cells, and also in the study of blood diseases such as malaria.

6.2   Future prospects

The confocal Mesolens has attracted the enthusiastic attention of several research groups who are keen to exploit its features, spawning collaborations

with other institutions. These include a collaboration with the Biophotonics group at Dundee for light sheet imaging using the Mesolens to look at, for example, the developing chick embryo, and with the Roslin Institute and Institute of Genetics and Molecular Medicine in Edinburgh to use three-dimensional images from the confocal Mesolens to visualise and study how neuronal connections form in the developing mouse embryo. Amos and Reid are currently building the next version of the Mesolens.

An exciting prospect for the widefield two-photon microscope is its use in the long-term imaging, spanning days, of cellular processes that can be tracked by calcium indicators. Specimen candidates are the developing tadpole brain or the zebrafish embryo. Long-term studies such as this currently cannot be performed because of photodomage.

For the work on standing-wave excitation of fluorescence, the natural next step is the utilisation of the moiré pattern when detecting the fluorescence emission at small bandwidths, a spectral approach to extracting more structural information from the specimen. Using this approach, detecting the fluorescence signal simultaneously at three different wavelengths will produce an image with structures excited by three groups of antinodes shifted axially from each other with a separation proportional to the difference in the wavelengths of detection.

The standing-wave experiment can also be performed in a widefield configuration, allowing for fast acquisition of images using a CCD camera. A fast imaging setup such as this, capable of showing 3D morphology, would be useful in the study of fast structural events such as the changes undergone by the platelet membrane during activation.

Finally, the contours generated by standing-wave excitation in the red blood cell can be used to make measurements of the surface areas of red cells both uninfected and infected with malaria. A quantification of the distribution of surface areas in the red cell membrane done in this way can contribute towards understanding how the malaria parasite uses and adds to the red cell surface area during infection.

It is my hope that with the prospects listed above, and more that might become apparent along the way, the work and techniques presented here can make a concrete contribution to biomedical science.

Bibliography

[1] A. N. Disney, C. F. Hill, and W. E. W. Baker. *Origin And Development of the Microscope: As Illustrated by Catalogues of the Instruments And Accessories, In the Collections of the Royal Microscopical Society, Together With Bibliographies of Original Authorities, 30 Plates And 36 Text-figures.* The Royal Microscopical Society, London, 1928.

[2] R. S. Clay and T. H. Court. *The History of the Microscope, Compiled from Original Instruments and Documents, Up to the Introduction of the Achromatic Microscope.* Charles Griffin & Co., London, 1932.

[3] L. L. Woodruff. Microscopy before the nineteenth century. *Am. Nat.*, 73(749):485–516, 1939.

[4] C. S. Ball. The early history of the compound microscope. *Bios*, 37(2):51–60, 1966.

[5] S. Bradbury. *The Evolution of the Microscope.* Pergamon Press, Oxford, 1967.

[6] S. H. Gage. *The Microscope and Histology, Part I. The Microscope and Microscopical Methods.* James W. Queen & Co., Philadelphia, 1896.

[7] A. Hughes. Progress in microscopy, 1663–1673. *J. R. Microsc. Soc.*, 83(1-2):25–28, 1964.

[8] Clara Sue Ball. The `Apiarium`: An early example of microscopic study. In *Proceedings of the Oklahoma Academy of Science*, volume 46, pages 148–151, Oklahoma, 1966.

[9] D. Bardell. The first record of microscopic observations. *BioScience*, 33(1):36–38, 1983.

[10] D. Freedberg. *The eye of the lynx: Galileo, his friends, and the beginnings of modern natural history.* University of Chicago Press, Chicago, 2003.

[11] J. Young. Malpighi's "De Pulmonibus". *Proc. R. Soc. Med.*, 23(1):1–11, 1929.

[12] R. Hooke. *Micrographia: Or Some Physiological Descriptions of Minute Bodies Made by Magnifying Glasses. With Observations and Inquiries Thereupon.* John Martyn, London, 1667.

[13] H. Gest. The discovery of microorganisms by Robert Hooke and Antoni Van Leeuwenhoek, fellows of the Royal Society. *Notes Rec. R. Soc.*, 58(2):187–201, 2004.

[14] J. Bolam. The botanical works of Nehemiah Grew, FRS (1641-1712). *Notes Rec. R. Soc.*, 27:219–231, 1973.

[15] B. J. Ford. The van Leeuwenhoek specimens. *Notes Rec. R. Soc.*, 36(1):37–59, 1981.

[16] C. Dobell. *Antony van Leeuwenhoek and His "Little Animals." Being Some Account of the Father of Protozoology and Bacteriology and his Multifarious Discoveries in these Disciplines. Collected, Translated, and Edited, from his Printed Works, Unpublished Manuscripts, and Contemporary Records.* Swets & Zeitlinger, Amsterdam, 1932.

[17] J. R. Porter. Antony van Leeuwenhoek: Tercentenary of his discovery of bacteria. *Bacteriol. Rev.*, 40(2):260, 1976.

[18] B. J. Ford. Cytological examination of Leeuwenhoek's first microbial specimens. *Tissue Cell*, 14(2):207–217, 1982.

[19] O. Stapf. *Lignum nephriticum. (Eysenhardtia amorphoides, `H.B.K.`).* *Bull. Misc. Inform. (R. Bot. Gard., Kew)*, 1909(7):293–305, 1909.

[20] G. G. Stokes. On the change of refrangibility of light. *Phil. Trans. R. Soc.*, 142:463–562, 1852.

[21] J. R. Lakowicz. *Principles of Fluorescence Spectroscopy.* Springer Science & Business Media, New Jersey, 3rd edition, 2007.

[22] B. R. Masters. The development of fluorescence microscopy. *eLS*, 2010.

[23] A. H. Coons, H. J. Creech, R. N. Jones, and E. Berliner. The demonstration of pneumococcal antigen in tissues by the use of fluorescent antibody. *J. Immunol.*, 45(3):159–70, 1942.

[24] A. H. Coons and M. H. Kaplan. Localization of antigen in tissue cells `II`. Improvements in a method for the detection of antigen by means of fluorescent antibody. *J. Exp. Med.*, 91(1):1–13, 1950.

[25] R. Yuste. Fluorescence microscopy today. *Nat. Methods*, 2(12):902–904, 2005.

[26] I. C. Ghiran. Introduction to fluorescence microscopy. In *Light Microscopy*, pages 93–136. Springer, 2011.

[27] M. Minsky. Microscopy apparatus. U.S. Patent No. 3,013,467, 19 December 1961.

[28] M. Minsky. Memoir on inventing the confocal scanning microscope. *Scanning*, 10(4): 128–138, 1988.

[29] G. J. Brakenhoff, H. T. M. Van der Voort, E. A. Van Spronsen, W. A. M. Linnemans, and N. Nanninga. Three-dimensional chromatin distribution in neuroblastoma nuclei shown by confocal scanning laser microscopy. *Nature*, 317: 748–749, 1985.

[30] K. Carlsson, P.-E. Danielsson, A. Liljeborg, L. Majlöf, R. Lenz, and N. Åslund. Three-dimensional microscopy using a confocal laser scanning microscope. *Opt. Lett.*, 10(2): 53–55, 1985.

[31] A. Draaijer and P. M. Houpt. A standard video-rate confocal laser-scanning reflection and fluorescence microscope. *Scanning*, 10(4): 139–145, 1988.

[32] S. R. Goldstein, T. Hubin, S. Rosenthal, and C. Washburn. A confocal video-rate laser-beam scanning reflected-light microscope with no moving parts. *J. Microsc.*, 157(1): 29–38, 1990.

[33] J. G. White, W. B. Amos, and M. Fordham. An evaluation of confocal versus conventional imaging of biological structures by fluorescence light microscopy. *J. Cell Biol.*, 105(1): 41–48, 1987.

[34] W. B. Amos, J. G. White, and M. Fordham. Use of confocal imaging in the study of biological structures. *Appl. Opt.*, 26(16): 3239–3243, 1987.

[35] W. B. Amos and J. G. White. How the confocal laser scanning microscope entered biological research. *Biol. Cell*, 95(6):335–342, 2003.

[36] C. Xu, W. Zipfel, J. B. Shear, R. M. Williams, and W. W. Webb. Multiphoton fluorescence excitation: new spectral windows for biological nonlinear microscopy. *Proc. Natl. Acad. Sci. U.S.A.*, 93(20):10763–10768, 1996.

[37] J. Mertz. Nonlinear microscopy: new techniques and applications. *Curr. Opin. Neurobiol.*, 14(5):610–616, 2004.

[38] T. Meyer, M. Schmitt, B. Dietzek, and J. Popp. Accumulating advantages, reducing limitations: Multimodal nonlinear imaging in biomedical sciences–the synergy of multiple contrast mechanisms. *J. Biophotonics*, 6(11-12): 887–904, 2013.

[39] F. Helmchen and W. Denk. Deep tissue two-photon microscopy. *Nat. Methods*, 2(12): 932–940, 2005.

[40] M. Göeppert-Mayer. Uber elementarakte mit zwei quantensprungen (on elementary processes with two quantum steps). *Ann. Phys.*, 9: 273–294, 1931.

[41] W. Denk, J. H. Strickler, and W. W. Webb. Two-photon laser scanning fluorescence microscopy. *Science*, 248(4951): 73–76, 1990.

[42] R. M. Williams, D. W. Piston, and W. W. Webb. Two-photon molecular excitation provides intrinsic 3-dimensional resolution for laser-based microscopy and microphotochemistry. *FASEB J.*, 8(11): 804–813, 1994.

[43] W. Denk. Two-photon excitation in functional biological imaging. *J. Biomed. Opt.*, 1(3): 296–304, 1996.

[44] D. W. Piston. Imaging living cells and tissues by two-photon excitation microscopy. *Trends Cell Biol.*, 9(2): 66–69, 1999.

[45] T. G. Phan and A. Bullen. Practical intravital two-photon microscopy for immunological research: faster, brighter, deeper. *Immunol. Cell Biol.*, 88(4):438–444, 2010.

[46] R. W. Boyd. *Nonlinear Optics*. Academic Press, San Diego, California, 2nd edition, 2003.

[47] A. Zumbusch, G. R. Holtom, and X. S. Xie. Three-dimensional vibrational imaging by coherent anti-Stokes Raman scattering. *Phys. Rev. Lett.*, 82(20): 4142, 1999.

[48] M. Hashimoto, T. Araki, and S. Kawata. Molecular vibration imaging in the fingerprint region by use of coherent anti-Stokes Raman scattering microscopy with a collinear configuration. *Opt. Lett.*, 25(24): 1768–1770, 2000.

[49] M. D. Duncan, J. Reintjes, and T. J. Manuccia. Scanning coherent anti-Stokes Raman microscope. *Opt. Lett.*, 7(8): 350–352, 1982.

[50] M. D. Duncan, J. Reintjes, and T. J. Manuccia. Imaging biological compounds using the coherent anti-Stokes Raman scattering microscope. *Opt. Eng.*, 24(2): 352, 1985.

[51] A. Volkmer. Vibrational imaging and microspectroscopies based on coherent anti-Stokes Raman scattering microscopy. *J. Phys. D: Appl. Phys.*, 38(5): R59, 2005.

[52] C. L. Evans and X. S. Xie. Coherent anti-Stokes Raman scattering microscopy: chemical imaging for biology and medicine. *Annu. Rev. Anal. Chem.*, 1: 883–909, 2008.

[53] A. Volkmer, J.-X. Cheng, and X. S. Xie. Vibrational imaging with high sensitivity via epidetected coherent anti-Stokes Raman scattering microscopy. *Phys. Rev. Lett.*, 87(2): 23901, 2001.

[54] J.-X. Cheng, Y. K. Jia, G. Zheng, and X. S. Xie. Laser-scanning coherent anti-stokes raman scattering microscopy and applications to cell biology. *Biophys. J.*, 83(1):502–509, 2002.

[55] Xiaolin Nan, Eric O Potma, and X Sunney Xie. Nonperturbative chemical imaging of organelle transport in living cells with coherent anti-Stokes raman scattering microscopy. *Biophysical journal*, 91(2):728–735, 2006.

[56] C. L. Evans, E. O. Potma, M. Puoris' haag, D. Côté, C. P. Lin, and X. S. Xie. Chemical imaging of tissue in vivo with video-rate coher-

ent anti-Stokes Raman scattering microscopy. *Proc. Natl. Acad. Sci. U.S.A.*, 102(46):16807–16812, 2005.

[57] C. L. Evans, X. Xu, S. Kesari, X. S. Xie, S. T. C. Wong, and G. S. Young. Chemically-selective imaging of brain structures with CARS microscopy. *Opt. Express*, 15(19):12076–12087, 2007.

[58] G. B. Airy. On the phænomena of Newton's rings when formed between two transparent substances of different refractive powers. *Philos. Mag. J. Sci.*, 2(7):20–30, 1833.

[59] O. Wiener. Stehende lichtwellen und die schwingungsrichtung polarisirten lichtes. *Ann. Phys.*, 276: 203–243, 1890.

[60] R. W. Ditchburn. *Light.* Blackie & Son Limited, London & Glasgow, 1958.

[61] F. A. Jenkins and H. E. White. *Fundamentals of Optics.* McGraw-Hill Book Company, Inc., New York, 4th edition, 1976.

[62] A. S. G. Curtis. The mechanism of adhesion of cells to glass. A study by interference reflection microscopy. *J. Cell Biol.*, 20(2):199–215, 1964.

[63] D. Gingell and I. Todd. Interference reflection microscopy. A quantitative theory for image interpretation and its application to cell-substratum separation measurement. *Biophys. J.*, 26(3):507, 1979.

[64] B. Bailey, D. L. Farkas, D. L. Taylor, and F. Lanni. Enhancement of axial resolution in fluorescence microscopy by standing-wave excitation. *Nature*, 366: 44–48, 1993.

[65] Y. Fu, H. Wang, R. Shi, and J.-X. Cheng. Second harmonic and sum frequency generation imaging of fibrous astroglial filaments in ex vivo spinal tissues. *Biophys. J.*, 92(9): 3251–3259, 2007.

[66] V. Raghunathan, Y. Han, O. Korth, N.-H. Ge, and E. O. Potma. Rapid vibrational imaging with sum frequency generation microscopy. *Opt. Lett.*, 36(19): 3891–3893, 2011.

[67] H.-W. Wang, V. Simianu, M. J. Locker, J.-X. Cheng, and M. Sturek. Stent-induced coronary artery stenosis characterized by multimodal nonlinear optical microscopy. *J. Biomed. Opt.*, 16(2): 021110, 2011.

[68] E. S. Lee, S.-W. Lee, J. Hsu, and E. O. Potma. Vibrationally resonant sum-frequency generation microscopy with a solid immersion lens. *Biomed. Opt. Exp.*, 5(7): 2125–2134, 2014.

[69] F. Masia, W. Langbein, P. Watson, and P. Borri. Resonant four-wave mixing of gold nanoparticles for three-dimensional cell microscopy. *Opt. Lett.*, 34(12): 1816–1818, 2009.

[70] R. Selm, G. Krauss, A. Leitenstorfer, and A. Zumbusch. Simultaneous second-harmonic generation, third-harmonic generation, and four-wave mixing microscopy with single sub-8 fs laser pulses. *Appl. Phys. Lett.*, 99(18): 181124, 2011.

[71] P. Mahou, N. Olivier, G. Labroille, L. Duloquin, J.-M. Sintes, N. Peyriéras, R. Legouis, D. Débarre, and E. Beaurepaire. Combined third-harmonic generation and four-wave mixing microscopy of tissues and embryos. *Biomed. Opt. Exp.*, 2(10): 2837–2849, 2011.

[72] A. D. Slepkov, A. M. Barlow, A. Ridsdale, P. J. McGinn, and A. Stolow. *In vivo* hyperspectral CARS and FWM microscopy of carotenoid accumulation in *H. pluvialis*. In *SPIE BiOS*, page 893709. International Society for Optics and Photonics, 2014.

[73] M. Balu, T. Baldacchini, J. Carter, T. B. Krasieva, R. Zadoyan, and B. J. Tromberg. Effect of excitation wavelength on penetration depth in nonlinear optical microscopy of turbid media. *J. Biomed. Opt.*, 14(1): 010508, 2009.

[74] W. Min, S. Lu, M. Rueckel, G. R. Holtom, and X. S. Xie. Near-degenerate four-wave-mixing microscopy. *Nano Lett.*, 9(6): 2423–2426, 2009.

[75] T. Hellerer, A. Schiller, G. Jung, and A. Zumbusch. Coherent anti-Stokes Raman scattering (CARS) correlation spectroscopy. *ChemPhysChem*, 3(7): 630–633, 2002.

[76] D. J. Jones, E. O. Potma, J.-X. Cheng, B. Burfeindt, Y. Pang, J. Ye, and X. S. Xie. Synchronization of two passively mode-locked, picosecond lasers within 20 fs for coherent anti-Stokes Raman scattering microscopy. *Rev. Sci. Instrum.*, 73(8): 2843–2848, 2002.

[77] X. D. Zhu, H. Suhr, and Y. R. Shen. Surface vibrational spectroscopy by infrared-visible sum frequency generation. *Phys. Rev. B*, 35(6): 3047, 1987.

[78] T. J. Weeks and T. R. Huser. Differential imaging of biological structures with doubly-resonant coherent anti-Stokes Raman scattering (CARS). *J. Vis. Exp.*, 44:e2085, 2010.

[79] P. D. Maker and R. W. Terhune. Study of optical effects due to an induced polarization third order in the electric field strength. *Phys. Rev.*, 137(3A): A801, 1965.

[80] M. D. Levenson, C. Flytzanis, and N. Bloembergen. Interference of resonant and nonresonant three-wave mixing in diamond. *Phys. Rev. B*, 6(10): 3962, 1972.

[81] M. D. Levenson and N. Bloembergen. Dispersion of the nonlinear optical susceptibility tensor in centrosymmetric media. *Phys. Rev. B*, 10(10): 4447, 1974.

[82] R. F. Begley, A. B. Harvey, and R. L. Byer. Coherent anti-Stokes Raman spectroscopy. *Appl. Phys. Lett.*, 25(7): 387–390, 1974.

[83] G. J. Puppels, F. F. M. De Mul, C. Otto, J. Greve, M. Robert-Nicoud, D. J. Arndt-Jovin, and T. M. Jovin. Studying single living cells and chromosomes by confocal Raman microspectroscopy. *Nature*, 347:301–303, 1990.

[84] N. M. Sijtsema, S. D. Wouters, C. J. D. Grauw, C. Otto, and J. Greve. Confocal direct imaging Raman microscope: design and applications in biology. *Appl. Spectrosc.*, 52(3):348–355, 1998.

[85] T. Dieing, O. Hollricher, and J. Toporski. *Confocal Raman Microscopy*, volume 158. Springer Science & Business Media, Berlin, 2011.

189

[86] T. H. Maiman. Stimulated optical radiation in ruby. *Nature*, 187(4736): 493–494, 1960.

[87] C. H. Townes. The first laser. In L. Garwin and T. Lincoln, editors, *A Century of Nature: Twenty-One Discoveries that Changed Science and the World*, pages 107–112. University of Chicago Press, Chicago, 2010.

[88] W. Kaiser and C. G. B. Garrett. Two-photon excitation in CaF_2:eu^{2+}. *Phys. Rev. Lett.*, 7(6): 229–231, 1961.

[89] D. A. Kleinman. Laser and two-photon processes. *Phys. Rev.*, 125(1): 87–88, 1962.

[90] I. D. Abella. Optical double-photon absorption in cesium vapor. *Phys. Rev. Lett.*, 9(11): 453–455, 1962.

[91] P. F. Curley, A. I. Ferguson, J. G. White, and W. B. Amos. Application of a femtosecond self-sustaining mode-locked Ti:sapphire laser to the field of laser scanning confocal microscopy. *Opt. Quant. Electron.*, 24(8): 851–859, 1992.

[92] S. Huang, A. A. Heikal, and W. W. Webb. Two-photon fluorescence spectroscopy and microscopy of NAD(P)H and flavoprotein. *Biophys. J.*, 82(5): 2811–2825, 2002.

[93] E. Hecht. *Optics.* Addison Wesley Longman, Inc., Reading, Massachusetts, 3rd edition, 1998.

[94] G. Ghosh. Sellmeier coefficients and dispersion of thermo-optic coefficients for some optical glasses. *Appl. Opt.*, 36(7): 1540–1546, 1997.

[95] W. Zhang, M. Parsons, and G. McConnell. Flexible and stable optical parametric oscillator based laser system for coherent anti-Stokes Raman scattering microscopy. *Micros. Res. Tech.*, 73(6): 650–656, 2010.

[96] R. L. Byer. Optical parametric oscillators. In H. Rabin and C. L. Tang, editors, *Quantum Electronics: A Treatise, Volume I: Nonlinear Optics, Part B*, pages 588–694. Academic Press, Inc., New York, 1975.

[97] L. Huang, D. Hui, D. J. Bamford, S. J. Field, I. Mnushkina, L. E. Myers, and J. V. Kayser. Periodic poling of magnesium-oxide-doped stoichiometric lithium niobate grown by the top-seeded solution method. *Appl. Phys. B*, 72(3):301–306, 2001.

[98] G. Norris, R. Amor, J. Dempster, W. B. Amos, and G. McConnell. Increased signals from short-wavelength-excited fluorescent molecules using sub-Ti: Sapphire wavelengths. *J. Microsc.*, 248(2): 200–207, 2012.

[99] Q.-T. Nguyen, P. S. Tsai, and D. Kleinfeld. MPScope: a versatile software suite for multiphoton microscopy. *J. Neurosc. Meth.*, 156(1):351–359, 2006.

[100] D. K. Padilla. Structural resistance of algae to herbivores. *Mar. Biol.*, 90(1): 103–109, 1985.

[101] W. J. Weninger and T. Mohun. Phenotyping transgenic embryos: a rapid 3-d screening method based on episcopic fluorescence image capturing. *Nat. Genet.*, 30(1):59–65, 2002.

[102] J. Streicher, M. A. Donat, B. Strauss, R. Spörle, K. Schughart, and G. B. Müller. Computer-based three-dimensional visualization of developmental gene expression. *Nat. Genet.*, 25(2):147–152, 2000.

[103] E. S. Lein, M. J. Hawrylycz, N. Ao, M. Ayres, A. Bensinger, A. Bernard, A. F. Boe, M. S. Boguski, K. S. Brockway, E. J. Byrnes, et al. Genome-wide atlas of gene expression in the adult mouse brain. *Nature*, 445(7124):168–176, 2007.

[104] T. Ragan, L. R. Kadiri, K. U. Venkataraju, K. Bahlmann, J. Sutin, J. Taranda, I. Arganda-Carreras, Y. Kim, H. S. Seung, and P. Osten. Serial two-photon tomography for automated ex vivo mouse brain imaging. *Nat. Methods*, 9(3):255–258, 2012.

[105] A. Li, H. Gong, B. Zhang, Q. Wang, C. Yan, J. Wu, Q. Liu, S. Zeng, and Q. Luo. Micro-optical sectioning tomography to obtain a high-resolution atlas of the mouse brain. *Science*, 330(6009):1404–1408, 2010.

[106] J. Sharpe, U. Ahlgren, P. Perry, B. Hill, A. Ross, J. Hecksher-Sørensen, R. Baldock, and D. Davidson. Optical projection tomography as a tool for 3D microscopy and gene expression studies. *Science*, 296(5567):541–545, 2002.

[107] J. Sharpe. Optical projection tomography. *Annu. Rev. Biomed. Eng.*, 6:209–228, 2004.

[108] M. D. Wong, J. Dazai, J. R. Walls, N. W. Gale, and R. M. Henkelman. Design and implementation of a custom built optical projection tomography system. *PLOS One*, 8(9):e73491, 2013.

[109] J Huisken, J. Swoger, F. Del Bene, J. Wittbrodt, and E. H. K. Stelzer. Optical sectioning deep inside live embryos by selective plane illumination microscopy. *Science*, 305(5686):1007–1009, 2004.

[110] P. J. Verveer, J. Swoger, F. Pampaloni, K. Greger, M. Marcello, and E. H. K. Stelzer. High-resolution three-dimensional imaging of large specimens with light sheet-based microscopy. *Nat. Methods*, 4(4):311–313, 2007.

[111] P. J. Keller and E. H. K. Stelzer. Quantitative in vivo imaging of entire embryos with digital scanned laser light sheet fluorescence microscopy. *Curr. Opin. Neurobiol.*, 18(6):624–632, 2008.

[112] P. J. Keller, A. D. Schmidt, J. Wittbrodt, and E. H. K. Stelzer. Reconstruction of zebrafish early embryonic development by scanned light sheet microscopy. *Science*, 322(5904):1065–1069, 2008.

[113] P. J. Keller, A. D. Schmidt, A. Santella, K. Khairy, Z. Bao, J. Wittbrodt, and E. H. K. Stelzer. Fast, high-contrast imaging of animal development with scanned light sheet-based structured-illumination microscopy. *Nature methods*, 7(8):637–642, 2010.

[114] C. J. Engelbrecht and E. H. K. Stelzer. Resolution enhancement in a light-sheet-based microscope (SPIM). *Opt. Lett.*, 31(10):1477–1479, 2006.

[115] Y. Wu, A. Ghitani, R. Christensen, A. Santella, Z. Du, G. Rondeau, Z. Bao, D. Colón-Ramos, and H. Shroff. Inverted selective plane illumination microscopy (`iSPIM`) enables coupled cell identity lineaging and neurodevelopmental imaging in Caenorhabditis elegans. *Proc. Natl. Acad. Sci. U.S.A.*, 108(43):17708–17713, 2011.

[116] S. Inoué. Foundations of confocal scanned imaging in light microscopy. In J. Pawley, editor, *Handbook of biological confocal microscopy*, pages 1–19. Springer, 3rd edition, 2006.

[117] M. J. Karkkainen, P. Haiko, K. Sainio, J. Partanen, J. Taipale, T. V. Petrova, M. Jeltsch, D. G. Jackson, M. Talikka, H. Rauvala, et al. Vascular endothelial growth factor c is required for sprouting of the first lymphatic vessels from embryonic veins. *Nat. Immunol.*, 5(1):74–80, 2004.

[118] M. H. Andersen, D. Schrama, P. thor Straten, and J. C. Becker. Cytotoxic t cells. *J. Invest. Dermatol.*, 126(1):32–41, 2006.

[119] W. B. Amos. How new science is transforming the optical microscope. Available at www.royalsociety.org. The Royal Society Leeuwenhoek Medal and Lecture, 2012.

[120] A. Saini. New lens offers scientist a brighter outlook. *Science*, 335(6076):1562–1563, 2012.

[121] R. Heim, D. C. Prasher, and R. Y. Tsien. Wavelength mutations and posttranslational autoxidation of green fluorescent protein. *Proc. Natl. Acad. Sci. U.S.A.*, 91(26):12501–12504, 1994.

[122] P. So, H. Kim, and I. Kochevar. Two-photon deep tissue ex vivo imaging of mouse dermal and subcutaneous structures. *Opt. Express*, 3(9): 339–350, 1998.

[123] G. P. Agrawal. *Nonlinear Fiber Optics.* Academic Press, San Diego, California, 2007.

[124] C. Xu and W. W. Webb. Measurement of two-photon excitation cross sections of molecular fluorophores with data from 690 to 1050 nm. *J. Opt. Soc. Am. B*, 13(3): 481–491, 1996.

[125] W. Zipfel. Two-photon excitation cross-sections. Available at www.drbio.cornell.edu. Accessed August 9, 2013.

[126] V. E. Centonze and J. G. White. Multiphoton excitation provides optical sections from deeper within scattering specimens than confocal imaging. *Biophys. J.*, 75(4): 2015–2024, 1998.

[127] G. H. Patterson and D. W. Piston. Photobleaching in two-photon excitation microscopy. *Biophys. J.*, 78(4): 2159–2162, 2000.

[128] T.-S. Chen, S.-Q. Zeng, Q.-M. Luo, Z.-H. Zhang, and W. Zhou. High-order photobleaching of green fluorescent protein inside live cells in two-photon excitation microscopy. *Biochem. Biophys. Res. Commun.*, 291(5): 1272–1275, 2002.

[129] H. Kawano, Y. Nabekawa, A. Suda, Y. Oishi, H. Mizuno, A. Miyawaki, and K. Midorikawa. Attenuation of photobleaching in two-photon excitation fluorescence from green fluorescent protein with shaped ex-

citation pulses. *Biochem. Biophys. Res. Commun.*, 311(3): 592–596, 2003.

[130] Q. T. Nguyen, N. Callamaras, C. Hsieh, and I. Parker. Construction of a two-photon microscope for video-rate Ca^{2+} imaging. *Cell Calcium*, 30(6): 383–393, 2001.

[131] G. J. Brakenhoff, J. Squier, T. Norris, A. C. Bliton, M. H. Wade, and B. Athey. Real-time two-photon confocal microscopy using a femtosecond, amplified Ti:sapphire system. *J. Microsc.*, 181(3): 253–259, 1996.

[132] D. Fittinghoff, P. Wiseman, and J. Squier. Widefield multiphoton and temporally decorrelated multifocal multiphoton microscopy. *Opt. Express*, 7(8): 273–279, 2000.

[133] R. Niesner, V. Andresen, J. Neumann, H. Spiecker, and M. Gunzer. The power of single and multibeam two-photon microscopy for high-resolution and high-speed deep tissue and intravital imaging. *Biophys. J.*, 93(7): 2519–2529, 2007.

[134] A. Deniset-Besseau, S. Leveque-Fort, M. P. Fontaine-Aupart, G. Roger, and P. Georges. Three-dimensional time-resolved fluorescence imaging by multifocal multiphoton microscopy for a photosensitizer study in living cells. *Appl. Opt.*, 46(33): 8045–8051, 2007.

[135] T. V. Truong, W. Supatto, D. S. Koos, J. M. Choi, and S. E. Fraser. Deep and fast live imaging with two-photon scanned light-sheet microscopy. *Nat. Methods*, 8(9): 757–760, 2011.

[136] X. Chen, U. Leischner, N. L. Rochefort, I. Nelken, and A. Konnerth. Functional mapping of single spines in cortical neurons in vivo. *Nature*, 475(7357): 501–505, 2011.

[137] X. Chen, U. Leischner, Z. Varga, H. Jia, D. Deca, N. L. Rochefort, and A. Konnerth. `LOTOS`-based two-photon calcium imaging of dendritic spines in vivo. *Nat. Protoc.*, 7(10): 1818–1829, 2012.

[138] Z. Varga, H. Jia, B. Sakmann, and A. Konnerth. Dendritic coding of multiple sensory inputs in single cortical neurons in vivo. *Proc. Natl. Acad. Sci. U.S.A.*, 108(37): 15420–15425, 2011.

[139] J. Y. Hwang, S. Wachsmann-Hogiu, V. K. Ramanujan, A. G. Nowatzyk, Y. Koronyo, L. K. Medina-Kauwe, Z. Gross, H. B. Gray, and D. L. Farkas. Multimodal wide-field two-photon excitation imaging: characterization of the technique for in vivo applications. *Biomed. Opt. Express*, 2(2): 356–364, 2011.

[140] A. E. Siegman. *Lasers*. University Science Books, Sausalito, California, 1986.

[141] H. Kogelnik and T. Li. Laser beams and resonators. *Appl. Opt.*, 5: 1550–1567, 1966.

[142] Scientific cmos brochure. Available at www.andor.com. Accessed March 21, 2015.

[143] J. Dempster. `WinFluor`: Fluorescence imaging & electrophysiology analysis program (2014). Available at www.strath.ac.uk. Accessed July 2, 2014.

[144] J. Gan, S. M. Greenwood, S. R. Cobb, and T. J. Bushell. Indirect modulation of neuronal excitability and synaptic transmission in the hippocampus by activation of proteinase-activated receptor-2. *Br. J. Pharmacol.*, 163(5): 984–994, 2011.

[145] C. A. Schneider, W. S. Rasband, and K. W. Eliceiri. `NIH Image` to `ImageJ`: 25 years of image analysis. *Nat. Methods*, 9(7): 671–675, 2012.

[146] M. M. Knight, S. R. Roberts, D. A. Lee, and D. L. Bader. Live cell imaging using confocal microscopy induces intracellular calcium transients and cell death. *Am. J. Physiol. Cell Physiol.*, 284(4): C1083–C1089, 2003.

[147] A. McDonald, J. Harris, D. MacMillan, J. Dempster, and G. McConnell. Light-induced Ca^{2+} transients observed in widefield epifluorescence microscopy of excitable cells. *Biomed. Opt. Express*, 3(6): 1266–1273, 2012.

[148] E. Betzig, G. H. Patterson, R. Sougrat, O. W. Lindwasser, S. Olenych, J. S. Bonifacino, M. W. Davidson, J. Lippincott-Schwartz, and H. F. Hess. Imaging intracellular fluorescent proteins at nanometer resolution. *Science*, 313(5793): 1642–1645, 2006.

[149] T. J. Mitchison, K. E. Sawin, J. A. Theriot, K. Gee, and A. Mallavarapu. Caged fluorescent probes. *Methods Enzymol.*, 291: 63–78, 1998.

[150] A. Schönle and S. W. Hell. Heating by absorption in the focus of an objective lens. *Opt. Lett.*, 23(5): 325–327, 1998.

[151] R. Y. Tsien, L. Ernst, and A. Waggoner. Fluorophores for confocal microscopy: photophysics and photochemistry. In J. Pawley, editor, *Handbook of Biological Confocal Microscopy*, pages 338–352. Springer, New York, 2006.

[152] C. J. Ledgerwood, S. M. Greenwood, R. R. Brett, J. A. Pratt, and T. J. Bushell. Cannabidiol inhibits synaptic transmission in rat hippocampal cultures and slices via multiple receptor pathways. *Br. J. Pharmacol.*, 162(1): 286–294, 2011.

[153] N. C. Danbolt. Glutamate uptake. *Prog. Neurobiol.*, 65(1):1–105, 2001.

[154] G. H. Patterson, S. M. Knobel, W. D. Sharif, S. R. Kain, and D. W. Piston. Use of the green fluorescent protein and its mutants in quantitative fluorescence microscopy. *Biophys. J.*, 73(5): 2782, 1997.

[155] N. Malkani and J. A. Schmid. Some secrets of fluorescent proteins: distinct bleaching in various mounting fluids and photoactivation of cyan fluorescent proteins at YFP-excitation. *PLOS ONE*, 6(4): e18586, 2011.

[156] M. Zaccolo, F. De Giorgi, C. Y. Cho, L. Feng, T. Knapp, P. A. Negulescu, S. S. Taylor, R. Y. Tsien, and T. Pozzan. A genetically encoded, fluorescent indicator for cyclic AMP in living cells. *Nat. Cell Biol.*, 2(1): 25–29, 2000.

[157] T. B. McAnaney, W. Zeng, C. F. E. Doe, N. Bhanji, S. Wakelin, D. S. Pearson, P. Abbyad, X. Shi, S. G. Boxer, and C. R. Bagshaw. Protonation, photobleaching, and photoactivation of yellow fluorescent protein

(`YFP 10C`): a unifying mechanism. *Biochemistry*, 44(14): 5510–5524, 2005.

[158] M. Weiss. Challenges and artifacts in quantitative photobleaching experiments. *Traffic*, 5(9): 662–671, 2004.

[159] G. A. Dunn, I. M. Dobbie, J. Monypenny, M. R. Holt, and D. Zicha. Fluorescence localization after photobleaching (`FLAP`): a new method for studying protein dynamics in living cells. *J. Microsc.*, 205(1): 109–112, 2002.

[160] D. Oron, E. Tal, and Y. Silberberg. Scanningless depth-resolved microscopy. *Optics Express*, 13(5): 1468–1476, 2005.

[161] J. Bewersdorf, R. Pick, and S.W. Hell. Multifocal multiphoton microscopy. *Opt. Lett.*, 23(9): 655–657, 1998.

[162] N. I. Smith, S. Iwanaga, T. Beppu, K. Fujita, O. Nakamura, and S. Kawata. Photostimulation of two types of Ca^{2+} waves in rat pheochromocytoma `PC12` cells by ultrashort pulsed near-infrared laser irradiation. *Laser Phys. Lett.*, 3(3): 154, 2006.

[163] H. Hertz. Ueber die ausbreitungsgeschwindigkeit der electrodynamischen wirkungen. *Ann. Phys.*, 270: 551–569, 1888.

[164] P. Drude and W. Nernst. Ueber die fluorescenzwirkungen stehender lichtwellen. *Ann. Phys.*, 281: 460–474, 1892.

[165] S. Hell and E. H. K. Stelzer. Fundamental improvement of resolution with a 4pi-confocal fluorescence microscope using two-photon excitation. *Opt. Commun.*, 93: 277–282, 1992.

[166] S. Hell and E. H. K. Stelzer. Properties of a 4pi confocal fluorescence microscope. *J. Opt. Soc. Am. A*, 9: 2159–2166, 1992.

[167] S. Cox. personal communication, 22 May 2015.

[168] K. Elsayad, A. Urich, P. S. Tan, M. Nemethova, J. V. Small, K. Unterrainer, and K. G. Heinze. Spectrally coded optical nanosectioning (specon) with biocompatible metal–dielectric-coated substrates. *Proc. Natl. Acad. Sci. U.S.A.*, 110: 20069–20074, 2013.

[169] A. Egner and S. W. Hell. Fluorescence microscopy with super-resolved sections. *Trends Cell Biol.*, 15: 207–215, 2005.

[170] R. Freimann, S. Pentz, and H. Horler. Development of a standing-wave fluorescence microscope with high nodal plane flatness. *J. Microsc.*, 187: 193–200, 1997.

[171] Immersion media for objectives. Available at www.leica-microsystems.com. Accessed April 25, 2014.

[172] Density of glycerine-water solutions. Available at www.dow.com. Accessed February 25, 2014.

[173] Optical materials. Available at www.comaroptics.com. Accessed April 25, 2014.

[174] Leica `TCS SP5 II` technical documentation (2009). Available at www.leica-microsystems.com. Accessed September 16, 2014.

[175] G. L. Rogers. A geometrical approach to moiré pattern calculations. *Optica Acta*, 24: 1–13, 1977.

[176] H. H. Barrett and K. J. Myers. *Foundations of Image Science.* John Wiley & Sons, Inc., Hoboken, New Jersey, 2004.

[177] M. S. Brennesholtz and E. H. Stupp. *Projection Displays.* John Wiley & Sons Ltd., West Sussex, 2nd edition, 2008.

[178] P. Selenyi. Wide-angle interferences and the nature of the elementary light sources. *Phys. Rev.*, 56: 477–479, 1939.

[179] K. H. Drexhage, H. Kuhn, and F. P. Schaefer. Variation of the fluorescence decay time of a molecule in front of a mirror. *Ber. Bunsenges. Phys. Chem.*, 72: 329, 1968.

[180] K. H. Drexhage. Influence of a dielectric interface on fluorescence decay time. *J. Lumin.*, 1–2: 693–701, 1970.

[181] K. H. Drexhage. Monomolecular layers and light. *Sci. Am.*, 222: 108–119, 1970.

[182] K. H. Drexhage. Interaction of light with monomolecular dye layers. In E. Wolf, editor, *Progress in Optics XII*, pages 165–231. North-Holland, Amsterdam, 1974.

[183] W. Lukosz and R. E. Kunz. Light emission by magnetic and electric dipoles close to a plane interface. i. total radiated power. *J. Opt. Soc. Am.*, 67: 1607–1615, 1977.

[184] W. Lukosz and R. E. Kunz. Light emission by magnetic and electric dipoles close to a plane dielectric interface. ii. radiation patterns of perpendicular oriented dipoles. *J. Opt. Soc. Am.*, 67: 1615–1619, 1977.

[185] W. Lukosz. Light emission by magnetic and electric dipoles close to a plane dielectric interface. iii. radiation patterns of dipoles with arbitrary orientation. *J. Opt. Soc. Am.*, 69: 1495–1503, 1979.

[186] E. H. Hellen and D. Axelrod. Fluorescence emission at dielectric and metal-film interfaces. *J. Opt. Soc. Am. B*, 4: 337–350, 1987.

[187] A. Lambacher and P. Fromherz. Fluorescence interference-contrast microscopy on oxidized silicon using a monomolecular dye layer. *Appl. Phys. A*, 63: 207–216, 1996.

[188] J. P. Greer, J. Foerster, G. M. Rodgers, F. Paraskevas, B. Glader, D. A. Arber, and R. T. Means, Jr. *Wintrobe's Clinical Hematology*, volume 1. Lippincott Williams and Wilkins, Philadelphia, 12th edition, 2009.

[189] J. Schlessinger, D. Axelrod, D. E. Koppel, W. W. Webb, and E. L. Elson. Lateral transport of a lipid probe and labeled proteins on a cell membrane. *Science*, 195: 307–309, 1977.

[190] D. C. Chang. Cell poration and cell fusion using an oscillating electric field. *Biophys. J.*, 56: 641–652, 1989.

203

[191] H. Chen, S. Kim, L. Li, S. Wang, K. Park, and J.-X. Cheng. Release of hydrophobic molecules from polymer micelles into cell membranes revealed by Förster resonance energy transfer imaging. *Proc. Natl. Acad. Sci. U.S.A.*, 105: 6596–6601, 2008.

[192] E. A. Hod, N. Zhang, S. A. Sokol, B. S. Wojczyk, R. O. Francis, D. Ansaldi, K. P. Francis, P. Della-Latta, S. Whittier, S. Sheth, J. E. Hendrickson, J. C. Zimring, G. M. Brittenham, and S. L. Spitalnik. Transfusion of red blood cells after prolonged storage produces harmful effects that are mediated by iron and inflammation. *Blood*, 115: 4284–4292, 2010.

[193] M. Diez-Silva, M. Dao, J. Han, C.-T. Lim, and S. Suresh. Shape and biomechanical characteristics of human red blood cells in health and disease. *MRS Bull.*, 35(5):382–388, 2010.

[194] A. Leaf. Cell swelling a factor in ischemic tissue injury. *Circulation*, 48(3):455–458, 1973.

[195] K. A. Reimer and R. B. Jennings. The "wavefront phenomenon" of myocardial ischemic cell death. II. Transmural progression of necrosis within the framework of ischemic bed size (myocardium at risk) and collateral flow. *Lab. Invest.*, 40(6):633–644, 1979.

[196] F. M. Harris, S. K. Smith, and J. D. Bell. Physical properties of erythrocyte ghosts that determine susceptibility to secretory phospholipase A_2^*. *J. Biol. Chem.*, 276: 22722–22731, 2001.

[197] R. Barer and S. Tkaczyk. Refractive index of concentrated protein solutions. *Nature*, 173: 821–822, 1954.

[198] W. T. Tse and S. E. Lux. Red blood cell membrane disorders. *Br. J. Haematol.*, 104: 2–13, 1999.

[199] H. W. G. Lim, M. Wortis, and R. Mukhopadhyay. Stomatocyte–discocyte–echinocyte sequence of the human red blood cell: Evidence for the bilayer–couple hypothesis from membrane mechanics. *Proc. Natl. Acad. Sci. U.S.A.*, 99: 16766–16769, 2002.

[200] P. G. Gallagher. Red cell membrane disorders. *Hematology Am. Soc. Hematol. Educ. Program*, 1: 13–18, 2005.

[201] J. A. Dvorak, L. H. Miller, W. C. Whitehouse, and T. Shiroishi. Invasion of erythrocytes by malaria merozoites. *Science*, 187: 748–750, 1975.

[202] J. C. Pinder, R. E. Fowler, A. R. Dluzewski, L. H. Bannister, F. M. Lavin, G. H. Mitchell, R. J. M. Wilson, and W. B. Gratzer. Actomyosin motor in the merozoite of the malaria parasite, *Plasmodium falciparum*: implications for red cell invasion. *J. Cell Sci.*, 111: 1831–1839, 1998.

[203] B. L. Salmon, A. Oksman, and D. E. Goldberg. Malaria parasite exit from the host erythrocyte: A two-step process requiring extraerythrocytic proteolysis. *Proc. Natl. Acad. Sci. U.S.A.*, 98: 271–276, 2001.

[204] J. Stubbs, K. M. Simpson, T. Triglia, D. Plouffe, C. J. Tonkin, M. T. Duraisingh, A. G. Maier, E. A. Winzeler, and A. F. Cowman. Molec-

ular mechanism for switching of *P. falciparum* invasion pathways into human erythrocytes. *Science*, 309: 1384–1387, 2005.

[205] P. R. Gilson and B. S. Crabb. Morphology and kinetics of the three distinct phases of red blood cell invasion by *Plasmodium falciparum* merozoites. *Int. J. Parasitol.*, 39: 91–96, 2009.

[206] D. T. Riglar, D. Richard, D. W. Wilson, M. J. Boyle, C. Dekiwadia, L. Turnbull, F. Angrisano, D. S. Marapana, K. L. Rogers, C. B. Whitchurch, J. G. Beeson, A. F. Cowman, S. A. Ralph, and J. Baum. Super-resolution dissection of coordinated events during malaria parasite invasion of the human erythrocyte. *Cell Host Microbe*, 9: 9–20, 2011.

[207] W. B. Amos, G. McConnell, and T. Wilson. Confocal microscopy. In E. Egelman, editor, *Comprehensive Biophysics*. Elsevier, Amsterdam, 2012.